Chlorine partitioning in the lowermost Arctic stratosphere during winter – an aircraft in situ measurement perspective

Dissertation zur Erlangung des Grades
„Doktor der Naturwissenschaften"

am Fachbereich Physik, Mathematik und Informatik
der Johannes Gutenberg-Universität
in Mainz

Andreas Marsing
geb. in Nürnberg
Mainz, den 8. Februar 2021

Die mündliche Prüfung wurde am 1. Juli 2021 abgelegt.

Zusammenfassung

Die vorliegende Arbeit untersucht experimentell die Veränderungen der Verteilungen von anorganischen Chlor-Reservoirgasen und aktiven Chlorverbindungen in der polaren untersten Stratosphäre im kalten Winter 2015/2016. Obwohl die Emission langlebiger chlorhaltiger Stoffe durch weltweite Klimaabkommen erfolgreich unterbunden wurde, bleiben stratosphärische Chlorkonzentrationen noch auf Jahrzehnte hinaus erhöht. Chlorverbindungen haben einen bedeutenden Anteil am katalytischen polaren Ozonabbau im Winter und Frühling. Die globale Ozonschicht ist ein wichtiger Faktor für den Strahlungshaushalt der Atmosphäre. Änderungen können Einflüsse haben auf die thermische Struktur und Stabilität der stratosphärischen Schichtung und Zirkulation, auf das Strahlungsbudget der Erdoberfläche und damit auf die Oberflächentemperatur, und nicht zuletzt auf die Belastung von Organismen durch Ultraviolettstrahlung. Der Transport und der katalytische Abbau von stratosphärischem Ozon werden seit vielen Jahren untersucht. Gerade in der polaren untersten Stratosphäre, die durch Mischungsprozesse an der Tropopause beeinflusst ist, verbleiben jedoch große Unsicherheiten in Vorhersagemodellen bezüglich Ozon und seiner Wirkung.

Die vorliegende Arbeit stellt für diese schwer zugängliche Region neue flugzeuggetragene In-situ-Messungen aus der POLSTRACC-Kampagne im Arktischen Winter 2015/2016 vor. Mit dem Forschungsflugzeug HALO wurde dabei der untere Rand des arktischen Polarwirbels von Dezember bis März beprobt. Im Rahmen dieser Arbeit wurde eine Kalibration des Massenspektrometers AIMS bezüglich HCl und $ClONO_2$ entwickelt, welche die schnelle und gleichzeitige Messung dieser Reservoirgase ermöglicht. Für den Verlauf des Winters und Frühlings 2015/2016 konnte aus den flugzeuggetragenen Messungen die Verteilung von anorganischem Chlor in aktive und Reservoir-Spezies mit Hilfe der potenziellen Temperatur quasi-vertikal aufgelöst werden. Es stellt sich heraus, das Chloraktivierung unterhalb von 400 K potenzieller Temperatur nie vollständig erfolgt, anders als bei höheren potenziellen Temperaturen. Gegen Ende des Polarwinters folgt eine unterschiedliche Umverteilung von Chlor in die Reservoirgase: Die Rückgewinnung von HCl dominiert auf niedrigen Höhen, während darüber $ClONO_2$ überwiegt, verursacht durch Konzentrationsgradienten der Reaktionspartner Stickoxide, Ozon und Methan in der untersten Stratosphäre. Dies wird erstmals in massenspektrometrischen In-situ-Messungen mit hoher räumlicher und zeitlicher Auflösung beobachtet. Ein Vergleich mit dem Chemie-Transport-Modell CLaMS zeigt eine mit Ausnahmen gute Übereinstimmung. Zudem geben die lokalen und zufälligen Flugzeugmessungen die allgemeine Entwicklung der Chlorverteilung im Polarwirbel gut wieder. Die hochaufgelösten und genauen Messungen können jedoch eine systematische Überschätzung von HCl im unteren polaren Wirbel im Modell nachweisen. Der beobachtete Fall von außergewöhnlich starker Chloraktivierung in der untersten Stratosphäre zeigt auf, wie wichtig es ist, chemische, mikrophysikalische und dynamische Prozesse von Chlorverbindungen in der oberen Troposphäre und unteren Stratosphäre physikalisch korrekt zu beschreiben, um die Klimaentwicklung dieser Regionen vorhersagen zu können.

Abstract

This thesis experimentally studies the partitioning of inorganic chlorine into active and reservoir species in the polar lowermost stratosphere in the cold Arctic winter 2015/2016. Despite the successful phase-out of further emissions of long-lived chlorine containing substances through worldwide climate agreements, elevated levels of chlorine will persist for decades in the stratosphere. Chlorine compounds are among the major substances for the catalytic depletion of ozone during winter and spring seasons. The global ozone layer is an important factor in the radiative energy budget of the atmosphere, and changes to it can impact the thermal structure and stability of the stratosphere, stratospheric circulation patterns, the surface radiative energy budget controlling surface temperature, and last but not least the stress to organisms through ultraviolet radiation. While transport of ozone in the stratosphere and its catalytic depletion have been investigated in the past decades, major uncertainties in the projection of future ozone and its impact remain, especially in the polar lowermost stratosphere.

The present work addresses the challenging observation and accessibility of this remote area with novel airborne in situ measurements. The HALO aircraft performed the POLSTRACC campaign in the Arctic winter 2015/2016, sampling the lower edge of the Arctic polar vortex from December to March. For the AIMS mass spectrometer, this work describes the development of a calibration for HCl and $ClONO_2$ which enables simultaneous, highly accurate and fast measurements of these chlorine reservoir species. Over the course of the winter and spring 2015/2016, the partitioning of inorganic chlorine into active and reservoir species could be resolved quasi-vertically by potential temperature. It is found that chlorine is never fully activated in the Arctic below 400 K potential temperature, unlike observations at higher temperatures. Repartitioning of chlorine into the reservoir species varies towards the end of the polar winter: the recovery of HCl is favoured on the lower levels, whereas $ClONO_2$ is favoured on the higher levels, due to concentration gradients in the available reaction partners nitrogen oxides, ozone and methane in the lowermost stratosphere. For the first time, this is observed with mass spectrometric in situ measurements at high temporal and spatial resolution. A comparison to the chemistry transport model CLaMS shows good agreement, with some exceptions, and demonstrates that the local and random airborne observations well represent the overall evolution of chlorine partitioning in polar vortex airmasses. Yet, the high accuracy and resolution of the measurements enable the detection of a systematic high bias of HCl in the model in the lowermost polar vortex. An observation of exceptionally high active chlorine in the lowermost stratosphere highlights the importance of a physically correct representation of chemical, microphysical and dynamical processes of chlorine species in the upper troposphere and lower stratosphere in climate projections.

Partial results of the presented work have been published in the following peer-reviewed articles. For each article the respective contributions of this monograph's author (AM) are declared.

Marsing, A., T. Jurkat-Witschas, J.-U. Grooß, S. Kaufmann, R. Heller, A. Engel, P. Hoor, J. Krause, and C. Voigt (2019). "Chlorine partitioning in the lowermost Arctic vortex during the cold winter 2015/2016". In: *Atmos. Chem. Phys.* 19.16, pp. 10757–10772. DOI: 10.5194/acp-19-10757-2019.

AM performed and evaluated the AIMS measurements. He devised and performed the study including other contributed instrumental and model data, and wrote the manuscript.

Johansson, S., W. Woiwode, M. Höpfner, F. Friedl-Vallon, A. Kleinert, E. Kretschmer, T. Latzko, J. Orphal, P. Preusse, J. Ungermann, M. L. Santee, T. Jurkat-Witschas, A. Marsing, C. Voigt, A. Giez, M. Krämer, C. Rolf, A. Zahn, A. Engel, B.-M. Sinnhuber, and H. Oelhaf (2018). "Airborne limb-imaging measurements of temperature, HNO_3, O_3, $ClONO_2$, H_2O and CFC-12 during the Arctic winter 2015/2016: characterization, in situ validation and comparison to Aura/MLS". In: *Atmos. Meas. Tech.* 11.8, pp. 4737–4756. DOI: 10.5194/amt-11-4737-2018.

AM performed and evaluated the AIMS measurements (Sec. 2.2), and discussed them in the validation of GLORIA's nitric acid (Sec. 4.3.3 and Fig. 7) and chlorine nitrate (Sec. 4.3.5 and Fig. 9) measurements. Further comparison is given in the supplement material.

Oelhaf, H., B.-M. Sinnhuber, W. Woiwode, H. Bönisch, H. Bozem, A. Engel, A. Fix, F. Friedl-Vallon, J.-U. Grooß, P. Hoor, S. Johansson, T. Jurkat-Witschas, S. Kaufmann, M. Krämer, J. Krause, E. Kretschmer, D. Lörks, A. Marsing, J. Orphal, K. Pfeilsticker, M. Pitts, L. Poole, P. Preusse, M. Rapp, M. Riese, C. Rolf, J. Ungermann, C. Voigt, C. M. Volk, M. Wirth, A. Zahn, and H. Ziereis (2019). "POLSTRACC: Airborne Experiment for Studying the Polar Stratosphere in a Changing Climate with the High Altitude and Long Range Research Aircraft (HALO)". In: *Bull. Amer. Meteor. Soc.* 100.12, pp. 2634–2664. DOI: 10.1175/bams-d-18-0181.1.

AM performed and evaluated the AIMS measurements. He presented and discussed the occurrence of exceptional chlorine activation in the lowermost stratosphere (pp. 2654–2656 and Fig. 15) and its relevance for ozone depletion.

Contents

Contents

1. Introduction

The discovery of the ozone hole – first over Antarctica in 1976, later also in the Arctic – led to an intense search for its origin and culminated in the implementation of the Montreal Protocol, the first supranational agreement that, together with several amendments, has led to an effective decline in the emission of ozone depleting substances (ODS). A huge success also for the reduction of anthropogenic climate change, the current struggle for implementing a new all-embracing climate agreement that is convincing, bearable and fair for all parties emphasises the need for more accurate in-detail understanding of atmospheric processes. This includes further studies on ODS that are still around and that will have significant climate impact in the coming decades.

While global warming of the Earth's surface and the lower atmosphere has reached about 1 °C compared to pre-industrial levels (IPCC, 2018), with a further positive trend, certain environments are affected from the anthropogenic climate change in different fashions and strengths. Over the last decades, the Arctic polar region has experienced warming thrice as high as the global average temperature increase. This in an indication of the so-called Arctic amplification, a result of complex interactions and feedback (overview in Wendisch et al., 2017, and references therein). Surface warming is connected to a shift in the radiative equilibrium of the atmosphere, established by the surface albedo, clouds and radiatively active trace gases, such as water vapour, carbon dioxide, methane or ozone. Anthropogenic emissions of ODS have led to the formation of the ozone hole in the polar winter stratosphere, before actions under the Montreal Protocol suppressed further ODS emission.

Particular importance in the estimation of the effects of climate relevant gases comes to regions where these substances as well as the temperature profiles exhibit large gradients, as they control the effective and spectrally resolved radiative balance of the surrounding air masses and of the atmosphere as a whole. In that respect, the upper troposphere/lowermost stratosphere (UTLS) marks the transition of the humid troposphere to the dry and ozone-rich stratosphere. Therefore, understanding the physical and chemical processes in the Arctic UTLS is crucial for a reliable estimation of the current and future radiation budget and global climate (Riese et al., 2012).

Ozone (O_3) in the polar stratosphere is primarily depleted by a photochemically driven catalytic cycle where gas phase molecular chlorine and chlorine oxides provide the catalyst to

reduce ozone molecules to oxygen (Molina and Molina, 1987). All of the chlorine species that contribute to this reaction are summarised under the term "active chlorine", which is abbreviated as ClO_x and comprises Cl, Cl_2, ClO, $ClOOCl$, $OClO$ and $HOCl$. Conversely, the passive molecules hydrogen chloride (HCl) and chlorine nitrate ($ClONO_2$, recent review by Clarmann and Johansson, 2018) contribute only indirectly to ozone depletion and are therefore called reservoir species. Besides chlorine, bromine compounds are also important contributors to catalytic ozone destruction. Bromine has the second most prominent role in ozone depletion cycles, with a higher reaction efficiency but far lower abundance, compared to chlorine (e.g. Daniel et al., 1999).

Chlorine is introduced into the stratosphere via chloroflourocarbons (CFCs) from anthropogenic sources. While the emission of CFCs has nearly ceased as a consequence of the Montreal Protocol and its amendments, Montzka et al. (2018) reported a slow down of the decrease rate of atmospheric CFC-11 since 2012 at some measurement sites, indicating unexpected new sources. In addition, chlorinated very short-lived substances (VSLS) appear to contribute an increasing fraction to the stratospheric chlorine burden (Hossaini et al., 2019). Therefore, continued monitoring of chlorine species and their predecessors is a crucial necessity for projections of the future climate, as the reservoir species remain in the stratosphere for decades due to their long chemical lifetimes (WMO, 2011) and chlorine-catalysed ozone depletion will continue to occur throughout the 21st century.

Polar stratospheric clouds (PSCs) play a prominent role in ozone depletion, as they provide a surface for the heterogeneous reactions that produce active chlorine from the reservoir species (Crutzen and Arnold, 1986; Drdla and Müller, 2012). PSCs are these solid condensates of nitric acid-trihydrate (Fahey et al., 2001; Voigt et al., 2000a), water ice (Toon et al., 2000) or liquid ternary solution particles (Carslaw et al., 1994; Voigt et al., 2000b) and occur only at very low temperatures below about 196 K. Hence they regularly appear inside the stratospheric polar vortices. During winter radiative cooling over the poles leads to the formation of the polar vortex which acts as a transport barrier between polar and mid-latitude stratospheric air. As sunlight returns in spring, photochemical reactions are initiated that lead to chlorine activation and to the formation of the ozone hole. It is less pronounced in the Arctic than in the Antarctic due to a less stable polar vortex as a consequence of enhanced planetary wave activity on the northern hemisphere (e.g. Matthias et al., 2016; Solomon et al., 2014).

The focus of this thesis is on processes in the lowermost polar stratosphere (LMS). A common definition locates the LMS between the tropopause and the 380 K isentrope (Holton et al., 1995). Although it shares most features with the greater part of the entire stratosphere, the vicinity of the tropopause makes it prone to stratosphere-troposphere exchange (STE). Also, in the polar winter LMS, the transport barrier of the polar vortex becomes weaker towards the tropopause, enabling isentropic transport and mixing (e.g. Werner et al., 2010) with air from

the lower latitude stratosphere and the extratropical transition layer (ExTL; WMO, 2003). These processes alter the composition of the polar LMS. This is relevant to climate in various ways, for example: The radiation budget is changed through the introduction of water vapour (Forster and Shine, 2002) or methane (e.g. Riese et al., 2012); these species, however, also alter the chlorine budget in gas phase or heterogeneous reactions, with implicit effects on ozone. Furthermore, ozone may be diluted – beyond removal by chemical processing – through horizontal mixing and isentropic transport towards lower latitudes (Knudsen et al., 1998; Knudsen and Grooß, 2000).

As stated above, it is necessary to resolve the physical and chemical processes in and around the LMS in detail in order to assess the implication of climate change on this region. Climate model intercomparisons (Bekki et al., 2013) and sensitivity studies (e.g. Xia et al., 2017) found the most severe disagreements in projected ozone change and ozone-climate impact within the polar LMS. In the northern hemisphere, even the sign of change is unclear. This is the consequence of uncertainties on the transport pathways of ozone and counteracting effects from catalytic depletion and stratospheric cooling during climate change, where some transport and chemical processes may have not been implemented into the models in all detail. In particular, Khosrawi et al. (2017) have shown recently that the climate model ECHAM5/MESSy Atmospheric Chemistry (EMAC) underestimates stratospheric downward transport in the polar vortex and potentially inherits uncertainties in chlorine chemistry kinetics. The lack of observations inside the polar LMS may contribute to the enhanced uncertainty. Access is challenging as satellite data products, e.g. from the Microwave Limb Sounder (MLS) or the Atmospheric Chemistry Instrument-Fourier Transform Spectrometer (ACE-FTS), do not achieve the high vertical resolution necessary to resolve strong concentration gradients near the tropopause (e.g. Livesey et al., 2017; Mahieu et al., 2008; Wolff et al., 2008). On the other hand, there have been numerous airborne activities in the Arctic LMS, but only few airborne (Bonne et al., 2000; Wilmouth et al., 2006) or balloon-borne (e.g. Wetzel et al., 2015) measurement platforms that have yet sampled the polar LMS chlorine budget. Several studies focused on ozone depleting ClO and the dimer ClOOCl (Hobe et al., 2005; Sumińska-Ebersoldt et al., 2012; Vogel et al., 2003) and heterogeneous chlorine chemistry (Wegner et al., 2012; Wohltmann et al., 2013; summary in Hobe et al., 2013). These studies have been very valuable for the understanding of chlorine-catalysed ozone depletion especially in the free stratosphere, where the spatial and temporal extent of PSCs enables full chlorine activation. Regarding the overall Cl_y budget, however, especially early measurements within the POLARIS mission in 1997 were low biased in HCl (Bonne et al., 2000). A newer comprehensive in situ sampling of chlorine species – including both reservoir gases – in the Arctic lower stratosphere was conducted in the SOLVE/THESEO mission in winter 1999/2000 using the ER-2 high altitude aircraft (Wilmouth et al., 2006). The HCl bias (relative to $ClONO_2$) was overcome, but the Cl_y budget was still inconclusive. Gener-

ally, measurements from aircraft are able to combine high spatial resolution, a benefit in the manifold environment near the tropopause, with sufficient temporal coverage in a suitable deployment.

The preceding remarks demonstrate a lack in understanding of the occurrence of activated chlorine in the UTLS and of the transition of chlorine partitioning between the upper troposphere and the lower stratosphere. The following hypotheses are set up for this thesis:

1. Unlike the middle and upper stratosphere, tropopause-related gradients in trace gases impact the chlorine partitioning in the lowermost stratosphere throughout the polar winter.

2. The lowermost stratosphere can experience exceptionally high levels of active chlorine.

The thesis addresses these hypotheses by introducing a novel dataset of airborne in situ measurements, primarily of the inorganic chlorine reservoir species HCl and $ClONO_2$. The measurements were performed within the POLar STRAtosphere in a Changing Climate (POL-STRACC) aircraft campaign in the Arctic winter 2015/2016 (Oelhaf et al., 2019). To elaborate on the acquisition and evaluation, but also on the scientific background, the thesis is structured as follows: Chapter 2 gives a brief introduction on atmospheric chlorine chemistry and its implications on ozone. Chapter 3 contains the recent development and characterisation of the experimental setup involved in obtaining the data. The study of chlorine partitioning in the Arctic winter 2015/2016 follows in chapter 4. Chapter 5 summarises the results and gives an outlook to future activities and research needs.

2. Basic knowledge about atmospheric chlorine and its impact

Setting a foundation to the subsequent study, this chapter introduces the relevant background information on physical and chemical processes involved in the chlorine partitioning of the polar stratosphere. The two major topics are chlorine compounds themselves and ozone depletion, which is nowadays the predominant climate impact of chlorine loading of the atmosphere by anthropogenic emissions. Lastly some terms of stratospheric dynamics are defined.

2.1. The role of chlorine in the stratosphere

This section introduces the basic concepts and reactions of chlorine in the stratosphere, emphasizing the importance for the ozone budget, which is the most relevant contribution of global chlorine to Earth's climate. Chlorine belongs to the group of the halogen chemical elements, which comprises also fluorine, bromine and iodine.[1] In many respects the halogens feature similar chemical behaviour and properties. Therefore, most of the statements and concepts about chlorinated substances in this section apply also to other halogenated substances in an often similar, not always equal, fashion.

2.1.1. Introduction of chlorine into the stratosphere

Chlorine in the atmosphere always originates from sources at the surface of the Earth. It is introduced in the form of various gases or by means of sea salt aerosol. One often discriminates between organic (i.e. carbon-containing) and inorganic chlorine compounds or molecules as these two classes are somewhat distinguished by their atmospheric lifetimes. The lifetime of an atmospheric trace gas estimates the average time period from the introduction at a source to the removal at a sink. It should be noted that it is not appropriate to assign a single lifetime for chlorine compounds in the entire atmosphere, as they are subject to different chemical

---

[1] Astatine ($_{85}$At) and – potentially – tennessine ($_{117}$Ts) are (very) short-lived radioactive halogens.

and physical processes depending on their location. For example, the most prominent inorganic chlorine compound, hydrogen chloride (HCl), has a short lifetime of a few days in the troposphere and a longer lifetime on the order of months in the stratosphere.

Earth's surface connects the atmosphere to the biggest chlorine reservoir, the oceans. HCl, as well as other reactive and volatile compounds such as Cl_2, HOCl, $ClNO_2$ or BrCl can be released from sprayed sea salt aerosol by means of acidification in the presence of sulfuric acid (H_2SO_4) or nitric acid (HNO_3) (Graedel and Keene, 1995, 1996). There are also other processes such as photodissociation or cloud processing that may release chlorine (Keene et al., 1999). Similarly, inorganic chlorine is contained in mineral aerosol (Talbot et al., 1986) and in volcanic eruption material, mainly HCl (Symonds et al., 1988). Most of the released compounds are quickly returned to the surface through wet and dry deposition. Natural organic chlorine compounds are released in a large variety, where methyl chloride (CH_3Cl) is the most prominent, followed by chloroform ($CHCl_3$). They originate from the ocean, from terrestrial ecosystems and from biomass burning (Grimvall and Leer, 1995). Only the organic compounds have a sufficiently long tropospheric lifetime to reach the stratosphere at significant amounts. Of the natural compounds, CH_3Cl has the largest contribution with an estimated flux of $30\,Gg\,Cl\,year^{-1}$ (Graedel and Crutzen, 1992).

Human activities have raised the chlorine loading of the atmosphere in several ways. First, emitted precursors such as H_2SO_4 or HNO_3 lead to a high anthropogenic contribution to the above mentioned release of HCl from sea salt aerosol (Keene et al., 1999). Second, industrial emissions, combustion, incineration and additional biomass burning increase the fluxes of the tropospheric chlorine sources introduced above (ibid.). Quantifying the corresponding anthropogenic chlorine emissions, which are as of yet unregulated, is a task of repeatedly updated emission inventories. From a stratospheric point of view, emissions of most inorganic chlorine species are of lesser interest due to the rapid scavenging. The emitted organic chlorine, i.e. the chlorocarbons (CCs), are commonly attributed "reactive" and denoted as very short-lived substances (VSLS, with a lifetime of less than 0.5 years), as only a fraction of them reaches the stratosphere. Explicitly not included in the VSLS are CH_3Cl and CCl_4, which have longer lifetimes (WMO, 2018).

Third, these terms imply a relative scale of (stratospheric or upper tropospheric) lifetimes, and this scale is filled at the opposite end by long-lived chlorine species. This class of compounds knows no natural sources. It consists of the chlorofluorocarbons (CFCs), hydrochlorofluorocarbons (HCFCs) and halons. These synthetic compounds are highly stable[2] and thus accumulate over time in the stratosphere, where their lifetimes range in the tens to hundreds of years.

---

[2]HCFCs and some halons in the troposphere can be destroyed by reactions with OH radicals. This limits their tropospheric lifetimes, which still amounts, however, to well above one year in most cases.

Table 2.1.: Non-exhaustive list of the most abundant chlorinated substances in the tropo-
sphere. Abundances are compiled from a more complete list from WMO (2018,
with references therein) as annual mean global mean mole fractions in 2016.
Small letters "a" and "n" denote anthropogenic and natural origin, respectively.

group	molecule	common name	abundance (ppt)	origin
CFCs	CCl_2F_2	CFC-12	515.9	a
	CCl_3F	CFC-11	230.2	a
	CCl_2FCClF_2	CFC-113	71.7	a
HCFCs	$CHClF_2$	HCFC-22	235.3	a
	CH_3CCl_2F	HCFC-141b	24.4	a
halons	$CBrClF_2$	halon-1211	3.59	a
CCs	CH_3Cl	methyl chloride	555	n, a
	CCl_4	carbon tetrachloride	80.5	a
VSLSs	CH_2Cl_2	dichloromethane	34	a (mainly)
	$CHCl_3$	chloroform	8.9	n, a

Table 2.1 lists the most abundant representatives of the different groups of chlorine com-
pounds in the troposphere as obtained from ground-based measurements. The complete list
of known compounds without VSLSs comprises about 290 species. It can be seen that to
date, human activities contribute the major part of the total tropospheric chlorine loading. In
2016, CFCs alone contained 60 % of tropospheric chlorine, followed by CH_3Cl with 17 %,
CCl_4 with 10 % and HCFCs with 9.5 %. VSLSs amounted to approximately 3 %.

At the tropopause, predominantly in the tropical tropopause layer (TTL), this mixture of
chlorine compounds is injected into the stratosphere. Regarding VSLSs, these gases exhibit
a higher variability in concentrations throughout the troposphere due to their volatility, de-
pending on source locations, reactant concentrations and transport pathways. Consequently
their injection into the stratosphere is also subject to enhanced variations. In this regard one
distinguishes between source gas injection (SGI, i.e. direct injection of the VSLSs) and prod-
uct gas injection (PGI), where chlorine was previously processed from the source gas into
another molecule in the troposphere. For example, product gases may be phosgene ($COCl_2$)
or HCl (Harrison et al., 2019; Hossaini et al., 2015). This processing is still a matter of on-
going research in order to quantify conversion rates and to incorporate all relevant species in
the calculated fluxes of chlorine into the stratosphere.

2.1.2. Repartitioning of chlorine compounds in the stratosphere

CFCs (and HCFCs and halons) as well as VSLS themselves are not reactive with ozone
in the stratosphere. The main reaction for these species is a photolytic dissociation releasing
atomic chlorine under the impact of solar far ultraviolet (UV) radiation (Molina and Rowland,

1974), taking place at altitudes higher than about 20 km above the bulk of the ozone layer. Also atomic oxygen (O) or the hydroxyl radical (OH) can release chlorine from the injected gases forming ClO (Mébarki et al., 2010). The highly reactive (also called active) Cl atoms and ClO are then part of a catalytic cycle destroying ozone (Sec. 2.2.2). This cycle is only interrupted by a removal of ClO, which is called chlorine deactivation. This can occur by a reaction with nitrogen oxide through

$$\text{ClO} + \text{NO}_2 + \text{M} \longrightarrow \text{ClONO}_2 + \text{M} \tag{R 2.1}$$

with a collision partner M. The availability of NO_2 in the stratosphere depends upon the release from gaseous HNO_3 through photolysis or through a reaction with OH. Chlorine nitrate ($ClONO_2$), however, can be decomposed again via photolysis:

$$\text{ClONO}_2 \xrightarrow{h\nu} \text{ClO} + \text{NO}_2, \tag{R 2.2}$$

where $h\nu$ denotes a photon with frequency ν and h is the Planck constant. Another loss mechanism for active chlorine is a reaction with methane:

$$\text{Cl} + \text{CH}_4 \longrightarrow \text{HCl} + \text{CH}_3. \tag{R 2.3}$$
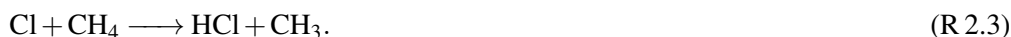
As will be evident from Sec. 2.2.2, the availability of Cl is reduced by (still present) ozone. Therefore, reaction R 2.3 requires low levels of ozone. Furthermore, several other reaction pathways have been proposed that ultimately lead to the formation of HCl, the next relevant of which is a reaction of ClO with OH:

$$\text{ClO} + \text{OH} \longrightarrow \text{HCl} + \text{O}_2. \tag{R 2.4}$$

OH, however, also enables the reverse reaction

$$\text{HCl} + \text{OH} \longrightarrow \text{Cl} + \text{H}_2\text{O}. \tag{R 2.5}$$

Other reactions involving OH, HO_2, Cl_2 and other species have been omitted in this conceptual summary. A more comprehensive description can be found in Wilmouth et al. (2006) and in the references therein. Accounting for the relative rate constants of the above reactions, gas phase and photochemical reactions in the stratosphere slowly redistribute chlorine into the two most stable compounds HCl and $ClONO_2$. Those are called the chlorine reservoir gases. The equilibrium partitioning among the two favours HCl, but the exact relation in each environment depends on the abundance of other gases involved in the above reactions.

The characteristic property of stratospheric chlorine is that it can be activated (i.e. repartitioned into molecules other than the reservoir gases) in a new temporary equilibrium through

the depletion of reservoir species in heterogeneous reactions on the surfaces of stratospheric cloud particles. This will be elaborated on in Sec. 2.2.3. It is this activation mechanism that drives the large scale polar ozone depletion.

HCl is highly soluble in water. This provides the main sink of stratospheric chlorine through uptake in high cirrus clouds in the transition region of the upper troposphere and lower stratosphere (Sec. 2.3 below), and the subsequent particle descent. The limitation of this removal mechanism to the lower boundary of the stratosphere causes the long stratospheric lifetime of inorganic chlorine. The uptake of HCl in stratospheric clouds, such as PSCs (Sec. 2.2.3), is probable due to the high fraction of contained water, but the quantity is currently debated. Whereas this alters the amount and composition of gaseous inorganic chlorine significantly, downward transport of PSCs is mostly limited to within the stratosphere and not attributed a major sink of overall stratospheric chlorine.

2.1.3. Impact of stratospheric chlorine: Radiation and composition

Chlorine compounds in the stratosphere alter the radiation budget and the composition in several ways. Due to their current abundance and the strength of the effects, these compounds are denoted as climate relevant trace species.

CFCs act as greenhouse gases similar to carbon dioxide (CO_2). Their radiative efficiency however, expressed as the change in radiative forcing per given change in concentration, is more than five orders of magnitude higher than that of CO_2 This is a property shared among most "minor" greenhouse gases (other than CO_2, CH_4 and N_2O) due a strongly linear dependency which has not yet reached a certain saturation threshold. Phasing out CFCs and other hydrocarbons through the Montreal Protocol thus actively helps in reducing the anthropogenic impact on global warming.

The following Sec. 2.2 will elaborate on ozone depletion, the most prominent climate effect of stratospheric chlorine. But this is not the only climate relevant chemical effect. Reaction R 2.3 shows that the recovery of HCl involves the depletion of methane (CH_4), the next important greenhouse gas behind CO_2. This reaction is not catalytic, but overall it can be noted that the formation and presence of active chlorine increases the oxidation capability of the atmosphere, with subsequent effects on a broad range of species, which are or may become relevant to climate, especially in sensitive regions like the UTLS.

2.2. Ozone depletion in the stratosphere

Stratospheric ozone is important for life on Earth's surface, as it shields solar ultraviolet (UV) radiation, predominantly in the wavelength range of 280 to 320 nm (Dameris et al., 2011). As such it forms the lower wavelength limit of the atmospheric window for sunlight reaching the surface. Its strong radiative impact causes the positive temperature gradient and stable thermal stratification in the stratosphere. Therefore the ozone abundance has been and will be a subject of careful monitoring and model projections for the assessment of current and future biomedical and climate impact.

The impact of stratospheric chlorine on ozone, and hence the coupled climate impact, will be explained in the following sections. For completeness this also includes a short treatment of the stratospheric circulation and the formation of polar stratospheric clouds (PSCs) that are requirements for the large scale chlorine-catalysed ozone depletion.

2.2.1. Chapman cycle: The natural photochemical equilibrium

Ozone is a gas that consists of three oxygen atoms (O_3). As such, it can be purely created from atmospheric molecular oxygen (O_2), which constitutes about 20.95 % in volume of the lower and middle atmosphere (Huang et al., 2018). Ozone is produced by photolysis of one oxygen molecule given a UV photon. The oxygen atoms can then quickly react with other oxygen molecules to form ozone:

$$O_2 \xrightarrow{h\nu} 2O \quad (\lambda < 242\,\text{nm}) \tag{R 2.6}$$

$$O + O_2 \xrightarrow{M} O_3 \quad (2\,\text{x}). \tag{R 2.7}$$

Here, $\lambda = \frac{c}{\nu}$ is the wavelength of the photon and M is a collision partner. But there is also the rapid reverse photolysis

$$O_3 \xrightarrow{h\nu} O + O_2. \tag{R 2.8}$$

It is this reaction that already points out the importance of the ozone layer for surface radiation, as the ozone photolysis occurs also at wavelengths longer than 242 nm, with the highest photon absorption cross sections below about 310 nm (Burrows et al., 1999). It is only in the presence of ozone that solar UV-B (and remaining UV-C) radiation, harmful to the cells of living organisms, is prevented from reaching the lower atmosphere. Reactions R 2.7 and R 2.8 constitute the Chapman ozone-oxygen cycle.

Through these reactions, ozone and atomic oxygen stand in a rapid photochemical equilibrium. Therefore, ozone can only be depleted upon removal of atomic oxygen, and this
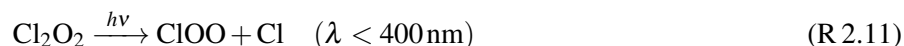
eventually happens through the loss reaction

$$O + O_3 \longrightarrow 2\,O_2, \tag{R 2.9}$$

which removes both an oxygen atom and an ozone molecule. This loss mechanism is dependent on altitude: In the upper stratosphere, high UV radiation leads to higher atomic oxygen, limiting the upper extent of the ozone layer. The maximum ozone mixing ratio is found at 30 km to 40 km altitude in the tropics, from where poleward transport redistributes ozone over the globe (e.g. Grooß and Russell, 2005).

2.2.2. Catalytic ozone depletion

More pronounced ozone depletion is enabled in the presence of catalysts that enable processing without the need of the atomic oxygen. Besides the naturally occurring hydroxyl radical OH, catalysts from anthropogenic sources comprise nitrogen oxides (Crutzen, 1970) and halogenated radicals. This last group was first proposed by Molina and Rowland (1974) as the main driver of the major ozone depletion leading to the so called ozone hole in the polar winter stratosphere. The reaction scheme for chlorine compounds as the prevalent halogen catalyst is as follows: Assuming the existence of the chlorine oxide ClO, the catalytic reaction is:

$$ClO + ClO + M \longrightarrow Cl_2O_2 + M \tag{R 2.10}$$

$$Cl_2O_2 \xrightarrow{h\nu} ClOO + Cl \quad (\lambda < 400\,nm) \tag{R 2.11}$$

$$ClOO \longrightarrow Cl + O_2 \tag{R 2.12}$$

$$Cl + O_3 \longrightarrow ClO + O_2 \quad (2x). \tag{R 2.13}$$

Here, M is again a collision partner. This process involving the chlorine oxide dimer Cl_2O_2 (Molina and Molina, 1987)[3] is very effective in providing the necessary atomic chlorine Cl and makes use of a broader range of the solar spectrum than the oxygen dissociation mechanism, reaching beyond the main ozone absorption band. Another important ozone loss mechanism includes the bromine oxide BrO in the combined reaction (omitting intermediate steps)

$$ClO + BrO \longrightarrow Cl + Br + O_2 \tag{R 2.14}$$

that again produces two reactive halogen atoms, each being able to destroy one ozone molecule like in reaction R 2.13.

---

[3]The Cl_2O_2 dimer exists in the predominant form ClOOCl and in the form ClOClO. The abbreviated chemical notation comprises both.

As seen before, a prerequisite for active chlorine and hence catalytic ozone depletion is the presence of heterogeneous reaction partners. Polar stratospheric clouds provide such reaction sites for the large scale ozone loss in the polar winter stratosphere. The following section briefly presents their characteristics.
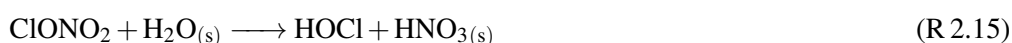
2.2.3. Polar stratospheric clouds and chlorine activation

As the concentration of water vapour generally decreases with altitude in the troposphere and lower stratosphere, the relative humidity in the lower stratosphere rarely reaches saturation, required for persistent water clouds (cirrus). This is fostered by the positive stratospheric temperature gradient.

In the polar regions, the lack of sunlight in winter leads to a diabatic cooling and downward motion of air. That is, net heat is radiated into space and the potential temperature decreases. This fuels the downward polar component of the Brewer-Dobson circulation, the major stratospheric overturning circulation between the tropics and the polar regions. Strong geostrophic westerly winds emerge that form a stratospheric circumpolar vortex. The isolated airmasses inside undergo enhanced diabatic cooling, reaching temperatures below $-80\,°C$.

Polar stratospheric clouds (PSCs) observed in these airmasses have been characterised to consist of solid condensates of water (ice), nitric acid trihydrate (NAT) or liquid supercooled ternary solutions (STS) (Voigt et al., 2018, and references therein). Figure 2.1 shows an example of a lidar measurement from the HALO aircraft during the POLSTRACC campaign, where a synoptic-scale PSC was observed and the composition classified. The frost point of NAT, dependent on the partial pressures of water vapour and nitric acid (HNO_3), is higher that that of pure water ice and a few degrees below $200\,K$ at typical stratospheric conditions (Hanson and Mauersberger, 1988), making NAT-PSCs the most widespread PSC type. Their climatological average extent at $30\,hPa$ is as high as $0.5\,(2.2)\cdot10^7\,km^2$ on the northern (southern) hemisphere (Voigt et al., 2018).

The PSC surface contains water ($H_2O_{(s)}$) and may incorporate hydrogen chloride ($HCl_{(s)}$), enabling the heterogeneous reactions (Dameris et al., 2011; Wilmouth et al., 2006)

$$ClONO_2 + H_2O_{(s)} \longrightarrow HOCl + HNO_{3(s)} \tag{R 2.15}$$

$$ClONO_2 + HCl_{(s)} \longrightarrow Cl_2 + HNO_{3(s)}. \tag{R 2.16}$$

Here, the subscript (s) denotes reaction partners in the solid phase as opposed to the gas phase. These activation reactions repartition chlorine from the gaseous reservoir species into
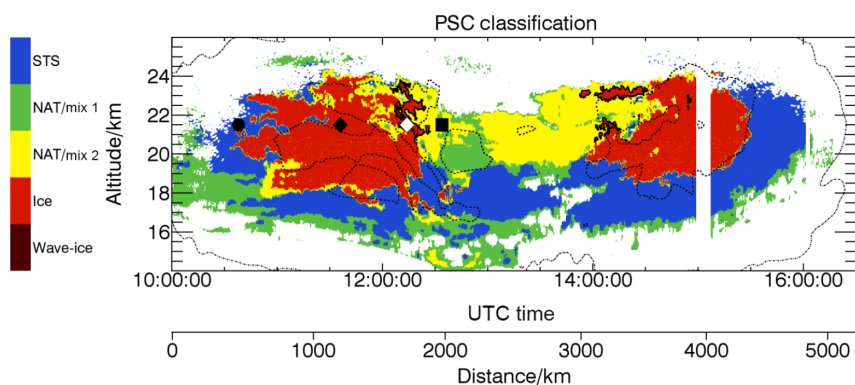
Figure 2.1.: Cross section of a synoptic-scale PSC from an airborne measurement with the WALES lidar on HALO on 22 January 2016. The vertical beam sampled the cloud above the flight track of the aircraft. Colours indicate a classification of the PSC type from properties of the backscatter signal. It can be seen that large patches at different locations and altitudes are dominated by a certain PSC type. Figure taken from Voigt et al. (2018).

reactive Cl_2 and $HOCl$ molecules, that are rapidly photolytically converted into the ozone-destroying radicals at the return of sunlight (and that are therefore included in the "active chlorine" (ClO_x), as will be seen later).

Further, as NAT PSCs form, they extract HNO_3 from the gas phase and sediment down, transporting HNO_3 to lower altitudes, depleting the overall nitrogen oxide budget above (denitrification) and inhibiting the fastest deactivation pathway, the formation of $ClONO_2$ (Reaction R 2.2). As the PSC particles sediment, they release HNO_3 upon sublimation in the warmer conditions of different airmasses (renitrification).[4]

Chlorine activation through Reactions R 2.15 and R 2.16 is not limited to PSCs. It happens wherever clouds, like cirrus, occur in stratospheric air masses. The extent and impact of possible chlorine activation on cirrus and potentially aerosol, which may be more common in the mid latitudes or tropics, is still discussed (e.g. Borrmann et al., 1996; Hobe et al., 2011; Solomon et al., 1997; Thornton et al., 2007). Model simulations and rare in situ observations suggest the potential for significant chlorine activation on cirrus, up to at least 50 % of total Cl_y.

---

[4]The same is true of course for the other constituents, and especially stratospheric dehydration is a likewise relevant research topic.

2.3. The upper troposphere and lowermost stratosphere

This section briefly elaborates on the region of interest in this thesis and on some terms that appear repeatedly throughout the work. Figure 2.2 from Gettelman et al. (2011) with a meridional picture of lower atmospheric dynamics is well suited to illustrate the phenomena.
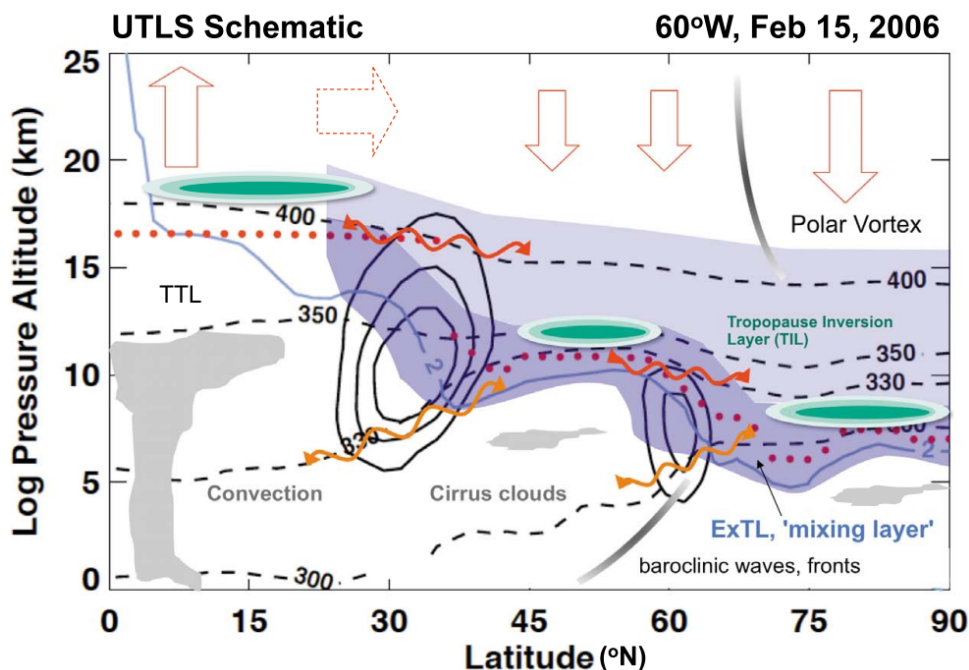

Figure 2.2.: Meridional schematic of the extratropical UTLS (shaded area), the ExTL (dark part of the shaded area), the thermal (red dotted line) and dynamic (blue line) tropopause, the BDC (bold arrows), extratropical STE (wavy arrows), the subtropical jet (zonal wind speed in black contours, here split in two jets) and some isentropes (black dashed lines). The abbreviations are explained in the text. Some additional visible features are explained only in the original work. Figure taken from Gettelman et al. (2011).

The upper troposphere/lower stratosphere (UTLS) is the transition region above and below the tropopause that inherits properties of both the troposphere and the stratosphere. It extends roughly $\pm 5\,\text{km}$ above and below the tropopause and contains processes known as stratosphere-troposphere exchange (STE) (Holton et al., 1995). At the transition between the negative and positive temperature gradients, it is the coldest region of the lower atmosphere. Strong gradients in humidity and many other radiatively relevant species across the UTLS assign it a key role for climate through the control of radiative forcing. The more confined region around the extratropical tropopause where mixing due to STE is ubiquitous (e.g. Hoor et al., 2002, 2004, 2010) is called the extratropical transition layer (ExTL).[5]

---

[5]There is also a tropical transition layer (TTL), but with very different processes that are not covered here.

The Brewer-Dobson circulation (BDC) is the stratospheric overturning circulation. It transports "fresh" tropospheric air in the "tropical pipe" up into the stratosphere. After subsequent poleward motion at different altitudes and time scales on the order of years, downwelling occurs at the high latitudes. As mentioned before, the strongest downwelling including diabatic descent occurs each year inside the isolated polar vortex. Meanwhile the vortex represents a strong barrier against otherwise common isentropic exchange between polar and mid latitude air.

The lowermost stratosphere (LMS) is the stratospheric part of the UTLS. The term most commonly refers to the extratropical region roughly between the 340 K and the 440 K isentrope. It is constantly fed by the downward components of the BDC. The polar vortex weakens in the LMS, enabling more meridional exchange. Influence from the troposphere arises mainly through quasi- or cross-isentropic exchange from the ExTL in the vicinity of strong wind shear at the subtropical jet.

The following chapter will introduce the instrumentation that has been developed and used specifically to sample inorganic chlorine species in the extratropical UTLS.

3. Instrumentation

This chapter introduces the experimental instrumentation used by the analysis in this work. A special emphasis is set on the instruments that the author operated himself, where characteristics, procedures, calibration, data processing and verification are explained. Furthermore, the origin and processing of model data are covered.

3.1. The AIMS instrument

This section describes the setup and operation of the AIMS mass spectrometer. Section 3.1.1 introduces past and new development of the instrument, as well as the general setup from the point of view of the sample gas flow. Section 3.1.2 explains the chemical ionization scheme, Sec. 3.1.3 the calculation of trace gas concentrations and Sec. 3.1.4 the typical operating procedures. Sections 3.1.5 and 3.1.6 contain a detailed description of the newly applied calibration methods. Characteristics of the AIMS data are given in Sec. 3.1.7 and Sec. 3.1.8 contains comparisons to other simultaneous measurements. Information on other instrument and model data sources is given in Sec. 3.2.

3.1.1. Development and setup

Mass spectrometry has been a widely used method for the analysis of atmospheric composition in terms of trace gases and aerosols, in appreciation of the generally high mass specificity and molecular sensitivity. A vast range of ionization techniques and mass spectrometer (MS) types are employed. Depending on the application, the capabilities are enhanced by the coupling of a gas chromatograph (GC). Together, mass spectrometric measurements are performed in all environments and target areas reachable by in-situ instrumentation, from ground- and vehicle-based air quality measurements to airborne, balloon-borne, rocket-borne and space-borne samplings.

The AIMS instrument (Fig. 3.1) is specifically designed for man-operated use aboard research aircraft. Its design has been developed in several stages in the group of Prof. Christiane Voigt, evolving from two converging development branches: the chemical ionization

Figure 3.1.: (a) The HALO research aircraft during the POLSTRACC campaign. The red arrow marks the inlet position for AIMS. (b) Detail of the top of the fuselage with four trace gas inlets. (c) The AIMS instrument inside the cabin. Tubing at the ceiling connects the inlets to the instrument.

(CI) scheme using sulfur pentafluorine ions (SF_5^-) as reagent ions was developed and successfully implemented by the National Oceanic and Atmospheric Administration (NOAA) (Marcy et al., 2004, 2005; Popp et al., 2009) and later adapted in an ion trap mass spectrometer at the Max Planck Institute for Nuclear Physics in Heidelberg (Jurkat, 2010; Jurkat et al., 2010). The quadrupole mass spectrometer part of AIMS is a commercial device by the company THS Instruments LLC. A detailed description of the instrument can be found in Kaufmann et al. (2016) and Jurkat et al. (2016).

Past development and use of the AIMS instrument for measurements of nitrous acid (HONO), HNO_3, HCl and SO_2 are extensively documented in the theses by Schäuble (2010) and Jeßberger (2013) and in Jurkat et al. (2014, 2017) and Voigt et al. (2010, 2014). In addition to these trace gas measurements, AIMS can be reconfigured without major changes to operate in a "positive ion" mode, which has been used for the detection of low concentrations of water vapour in the upper troposphere and lower stratosphere (UTLS) (Kaufmann, 2013; Kaufmann et al., 2016, 2018).

The setup of the instrument in the here used "trace gas" (i.e. negative ion) configuration is briefly introduced in order to serve as an updated reference for the following sections. More details and background can be found in the aforementioned literature. There have been some new developments since then within the scope of this thesis:

- The included calibration devices for HCl and HNO$_3$ were for the first time used in a long-term application over several months during the POLSTRACC campaign 2015/2016 (and equally in subsequent campaigns in the following years), allowing a long term monitoring of the stability of calibration devices and instrument performance. This enabled consistent measurements of trace gas concentrations over the course of long field missions and inter-annual comparability. More details can be found in Sec. 3.1.5.

- The envisioned "indirect" calibration of ClONO$_2$ was successfully applied and proved equally stable, enabling for the first time the joint in situ measurement of both chlorine reservoir gases, HCl and ClONO$_2$, in comprehensive aircraft deployments (Sec. 3.1.6).

- Detailed improvements in the hardware comprise the optimisation of sample gas transport in terms of in-flight procedures and inlet tubing heating, optimised tuning of the electrical supply of the ion source and a more reliable scroll pump drive train (Fig. 3.2).

Figure 3.2 gives an overview of the gas flow. A high current of ambient air is sucked into the aircraft cabin through an inlet with a backward facing opening, which effectively prevents particles (aerosol, droplets and ice crystals) from entry. The high flow ensures that the residence time inside the tubing is reduced to below one second (Jurkat et al., 2016) for quick response times. The tubing is made out of ½" PFA hoses and heated to a temperature of about 40 °C. Together, these measures try to minimize surface effects which can significantly impair the fraction of HCl and HNO$_3$ molecules transferred into the MS (Neuman et al., 1999). About a quarter of the ambient air flow is guided into the MS through an automatic pressure regulation valve. A stable pressure and temperature is necessary for constant chemical ionization rates inside the flow tube. The ion source and ionization scheme are treated in the following section. Created ions are guided through the mass spectrometer's three chambers by DC voltages. The speed relative to remaining neutral gas determines the rate of collisions, especially in terms of break-up of molecule-ion clusters. Octopoles focus the ion beam and the quadrupole, driven by DC and AC voltages, filters ions with a small range of mass-to-charge ratio[1], which eventually impinge on a channel electron detector ("channeltron") that counts the individual events.

---

[1]The range is ideally below $1\,u/e$, where u is the atomic mass unit and e is the elementary charge, in order to provide maximum separation/filtering of different ions.
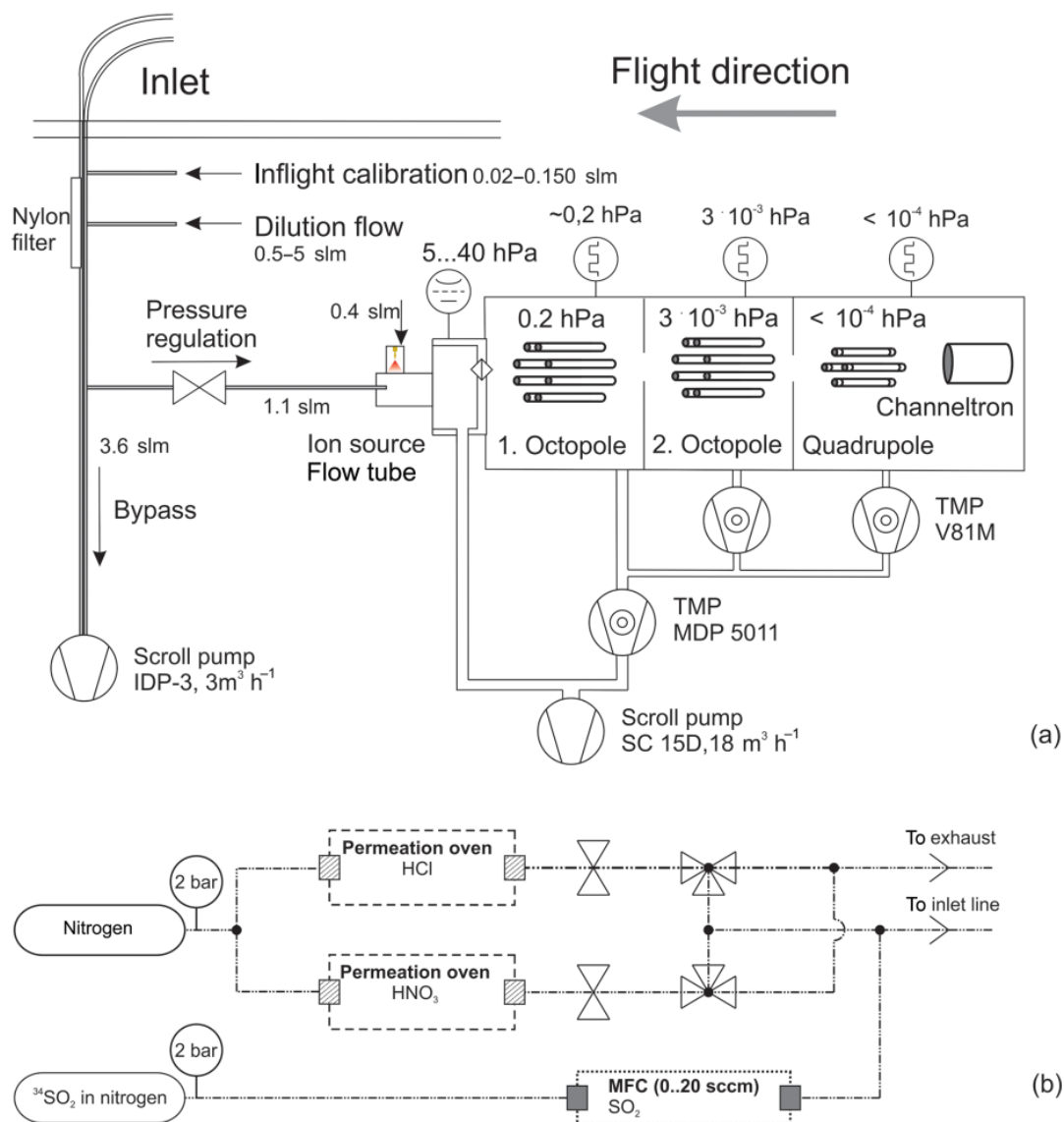
Figure 3.2.: (a) Schematic illustration of the gas flow in the AIMS instrument. From the inlet at the aircraft fuselage, ambient air enters the instrument via a pressure regulation valve. A high bypass flow ensures a high flow velocity and short response time. In the instrument, trace gases are ionized in the flow tube. Ions are guided by DC voltages towards the channeltron detector through three chambers separated by apertures. Octopoles focus the beam and the quadrupole separates the ions by their mass-to-charge ratio. (b) Detailed flow scheme of the in-flight calibration units. Figure from Jurkat et al. (2016).

3.1.2. Chemical ionization

Chemical ionization uses a dedicated species of so called reagent or educt ions[2] that subsequently ionize the desired neural trace gas molecules. Depending on the application, a variety of educt species are known. The trace gas configuration of the AIMS instrument is fed through the source gas inlet with a known and constant flow of trifluoromethylsulfur pentafluoride (SCF_8) together with inert nitrogen (N_2; typically 1500 ppbv to 3000 ppbv SCF_8 in N_2) as a carrier gas to provide a sufficiently fast flow. The SCF_8 compound, together with its precursor sulfur hexafluoride (SF_6), is itself a greenhouse gas with one of the highest global warming potentials of all gases (WMO, 2018). SCF_8 is highly inert and mainly decomposed upon an electron attachment, in the free atmosphere (Takahashi et al., 2002) and in the instruments discharge ion source, where an electron current is created via corona discharge at the tip of a gold needle set to a potential of -800 V. The products are trifluorocarbon (CF_3) and the desired $SF_5{}^-$ ions.

The design of the discharge ion source employed for the chemical ionization process is drawn in Fig. 3.3. It is described in detail in Jurkat et al. (2016). Relative to the design depicted therein, the geometry was changed in advance to the POLSTRACC campaign, in that the discharge gold needle was moved from the front (sample gas entry face) to the side of the flow tube chamber. The aim was to achieve a more efficient mixing of the reactant ions, injected through the hole at the discharge needle, with the sample gas. As the new geometry proved useful, it is now the standard ion source setup employed in the AIMS trace gas configuration.

The actual (soft) chemical ionization taking place in the flow tube utilises lower collision energies than the (harder) electron attachment in the previous step. This renders less fragmentation of the product ions, leading to a cleaner spectrum and higher sensitivity at the observed masses.

The essential ionization reaction has the form

$$X + SF_5{}^- \longrightarrow XF^- + SF_4, \tag{R 3.1}$$

which represents a fluoride transfer from an educt ion (here $SF_5{}^-$) to a trace gas ion, represented by the letter X. Explicitly written for the species treated in this work, reaction R 3.1

---

[2]The attributes "reagent" and "educt" are used interchangeably in this text and both refer to the $SF_5{}^-$ ions that serve as reagent partners on the educt (left) side of the fluoride transfer reaction R 3.1.
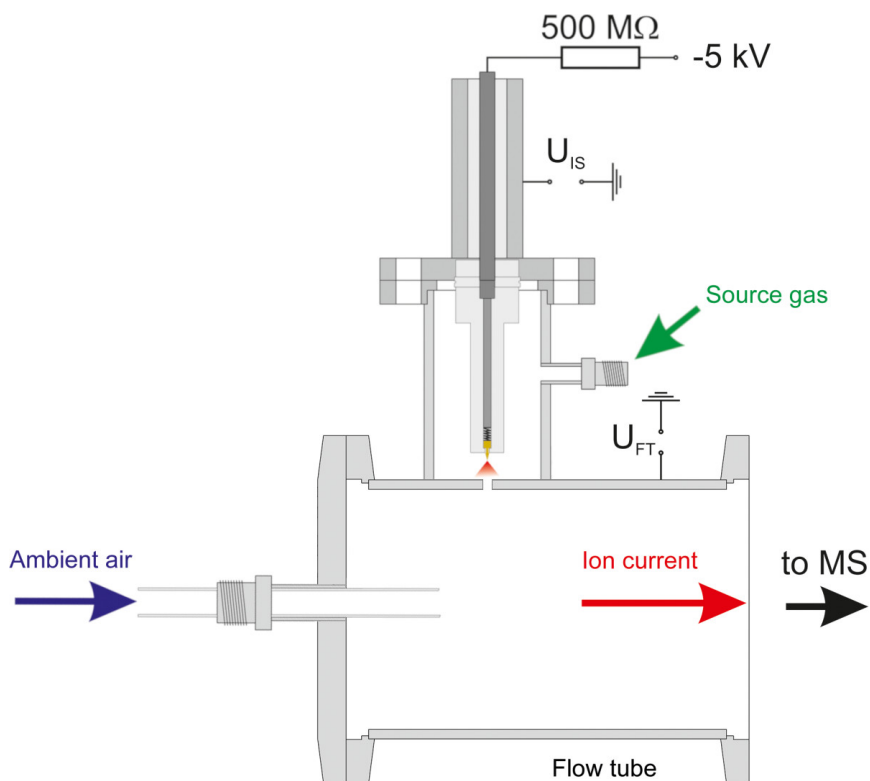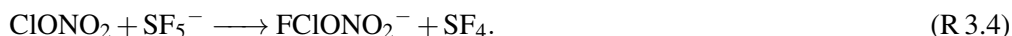
Figure 3.3.: Cutaway drawing of the discharge ion source and flow tube assembly as used during the POLSTRACC campaign. Modified figure from Jurkat et al. (2016).

reads (Jurkat et al., 2016; Marcy et al., 2005)

$$HNO_3 + SF_5^- \longrightarrow HFNO_3^- + SF_4, \tag{R 3.2}$$

$$HCl + SF_5^- \longrightarrow HFCl^- + SF_4, \tag{R 3.3}$$

$$ClONO_2 + SF_5^- \longrightarrow FClONO_2^- + SF_4. \tag{R 3.4}$$

The product ions, together with the remaining educt ions, on the righthand side of these reactions can be subsequently detected in the MS. Other reactions are possible however, e.g. a fluoride-chloride exchange involving HCl (Marcy et al., 2005), fragmentation of product ions, subsequent cross-reactions and cluster formation including other neutral compounds in the ambient air, predominantly water vapour (H_2O).

All electrostatic potentials, oscillation frequencies and pressures of the instrument are tuned and optimized in order to

(a) maximize the generation of desired product ions of reactions R 3.2 to R 3.4, i.e. the efficiency of these reactions with respect to the incoming atmospheric trace gases,

(b) maximize the sensitivity of detection for educt and all desired product ions,

(c) minimize fragmentation by careful tuning of the ion source voltage and minimize cluster occurrence by a proper ion drift velocity in the first MS chamber (collision-dissociation chamber, Fig. 3.2).

3.1.3. From ion count rates to concentrations

The relation between the number concentration $[X_i]$ of a species X_i in the sampled air derived from ion concentration in the MS will be shown in the following. Assuming first order reaction kinetics in reaction R 3.1, the formation of product ions $\frac{d[X_iF^-]}{dt}$ is proportional to the available number of reaction partners:

$$\frac{d[X_iF^-]}{dt} = k_i \beta \mu [X_i][SF_5^-] \tag{3.1}$$

with the reaction rate constant k_i. The additional factors represent dilution (β) and the transmission efficiency of the inlet line (μ), both of which may reduce the trace gas concentration on the way from the inlet to the ionization region. The reagent or educt ions are consumed in the same way:

$$\frac{d[SF_5^-]}{dt} = -\frac{d[X_iF^-]}{dt} = -k_i \beta \mu [X_i][SF_5^-]. \tag{3.2}$$

Assuming that only a small fraction of trace gas molecules are ionized, thus assuming that $[X_i]$ is available in excess and unchanged by the ionization, equation 3.2 can be integrated over the reaction time τ (i.e. the residence time of the ion-molecule mixture in the flow tube) to attain the time evolution of reagent ions:

$$[SF_5^-]_\tau = [SF_5^-]_0 \exp(-k_i \tau \beta \mu [X_i]). \tag{3.3}$$

This equation can now be solved for $[X_i]$. As for the loss of educt ions compensated by the generation of product ions, $[SF_5^-]_0$ can be replaced by $[SF_5^-]_\tau + [X_iF^-]_\tau$, which yields the ACIMS formula

$$[X_i] = \frac{1}{k_i \tau} \frac{1}{\beta \mu} \ln\left(\frac{[X_iF^-]_\tau}{[SF_5^-]_\tau} + 1\right). \tag{3.4}$$

As the count rate of the ions in the quadrupole mass spectrometer is proportional to their concentration[3], this formula can be used to determine trace gas concentrations from the mass spectrometric measurements.

Two remarks have to be made regarding formula 3.4: first, ions in a quadrupole mass spectrometer are subject to so called mass discrimination. That is, the transfer efficiency of in-

---

[3]or more precise, to their abundance

dividual ions from the entry to the detector depends on their mass, due to inertial effects on their undulating trajectories. A mass discrimination factor md for the count rates of each species can be applied to account for this differential transfer efficiency. Mass discrimination factors can be determined experimentally for certain masses using suitable ions with simple reaction schemes, and are then interpolated for the other masses. One mass for which $md = 1$ is selected as the reference mass. Second, the reagent ions are depleted by reactions with several trace gases at the same time. This reduces the amount of available reaction partners for each trace species and is reflected in the so called parallel ACIMS formula. From these two points, formula 3.4 can be rewritten in the more general form

$$[X_i] = \frac{1}{k_i \tau} \frac{1}{\beta \mu} \frac{md_i \, r(X_i F^-)}{\sum_j md_j \, r(X_j F^-)} \ln \left(\frac{\sum_l md_l \, r(X_l F^-)}{md_{SF_5^-} \, r(SF_5^-)} + 1 \right), \tag{3.5}$$

where md_i is the mass discrimination factor of the $X_i F^-$ ion and r are respective count rates.[4] The sum in the logarithm reflects the enhanced depletion of the reagent ions through all the fluoride transfer reactions, whereas the new fraction outside the logarithm determines the relative abundance of species X_i with respect to all the involved trace gases by the relative weight of the respective count rate.

A very useful simplification can be performed if gas flows and ionization rates are chosen such that only a small fraction of educt ions actually undergo loss through fluoride transfer. Then, employing the approximation $\ln(x + 1) \approx x$ for $x \ll 1$, a linearised form of the ACIMS formula reads

$$[X_i] = \frac{1}{k_i \tau} \frac{1}{\beta \mu} \frac{md_i}{md_{SF_5^-}} \frac{r(X_i F^-)}{r(SF_5^-)} = CF_i \cdot \frac{r(X_i F^-)}{r(SF_5^-)}. \tag{3.6}$$

Here, all the constant factors are collected in a single "calibration factor" CF_i that can be experimentally determined by a calibration with given concentrations of a trace gas.

3.1.4. Measurement procedure

Figure 3.4 displays a typical spectrum during a stratospheric flight section of HALO in the POLSTRACC campaign. The spectrum is obtained by a scanning measurement of the quadrupole mass spectrometer within a specified range and with a specified step size. The scan for the shown spectrum took 34 s. The single peaks of distinct mass-to-charge ratios are visible. The peak width is determined by the filter resolution of the quadrupole. The resolution is tuned to achieve optimal spectral separation of adjacent masses to minimize cross-sensitivity, while maintaining a high peak maximum for sufficient sensitivity and minimum

---

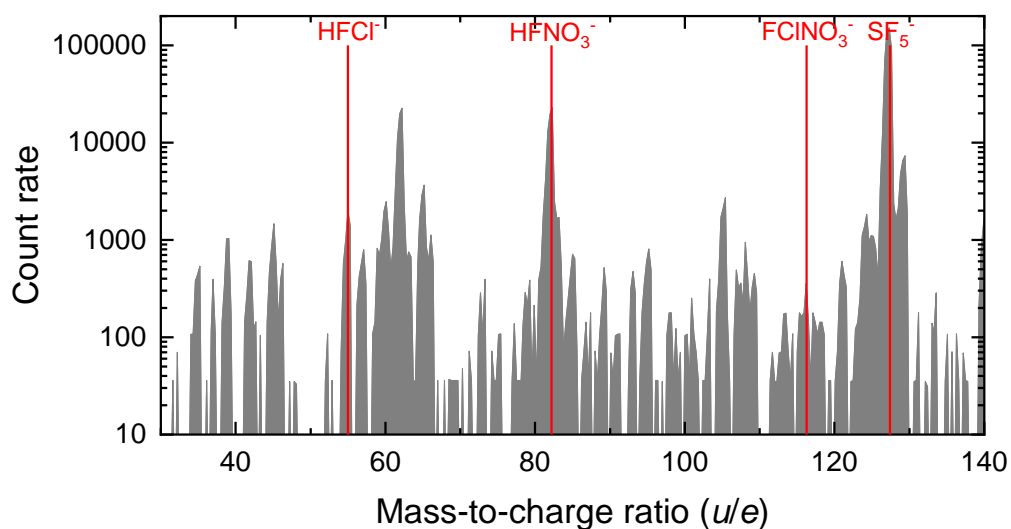[4]These count rates are already background-corrected, see Sec. 3.1.4.

Figure 3.4.: Spectrum of trace gases recorded by AIMS at typical atmospheric measurement conditions during POLSTRACC flight 14 (26 February 2016) at 15:08 UTC. Count rates denote the number of ion counts during each 100 ms dwell interval. The positions of the four principal masses for the evaluation in this work are highlighted correspondingly to Tab. 3.1.

noise. Such spectra are recorded periodically to monitor the tuning, as well as fragmentation and cluster formation.

Time series measurements of the ions in the MS are performed in the so-called "hop mode": Specified ions are sampled through repeated step-wise scanning through a predefined set of mass-to-charge ratios. In each step or hop, ion detection events are counted during a dwell time of usually 100 ms. The precise mass-to-charge ratios are selected from spectra during calibration periods where the maximum position of the generally broad mass peak is determined.[5] The overall time resolution for the entire set of 16 ions lies at about 1.7 s. Auxiliary ions that are recorded to monitor the correct ionization and dissociation reaction pathways can be sampled with reduced dwell times to minimise the time resolution.

Table 3.1 lists the set of ions recorded during the POLSTRACC campaign. A more comprehensive list of ions of interest in the AIMS trace gas configuration can be found in Jurkat (2010), from where parts of this table are extracted.

In contrast to laboratory experiments, measurements aboard a high-flying aircraft are subject to a highly variable environment, including variable airspeed from zero to $240\,\mathrm{m\,s^{-1}}$, temperature ranges of about 90 K, high pressure differences and highly variable humidity (water

---

[5]One would expect the maximum positions at integer multiples of u/e. However, as the tuning of the mass spectrometer may over time deviate from the perfect behaviour, it is often easier to shift the precise value of recorded mass-to-charge ratios instead of readjusting the whole spectrum.

Table 3.1.: List of ions recorded during the POLSTRACC campaign. All relevant ions are single charged, therefore they can be discerned solely by their atomic mass *m* (expressed in the atomic mass unit u). Lines set in bold type mark the ions for trace gas detection during the campaign.

Ion	m (u)	Purpose
Cl^-	35	fragmentation of $HFCl^-$
FHF^-	39	reaction with water
$Cl(H_2O)^-$	53	fragmentation of $HFCl^-$ (cluster)
$HFCl^-$	**55**	**detection of HCl**
$FHF(H_2O)^-$	57	reaction with water (cluster)
$HF^{37}Cl^-$	57	heavy isotopologue of $HFCl^-$
NO_3^-	62	fragmentation of $HFNO_3^-$
$HFNO_2^-$	66	detection of HONO
$HFNO_3^-$	**82**	**detection of HNO_3**
FSO_2^-	83	detection of SO_2
$F^{34}SO_2^-$	85	heavy isotope calibration of SO_2 measurement
$FClNO_3^-$	**116**	**detection of $ClONO_2$**
$F^{37}ClNO_3^-$	118	heavy isotopologue of $FClNO_3^-$
SF_5^-	**127**	**educt ion**
$^{34}SF_5^-$	129	heavy isotopologue of the educt ion

vapour changes by four orders of magnitude in the troposphere). Conditions inside the pressurized and air conditioned cabin may change during the flight and have to be monitored.

An example for a time series of count rates for the product ions related to HCl and HNO_3, together with the SF_5^- educt ions, during the POLSTRACC flight 13 is shown in Fig. 3.5, together with a ground calibration measurement before the flight. The mostly stratospheric HALO flight was conducted on 2 February 2016 out of Kiruna, Sweden and headed north for a high latitude survey and gravity wave observations over Svalbard. Grey shaded areas mark periods when background measurements were performed. This is achieved by adding a current of 2 slm (standard litres per minute) of dry synthetic air (i.e. a mixture oxygen and nitrogen at roughly the atmospheric composition of 20.9 % oxygen) to the flow entering the mass spectrometer, which is sufficiently high to suppress further sampling of atmospheric air from the inlet. This mode of operation serves two purposes: First, it is the standard mode whenever the instrument is run on the ground and below several (often about six) kilometres altitude[6], to avoid intake of very humid air in the lower troposphere and from low clouds, as water vapour strongly adsorbs on surfaces along the inlet line and in the mass spectrometer. This impairs the transmission of HNO_3 and also alters the ion spectrum through the formation of water clusters. Therefore, background measurements are always found at the beginning and at the end of a flight. Second, the actual quantitative measurement of background trace

---

[6]In aeronautical terms, "altitude" usually refers to the vertical distance to the mean sea level (MSL), whereas "height" refers to the vertical distance to the surface.
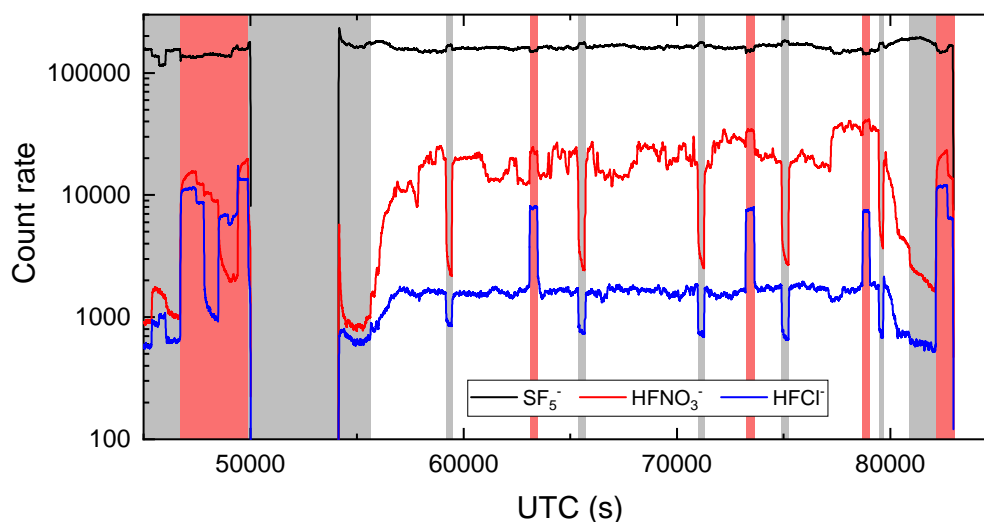
Figure 3.5.: Time series of selected ion count rates for the POLSTRACC flight 13 (2 February 2016) and the ground calibration before. Count rates denote the number of ion counts during each 100 ms dwell interval. Time is given in seconds of the day from midnight UTC. Grey shaded areas mark periods in the background measurement mode. Red shaded areas show calibration measurements. During the data gap from 50004 s to 54159 s UTC, the instrument was pumped without sample flow to minimize contaminations inside the chamber.

gas concentrations is essential, as this determines the amount of ion counts that is not directly related to sampling of outside air. These result from trace gas resorbing from the inlet line (which still occurs despite the measures mentioned above) and from other potential sources of erroneous counts, such as cross-sensitivities for neighbouring ions in the mass spectrum or electric noise.

Periodic background measurements are performed during each flight to monitor the course of the instrumental trace gas background. Also, these measurements are used to determine the instrument's detection limit.

3.1.5. Calibration of hydrogen chloride (HCl) and nitric acid (HNO₃)

Instrument calibrations are used to determine the calibration factor CF_i of species X_i in the linear formula 3.6. There are different calibration strategies, one is to feed a known concentration of the respective trace gas into the instrument. This has been done for HCl and HNO_3. The calibration signal appears on the same mass in the spectrum as the ions from the sample gas. By adding the calibration gas shortly behind the inlet, adsorption effects along the inlet line are readily covered by the calibration. Another strategy would use isotopically

labelled calibration gases using a naturally rare isotopologue of the sample gas. While being chemically quasi identical, the resulting ions appear at a different spectral position in the MS, enabling simultaneous ambient and calibration. The feasibility depends on the atmospheric isotopic composition and on the overall spectrum. For instance, isotopically labeled HNO_3 (using the ^{15}N atom instead of ^{14}N) would interfere with the FSO_2^- product ion (3.1, Jurkat et al., 2016). So far, isotopic calibration of AIMS has only been applied for SO_2 calibration using the $^{34}SO_2$ isotopologue (Voigt et al., 2014). The following paragraphs address calibration of the POLSTRACC dataset.

Calibration of HCl and HNO_3 measurements are performed using permeation tubes. In each of the two devices, a small permeation glass tube contains an azeotrope solution of the respective substance in water. For a defined temperature the gas phase above the solution contains equal portions of the mixed substances as the solution. Gaseous HCl or HNO_3 diffuse through a semi-permeable membrane. Evenly heated to a specific temperature, each tube generates a constant partial pressure of trace gas, which gives a constant flow of molecules through the membrane. Inside the permeation oven, the calibration gas is diluted and carried by a nitrogen flow of $75\,ml\,min^{-1}$ to the inlet line. The permeation rate of the tubes was determined several times during each campaign for control and to account for possible drifts due to ageing or contamination. Therefore, the trace gas/nitrogen flow is entered into two a washing bottle filled with water, where all trace gas molecules are adsorbed by the water. As both acids strongly dissociate in water, the amount of trace gas accumulated over several days can be determined through an ion chromatographic measurement of the concentration of Cl^- and NO_3^- ions (a service performed by the company Currenta GmbH & Co. OHG).

Figure 3.6 shows the washing bottle with gas entered through a dispenser into the water (generation of bubbles), together with the permeation oven in the back of the picture. The determined permeation rates are shown in Fig. 3.7. The $\pm 10\,\%$ error bars reflect the assumed combined uncertainty for the bubble process and the ion chromatography. The permeation devices were usually run at $52\,°C$ for HCl and $40\,°C$ for HNO_3. However, for runs on 4 December 2015 and 16 June 2016, the HNO_3 permeation temperature was lifted to $50\,°C$ (with at least one day of accommodation before the measurement) to check the change of perme-
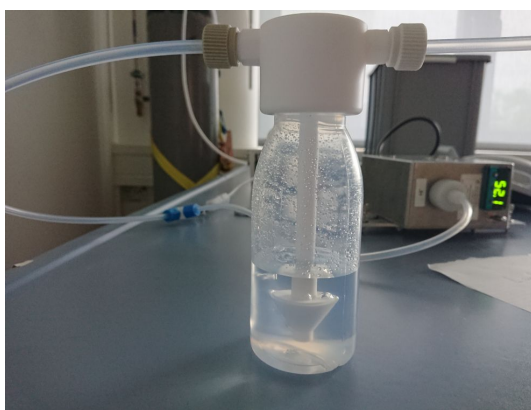

Figure 3.6.: Washing bottle with HCl permeation device in the background. At the liquid-gas interface of the (nitrogen) bubbles the trace gas molecules are transferred into the water for further quantification.
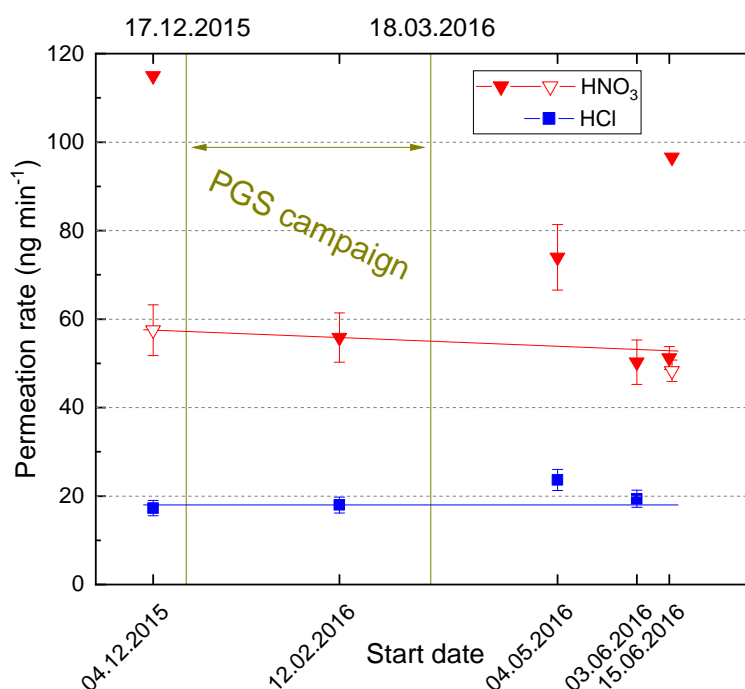
Figure 3.7.: Result of permeation rates of HNO_3 and HCl (squares and triangles) in nanograms per minute. On 17 December 2015 and 16 June 2016, the HNO_3 permeation device was heated 10 K above normal (see text). Open triangles show the respective half value. Error bars stretch $\pm 10\%$ or $\pm 5\%$ (only 15/16 June 2016) of the total value. Explanation for the "regression" lines is given in the text.

ation rate with increasing temperature. Assuming a common doubling of reaction rates with a 10 °C temperature increase, half the value of the measured permeation rates fits the other values very well within the limits of uncertainty (empty triangles in Fig. 3.7). The HNO_3 data on 15/16 June 2016 represent an independent measurement where the permeation device was coupled in house to the SIOUX NO_y chemiluminescence detector (Voigt et al., 2005). The SIOUX instrument uses a gold converter heated to 300 °C that converts all nitrogen oxides (NO_y) into NO. With an artificial excess of ozone and through the reaction $NO + O_3 \longrightarrow NO_2{}^* + O_2$, the intensity of the infrared emission of the excited $NO_2{}^*$ returing to the ground state is measured. There, the uncertainty in the total value is estimated at $\pm 5\%$. These independent measurements fit quite well in the series of ion chromatographic measurements and support the validity of the process.

Permeation rates seem to be almost constant during the POLSTRACC campaign. For HNO_3, a linear relationship with a trend of $-0.0024\ \mathrm{ng\,min^{-1}\,d^{-1}}$ was determined from the first two measurements, which were closest to the campaign period. For HCl, the measurements suggest a minor positive trend, which seems unphysical in view of the always constant tempera-

ture. Therefore, the value measured on 12 February 2016 is assumed valid for the campaign period (i.e., no trend), and it still lies within the errorbars of the first and the last measurement. The data from 4 May 2016 are well above all other values for each HCl and HNO_3, so the author supposes there must have been some kind of wrong handling of the water samples. These values were not considered in the trend estimation.

Having the permeation rates, the precise gas flow rates need to be known as well in order to calculate the proper concentration and dilution of trace gases. The gas flow is controlled by various critical orifices (passive) and mass flow controllers (MFC, active), all of which were gauged and calibrated appropriately (for MFC calibration see the Appendix).

Now for the actual calibration of the mass spectrometer, red shaded areas in Fig. 3.5 highlight the two types of calibration measurements: ground calibration (before 50000 UTC and immediately after the flight at the very end of the time series) and in-flight calibration (three short events). Ground calibrations are performed by adding the permeation gas flow to the background synthetic air flow. Different mixing ratios can be set by further dilution with more synthetic air. This produces the stepwise pattern in Fig. 3.5. It can be seen that an equilibrium state is reached only after a certain accommodation time, which is between 5 and 30 min. From every step a single mean equilibrium count rate is extracted by averaging the values from within the last 30 s.

Figure 3.8 displays the ground calibration measurements during the POLSTRACC campaign for HNO_3 in terms of relative count rate versus concentration. One series of measurement taken on 17 January 2016 is highlighted as black squares. According to Eq. 3.6 the slope of a linear function along these values should give the inverse calibration factor, $CF^{-1}_{HNO_3}$ which is also called the sensitivity s_{HNO_3}. In the sketched case, the slope is $0.022(1)$ /ppbv. It can also be seen that the y-axis intercept is reasonably close to zero and that the assumption of linearity leading up to the simplified relation in Eq. 3.6 is valid even for the highest sampled concentrations.

Additionally Fig. 3.8 shows that the minimum concentration that can be calibrated is 4 ppbv HNO_3. Ideally the HNO_3 calibration should be extended to lower concentrations that better represent atmospheric conditions found in the polar UTLS. However, this was due to the measurement setup not possible in this configuration. Higher dilution flows or different permeation rates would have generated lower concentrations but are often related to higher errors without significant improvement for the calibration. Furthermore, the grey dots in Fig. 3.8 show that there is a large variation between different ground calibration measurements of about 50 % of the maximum value. This is most likely due to limited time and limited flow through the hoses, such that accommodation is incomplete and therefore the equilibrium of the plateaus was often not reached. Therefore ground calibrations should not be taken alone to determine the sensitivity, but are useful to monitor the state of the instrument and the
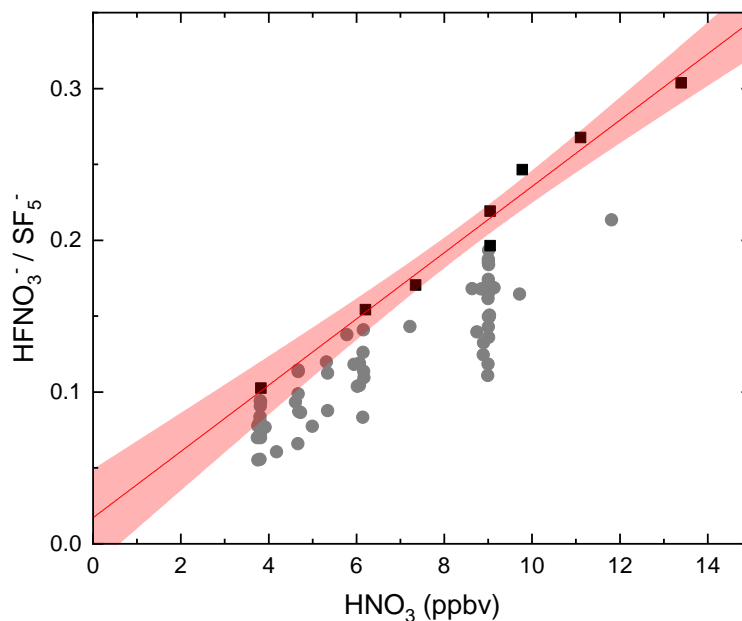
Figure 3.8.: Ground calibration of HNO_3. Points denote singular (averaged, see text) measurements of the $HFNO_3^-/SF_5^-$ ratio versus the given trace gas concentration. Black squares highlight a series of ground calibration measurements on 17 January 2016. The red line is a linear fit to this series, together with the 95 % confidence interval.

linearity over the range of concentrations. The picture is similar for HCl, except that calibration can be performed at lower concentrations closer to the atmospheric reality due to the lower permeation rate. The values also tend to show a little bit less spread as transmission is faster.

In-flight calibrations are performed by adding the permeation gas flow to the stream of atmospheric air that is sucked into the cabin. This increases the concentration of HCl and HNO_3 and is visible as a step in the count rates. After a short accommodation, the increased count rate is evaluated as aforementioned. It is beneficial to perform these calibrations at a predictably rather constant atmospheric trace gas concentration, for instance during constant flight legs, and to keep them short to save precious measurement time. Assuming linear instrumental response, the sensitivity can be deduced from the step height of the calibration count rates over the atmospheric background.

The advantages of the in-flight calibrations are as follows: The entire inlet flow (bypass + vacuum chamber) is about 5 slm. Considering the lower density of air at flight altitude, this constant mass flow is achieved by a higher flow velocity than on ground. Both the high mass

flow and the enhanced velocity lead to reduced residence and wall contact times of the air in the inlet line. Therefore the accommodation during in-flight calibration is much faster. Besides, the calibration directly images the state of the instrument at the given atmospheric conditions.
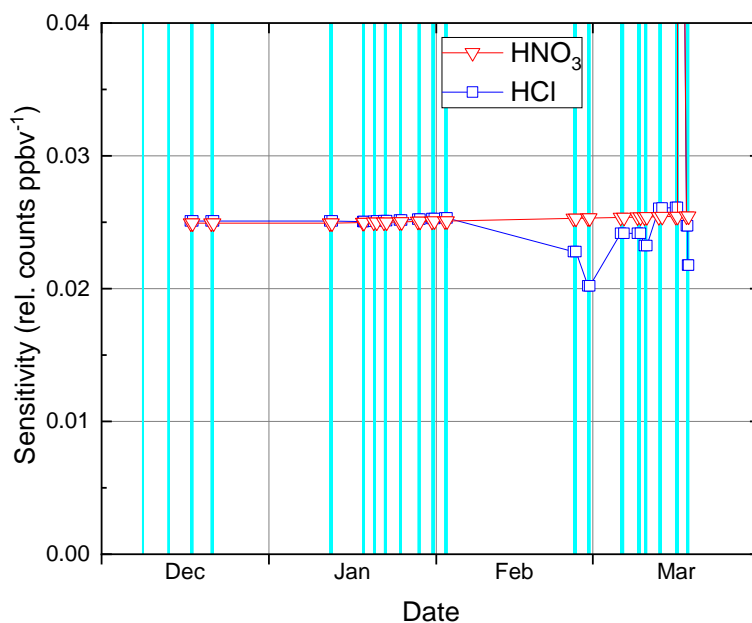

Figure 3.9.: Applied sensitivity values for HCl and HNO$_3$ throughout the POLSTRACC campaign. Light blue shading indicates the time of the HALO flights.

Figure 3.9 displays the deduced sensitivities s_{HCl} and s_{HNO_3} for the POLSTRACC campaign. They are mainly derived from in-flight calibration and take a rather constant value, both at about $0.025\,\mathrm{ppbv^{-1}}$. For HNO$_3$ there is a slight positive tendency over the months, which reflects and overall improving performance of the instrument, as residual contaminations are gradually removed. This course is also generally true for HCl. In the second phase beginning in late February, however, a significantly reduced sensitivity was derived and has to be assumed. This can be explained by water that has entered the inlet line during the campaign break before, and that reduces the production of pure HFCl$^-$. An outlier value of $0.1\,\mathrm{ppbv^{-1}}$ for both sensitivities on 16 March 2016 (out of range in Fig. 3.9) is due to a malfunction and short-term repair on the instrument.

3.1.6. Calibration of chlorine nitrate (ClONO$_2$)

Chlorine nitrate (ClONO$_2$) is measured similar to HCl and HNO$_3$, including the background measurements. A likewise direct calibration, however, is technically much more challenging: Brauer (1960) describes two synthesis pathways through dichlorine monoxide (C$_2$O) and dinitrogen pentoxide (N$_2$O$_5$) or through chlorine monofluoride (ClF) and HNO$_3$. Both involve high vacuum containers and cooling with liquid air or nitrogen. The former pathway is illustrated in Wagner and Birk (2003) and the produced ClONO$_2$ was used there to sample reference absorption cross sections in the infrared spectrum that have since been used in remote sensing instruments like MIPAS-B (Wetzel et al., 2010) and GLORIA (Rothman et al., 2013; Ungermann et al., 2015). Storage and transport of ClONO$_2$ on the ground require cooling to lower the vapour pressure, ideally glass surfaces to prevent heterogeneous loss reactions and shielding from decomposing UV radiation (Goldfarb et al., 1997). Efforts have not yet been undertaken to supply AIMS in such a way due to the necessary mobility of the instrument.

Instead, the ClONO$_2$ calibration is founded on work by Marcy et al. (2005) who performed laboratory calibrations of HCl, HNO$_3$ and ClONO$_2$ with a similar quadrupole mass spectrometer, using the same SF$_5{}^-$ reaction ions. They report values for all sensitivities s_i. The similar setup considering the flow tube, quadrupole and detector allows to assume similar ionization and detection characteristics between the laboratory and the AIMS instrument. Therefore the sensitivity s_{ClONO_2} for AIMS is inferred using known s_{HCl} or s_{HNO_3} and the relative sensitivities from Marcy et al. (ibid.). Using HNO$_3$ is preferred here over HCl as the structure of the molecule and the ion is more similar to the ClONO$_2$ counterparts. One obtains $s_{ClONO_2} = \dfrac{2.0}{5.4} s_{HNO_3}$. Furthermore the unique mass discrimination of AIMS has to be considered (Sec. 3.1.3). Therefore the mass discrimination factor for HFNO$_3{}^-$ was defined as md$_{HFNO_3{}^-} = 1$. Then the md factor for the educt ion on mass 127 u can be measured from the reduction of transmitted educt ions at a high concentration of HNO$_3$ and hence produced HFNO$_3{}^-$ ions. Linear interpolation to the mass 116 u of the FClNO$_3{}^-$ product ion gives md$_{ClONO_2} = 2.08$.

3.1.7. Detection limit, precision and accuracy

Finally, the time series of trace gas concentrations from the AIMS measurements has been calculated for all POLSTRACC flight. These time series still feature noise that may cover atmospheric features. The noise is a combined effect by intermittency in the arrival of the ions at the detector due to not perfectly stable ionization conditions, resorbed molecules from the inlet line, electric noise in the detector and the various potentials in the MS, and potential sensitivities to other ions at the specific mass. Therefore the data were smoothed using a 10

data points wide running average window, that is, a width of 17 s. This setting proved to be a reasonable tradeoff between time resolution and enhanced signal-to-noise ratio.

The detection limit (smallest detectable change in mixing ratio) can be expressed in terms of the standard error of the signal during a background measurement. It is reduced by the running average by a factor $\sqrt{N}$ where N is the window width. For the POLSTRACC data with the above settings, the 1σ detection limit is 6 to 12 pptv (parts per trillion) for HCl and ClONO$_2$ and 9 to 28 pptv for HNO$_3$. This varies over time depending on the overall performance of the instrument. Likewise, the statistical precision is 10 to 15 % for all species. The accuracy is estimated with 12 % for HCl, 16 % for HNO$_3$ and 20 % for ClONO$_2$. It reflects the systematic uncertainties involved with the calibration gases, the ion chromatographic concentration analysis, gas flow errors and the uncertainty in the indirect ClONO$_2$ calibration (Jurkat et al., 2016, 2017; Marcy et al., 2005).

3.1.8. Data comparison and verification

The measurement of AIMS during the POLSTRACC campaign were compared to simultaneously collected data from a number of other instruments to check for consistency in congruent measurements and for verification of less certain observation.
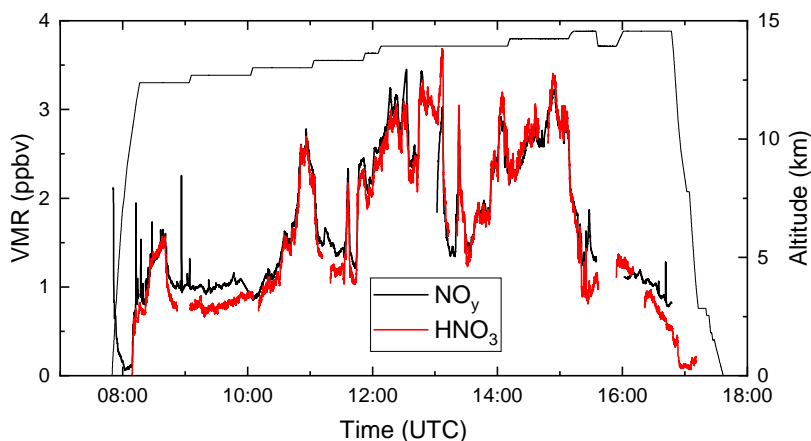

Figure 3.10.: Comparison of HNO$_3$, measured by AIMS, to NO$_y$, measured by AENEAS, during POLSTRACC flight 05 on 21 December 2015. The flight altitude is displayed for context.

The first comparison is the AIMS HNO$_3$ versus the total nitrogen oxides (NO$_y$) measurement by AENEAS, provided by Helmut Ziereis. The AENEAS (or IPA-NOy) instrument is a chemiluminescence detector for nitrogen oxides (Ziereis et al., 2000), similar to SIOUX
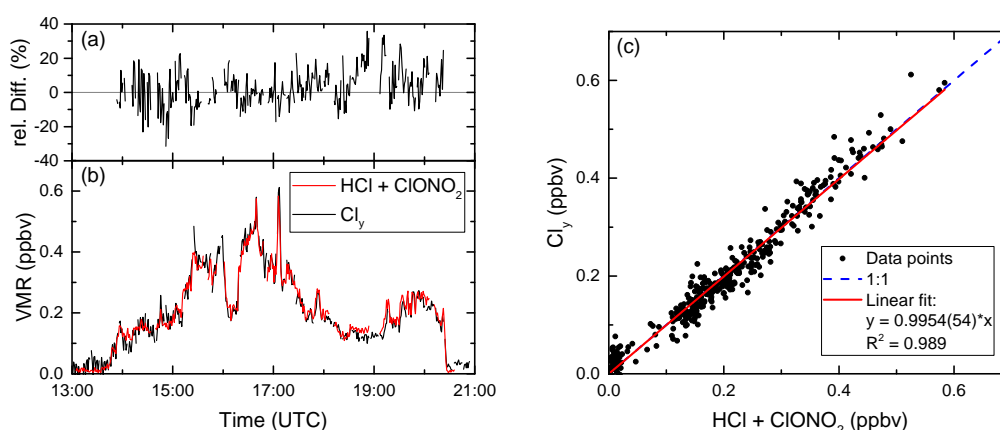
Figure 3.11.: Comparison of the sum of HCl and ClONO$_2$, measured by AIMS, to Cl$_y$, inferred from GhOST measurements, during POLSTRACC flight 04 on 17 December 2015. (a) Difference between both curves relative to Cl$_y$ and (b) timeline of mixing ratios over the whole course of the flight. (c) Correlation between added AIMS measurements and Cl$_y$. Figure taken from Marsing et al. (2019).

mentioned before. Figure 3.10 shows the time series of HNO$_3$ and NO$_y$ measurements during flight 05 of the POLSTRACC campaign on 21 December 2015. The flight was conducted from Oberpfaffenhofen, Germany and headed to Svalbard and back for an early winter survey of the polar vortex. This included stratospheric flight sections at different latitudes and potential temperatures. Measured HNO$_3$ levels reached up to 3.6 ppbv (with ozone topping at 940 ppbv, not shown). The comparison of HNO$_3$ to NO$_y$ revealed that both measurements are in generally good agreement within the limits of uncertainty, especially deep in the stratosphere. The general shortfall of HNO$_3$ versus NO$_y$ above 2 ppbv (well visible past 12:00 UTC) can be explained by ClONO$_2$ at about 10 to 15 ppbv. The larger deviations especially at the beginning and at the end of the flight, are rather due to the presence of tropospheric NO$_x$. Peaks where HNO$_3$ even exceeds NO$_y$ at around 14:00 UTC and 15:00 UTC likely represent a saturation effect in some peak NO$_y$ measurements.

After verification of HNO$_3$ fitting consistently into the NO$_y$ budget, the next comparison targets the closure of the total inorganic chlorine Cl$_y$ budget, which is crucial for the analysis further below. Therefore, observations from the GhOST gas chromatography-mass spectrometer (Sala et al., 2014) by Andreas Engel are used. Cl$_y$ is inferred through a stratospheric correlation from measurements of dichlorofluoromethane (CFC-12) with a precision of 0.2 %. For further details on the correlation, see Marsing et al. (2019). Figure 3.11 displays a comparison of AIMS and GhOST data data for flight 04 of the POLSTRACC on 17 December 2015. The flight from Oberpfaffenhofen was headed to the Atlantic Ocean north of Ireland with horizontal cuts of the tropopause. As the polar vortex was only sparsely hit and no
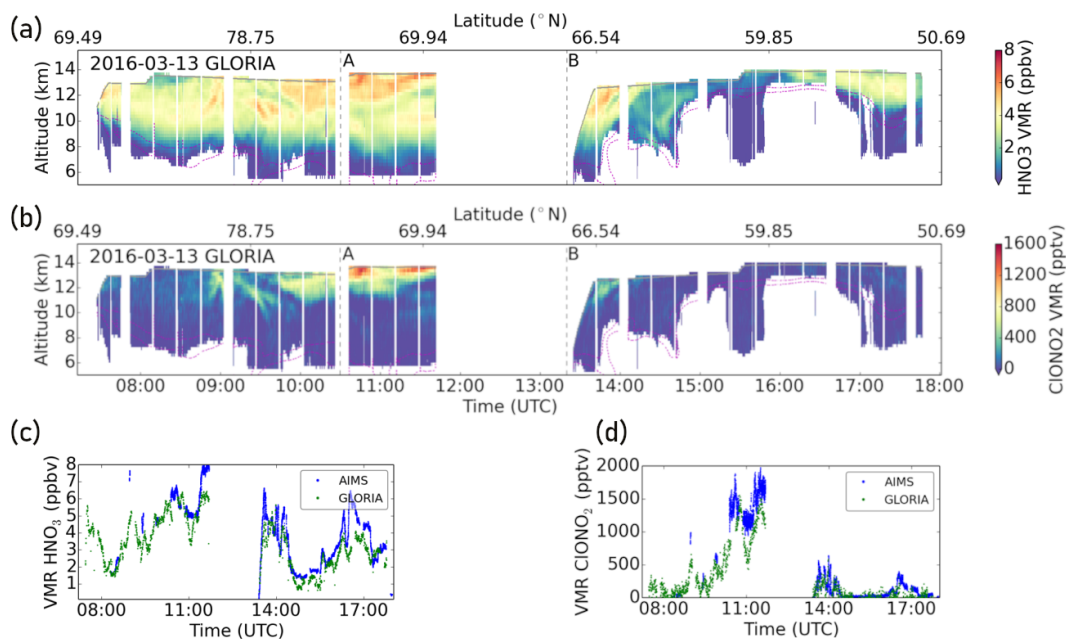
Figure 3.12.: (a) and (b) Curtain plots of HNO_3 and $ClONO_2$ mixing ratios (shading) from the GLORIA instrument versus time and altitude during POLSTRACC flight 19 on 13 March 2016. The top altitude corresponds to HALO's flight path. Clouds induce data gaps at lower altitudes. (c) and (d) For the same species, time series of simultaneous in situ measurements by AIMS and the closest GLORIA data. Figure adapted from Johansson et al. (2018).

chlorine activation occurred in the lowermost stratosphere at this early stage of the vortex development, chlorine was expected to be partitioned entirely into the reservoir species HCl and $ClONO_2$. This is corroborated by Fig. 3.11, where HCl + $ClONO_2$ agree within $\pm 20\%$. Larger deviations are only found in tropospheric sections of the flight, where the correlation of CFC-12 and Cl_y is less robust due to tropospheric sources. The result of the overall excellent agreement is used below, where any difference between the reservoir species measured by AIMS and Cl_y from GhOST represents activated chlorine species (ClO_x).

To end with, in situ measurements are always valuable test points for the verification of remote sensing data. In this sense, AIMS HNO_3 and $ClONO_2$ measurements have been used to assess the quality of the respective measurements by the GLORIA limb infrared spectrometer (Ungermann et al., 2015). Limb measurements of infrared emissions by Sören Johansson provide a slant "curtain" of trace gas concentrations below and to the side of the HALO aircraft. Figure 3.12 shows in panels a and b two exemplary time-altitude curtains of HNO_3 and $ClONO_2$ from POLSTRACC flight 19 on 13 March 2016. The flight from Kiruna with intermediate stop in Kangerlussuaq, Greenland targeted a low stratosphere on the northern westbound leg and a high tropopause on the southern return leg. The difference is

clearly visible in the trace gas concentrations. Figure 3.12c and d compare the uppermost data points of GLORIA, where the information originates closest to the aircraft, to the AIMS in situ measurements. While both instruments observed similar features[7], differences in HNO_3 reach up to 2.0 ppbv at some locations and $ClONO_2$ is underestimated by 200 to 500 pptv (Johansson et al., 2018). One reason for these differences is that the largest contribution to the considered GLORIA data points still comes from air masses slightly below and next to the aircraft. Another reason would be enhanced atmospheric variability along the line of sight of GLORIA in certain locations that negatively affect the comparability to in situ measurements. Nevertheless, some agreement in more homogeneous environments provides a valuable hook for the complex retrieval of the remote sensing data.

3.2. Other data sources

This section very briefly covers the other instruments from the POLSTRACC campaign which provided data for the study in this thesis, as well as the involved model. Those data and model results were provided by the individual teams as referenced below and they were not acquired within this thesis.

The previous section already introduced the GhOST gas chromatography-mass spectrometer by Andreas Engel, which is used to derive total inorganic chlorine (Cl_y). Another crucial contribution are precise and high resolution measurements of nitrous oxide (N_2O) that are needed in the in situ method for the identification of polar vortex air (Sec. 4.2.1). N_2O was measured by Peter Hoor using the three-channel quantum cascade laser infrared absorption spectrometer TRIHOP (Müller et al., 2016). The integration time was 1.5 s with a precision of 1.84 ppbv (Krause et al., 2018). Afther linear drift correction, the total uncertainty of N_2O during the POLSTRACC campaign is estimated to be 2.5 ppbv.

Simulations were performed by Jens-Uwe Grooß with the Chemical Lagrangian Model of the Stratosphere (CLaMS) that is described elsewhere (Grooß et al., 2014, and references therein). Unlike most other Eulerian models, the Lagrangian chemical transport model CLaMS calculates the chemical composition along air parcels irregularly distributed over space that individually follow their trajectories. The underlying wind and temperature data are taken from ECMWF ERA-Interim data (Dee et al., 2011). Initialisation and boundary conditions of the model simulation for the winter 2015/2016 are described by Grooß et al. (2018). Typically, the model output is written every day at 12:00 UTC. For interpolation to the observation locations and times, a Lagrangian mapping was used, employing back trajectories from the desired positions and times to the previous day. The interpolated model output

---

[7]Both in situ and GLORIA observations are much more fine scaled than comparable satellite measurements, revealing, for example, the structure of the tropopause or stratospheric intrusions.

is then taken as the initial state for the CLaMS chemistry module integrated forward to the observation point. With that procedure, the chemical composition (including the simulated chlorine partitioning) at the observation location and time is determined from the model.

4. Chlorine partitioning in the Arctic lowermost stratosphere

This chapter treats the partitioning of inorganic chlorine species using the in situ measurements during the POLSTRACC campaign, targeting a proof to the two hypotheses by addressing the following questions: In how far does chlorine partitioning in the polar LMS differ from the free stratospheric evolution? What unique characteristics can be observed? The chapter is structured as follows: An introduction to the aircraft campaign and the measurement strategy is given in Sec. 4.1. Section 4.2 introduces the method to identify air masses that belong to the polar vortex. Section 4.3 covers the evolution of the partitioning throughout the measurement period and at different altitudes. Both these sections are for the most part published in Marsing et al. (2019). Parts of Sec. 4.4 that contains a case study of a single flight witnessing unusually high Cl_y and ClO_x are also published in Oelhaf et al. (2019).

4.1. The Arctic winter 2015/2016 and the POLSTRACC campaign

The polar vortex that evolved in the Arctic winter 2015/2016 was extraordinarily strong, meaning that unusually low planetary wave activity in the northern hemisphere in November/December 2015 posed little resistance to the acceleration of the circumpolar zonal wind band in the stratosphere and mesosphere, which cut off the polar air masses from the lower latitudes (Matthias et al., 2016). The (stratospheric) vortex air masses cooled to record-breaking low temperatures (Manney and Lawrence, 2016). This enabled the widespread formation of polar stratospheric clouds (PSCs) of different types, even ice clouds (Voigt et al., 2018), which is much more common in the typically stronger and colder Antarctic vortex. Such extreme conditions enable physical and chemical reactions in the atmosphere to proceed at previously unseen pace and extent. It is essential for current understanding and future projections to consistently track the effects in observations and modelling.

In this interesting synoptic setting, the German research aircraft HALO was deployed on the POLar STRAtosphere in a Changing Climate (POLSTRACC) mission (Oelhaf et al., 2019).
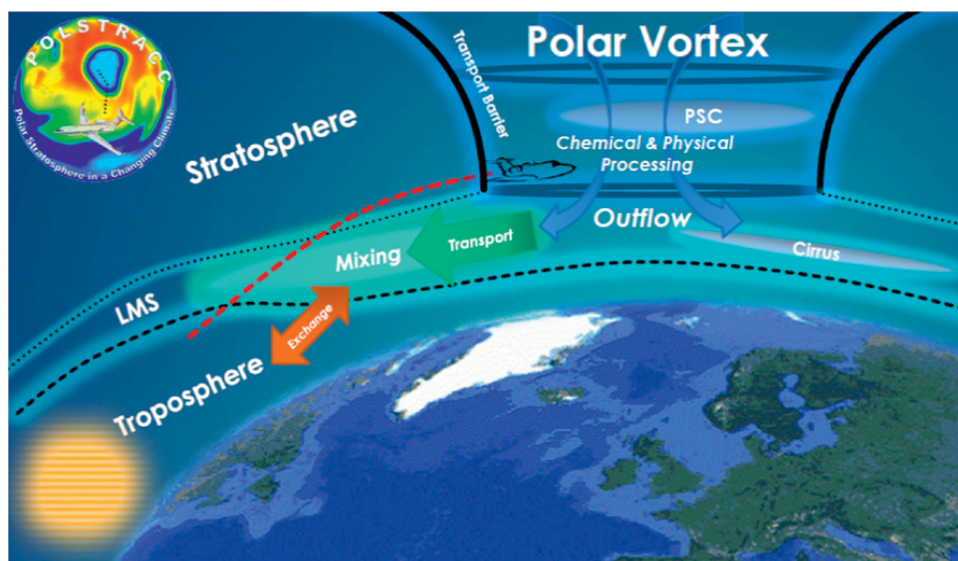
Figure 4.1.: Figurative latitude-altitude representation of the target area for the POLSTRACC mission. The flights attempted to cross the lowermost stratosphere (LMS) at various latitudes with sampling of the adjacent troposphere and intra- and extra-vortex stratosphere (red dashed line). Transport barriers exist at the tropopause (black dashed line) and around the polar vortex (solid line). Polar stratospheric clouds (PSCs) are visual features of the vortex and play a key role in chemical processing. Arrows indicate dominant transport and mixing processes. Figure taken from Oelhaf et al. (2019).

For synergistic reasons, the aircraft campaign was conducted as a joint effort of the POL-STRACC mission together with the GW-LCYCLE (Gravity Wave Life Cycle Experiment, Wagner et al. (2017)) and SALSA (Seasonality of Air mass transport and origin in the Low-ermost Stratosphere using HALO Aircraft) research programmes. The joint research flights were conducted under the acronym "PGS".

As a first comprehensive aircraft mission in the Arctic lowermost stratosphere (LMS) spanning the entire winter-spring season, POLSTRACC was designed to address four main goals, that are also illustrated in Fig. 4.1:

1. Quantification of transport and mixing in the lower polar vortex and in structures with the coupled extra-vortex stratosphere and upper troposphere.

2. Study of polar stratospheric clouds, cirrus and redistribution of nitric acid in the Arctic winter stratosphere.

3. Investigating of the chemistry of ozone-depleting chlorine and bromine compounds.

4. Quantification of ozone loss.

The research aircraft HALO (High Altitude and LOng Range), a Gulfstream G550 twin-engine jet, served as a well suited platform, providing about 10^4 km range and a 15 km ceiling altitude for a potential 3 tons of payload. In total 18 scientific flights were performed between 17 December 2015 and 18 March 2016. They were arranged around focus periods, targeting the early winter, midwinter and late winter/spring seasons in the Arctic. Most flights were based in Kiruna, Sweden, providing a high-latitude entry at 68 °N. The entire campaign's flight tracks cover a region between 25 to 87 °N and 80 °W to 28 °E over Europe, the North Atlantic and Greenland. Vertically, potential temperatures up to 411 K were reached.

The aircraft was equipped with a set of 13 in situ and remote sensing instruments for the measurement of meteorological parameters, trace gas concentrations, cloud water and nitrogen oxides content and aerosols (Oelhaf et al., 2019). This compilation proved very constructive and was adapted with minor changes for the later HALO missions WISE (2017) and SouthTRAC (2019).

The campaign provided data for a number studies: Parts of the chlorine partitioning study in this thesis are published in Marsing et al. (2019). A remote sensing and simulation perspective is given in Johansson et al. (2019) and the characterisation and validation of the GLORIA $ClONO_2$ measurements (inter alia) was performed in Johansson et al. (2018). Mixing at the lower vortex edge was investigated by Krause et al. (2018). Nitrification of the LMS was the topic of Braun et al. (2019), while Keber et al. (2020) observed the injection of bromine into the UTLS. Voigt et al. (2018) reconstructed the exceptionally widespread occurrence of ice PSCs. Gravity waves, especially those excited by mountain orography, were studied by Dörnbrack et al. (2017) and, by means of a novel tomography technique, by Krisch et al. (2017) and Krisch et al. (2020). Woiwode et al. (2018) investigated the tropopause structure and Woiwode et al. (2020) the moist bias of numerical weather forecasts in the LMS. A model perspective on vortex processing and transport in this Arctic winter is given by Khosrawi et al. (2017). Further highlight findings can also be found in the overview publication (Oelhaf et al., 2019).

4.2. Vortex identification

The following two sections introduce the methods that were applied in order to identify air masses from the polar vortex. The methods differ between the in situ measurements and the model perspective due to the different available data space, but aim at selecting corresponding subsets of data in the most suitable way, respectively.
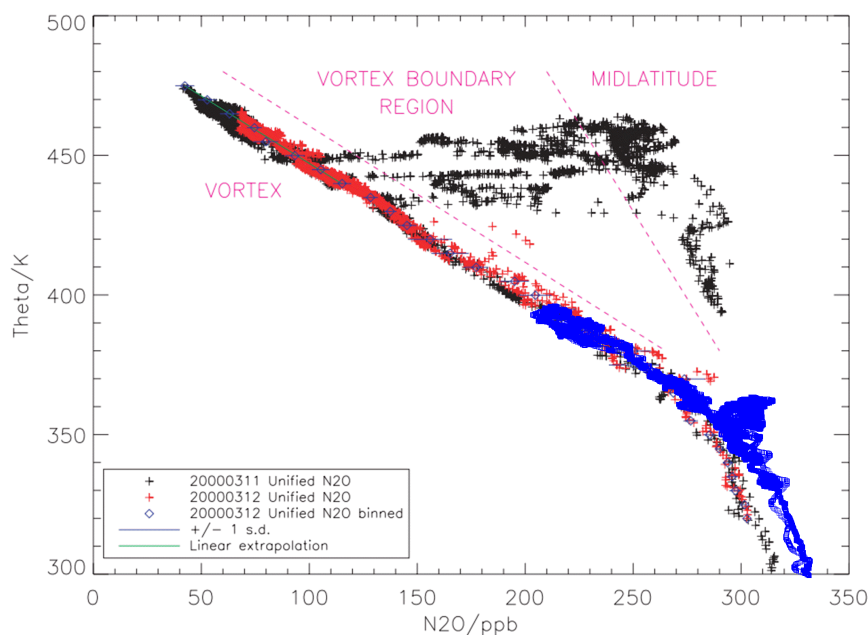
Figure 4.2.: Polar vortex identification by profiles of N_2O concentration versus potential temperature (Theta). Black and red crosses indicate measurements from two different flights of NASA's ER-2 high altitude aircraft during the 2000 SOLVE/THESEO mission, complemented by blue boxes for the POLSTRACC HALO flight 14 on 26 February 2016. The assignment of the measurements to the different origins of air masses is explained in the text. Figure adapted from Greenblatt et al. (2002).

4.2.1. Identification of vortex air by in situ measurements

A common means for vortex identification in the three-dimensional space of atmospheric parameters is the Nash criterion (Nash et al., 1996), essentially defining the location of the vortex edge by the maximum gradient of potential vorticity (PV) on isentropic surfaces. In this work, however, the method of Greenblatt et al. (2002) is applied where vortex air is identified by a tight correlation between the inert tracer N_2O and potential temperature. The principle can be seen in Fig. 4.2 which is adapted from the original publication.

The major difference to the POLSTRACC measurements is the altitude and potential temperature range, as the POLSTRACC flights did not exceed 411 K, whereas the focus during SOLVEO/THESEO was more on the free stratosphere. In this thesis the extension to the lowermost stratosphere and UTLS region is presented which is, due to the vortex deformation, more challenging than the free stratospheric analysis. The structure of the vortex will be discussed in detail in Sec. 4.3.

The analysis shown here benefits from the high resolution of measurements of N_2O and potential temperature in contrast to reanalysis PV fields sampled along the flight track. Thus, small-scale patterns at a size of several kilometres or filamentary structures can be assigned correctly and do not depend on the resolution of the model. Figure 4.3 aggregates all N_2O data points from the POLSTRACC campaign versus potential temperature (θ). (The data for the single flights can be found in Fig. 4.4.) The plot shows data for potential temperatures above 320 K to focus on the stratosphere above the ExTL at high latitudes. The observed $N_2O{:}\theta$ profile narrows towards the tropopause, whereas it widens towards higher altitudes and thus potential temperatures, showcasing the wide variety of air masses sampled during the flights. The labels in the upper part of Fig. 4.3 roughly indicate the region of the sampled air masses. Generally three regimes can be distinguished: the vortex regime is found at the inclined left edge of the profile characterised by a strong vertical gradient of N_2O mixing ratio, which connects the tropospheric source region to the photochemical sink in the middle stratosphere (Schmeltekopf et al., 1977). The gradient is maintained by the stratification and isolation of the polar vortex, while isentropic homogeneity leads to a compact form of the profile. At the other extreme, air from mid latitudes exhibits a more variable gradient in N_2O due to altering influence from tropical or polar air. The lower N_2O mixing ratios inside the vortex, on constant isentropes, result from the large-scale descent of N_2O-poor air from higher altitudes. Both regimes merge towards the troposphere, where the vortex transport barrier vanishes. In between at higher altitudes, the boundary region with a continuous transition of the mixing state between vortex and mid latitude contributions is visible.

A flight on 26 February 2016 (flight 14) provides a reference profile, reaching well into the upper vortex and capturing dynamically unperturbed vortex conditions. The flight exhibits a very compact relationship between N_2O and θ for a wide range of potential temperatures at the lower left edge of the data set in Fig. 4.3 (blue points). N_2O measurements from this flight are binned in 5 K intervals of θ, and the mean values are taken as the vortex reference profile (triangles in Fig. 4.3). Observations also include outside-vortex air as indicated by the light blue points between 345 K and 360 K, so the vortex reference points in this range are determined by a quadratic interpolation between the adjoining sections. Beyond 395 K, the vortex reference profile is set by linear extrapolation. A symmetric envelope is placed around the vortex reference profile. The width is determined for each flight individually by the maximum deviation of N_2O data points below the vortex reference value in each bin. All data points lying within the envelope are then considered to belong to vortex air masses (dark points in Fig. 4.3). This procedure is chosen to sensibly include a high number of measurements in the vortex regime, accounting for instrumental noise and small atmospheric variability while the criterion is not weakened too much. Hereafter, the term "vortex air" is meant to refer to measurements that fulfil the vortex criterion above 320 K. Equally, the term "extra-vortex air" is the complimentary set of measurements above 320 K.
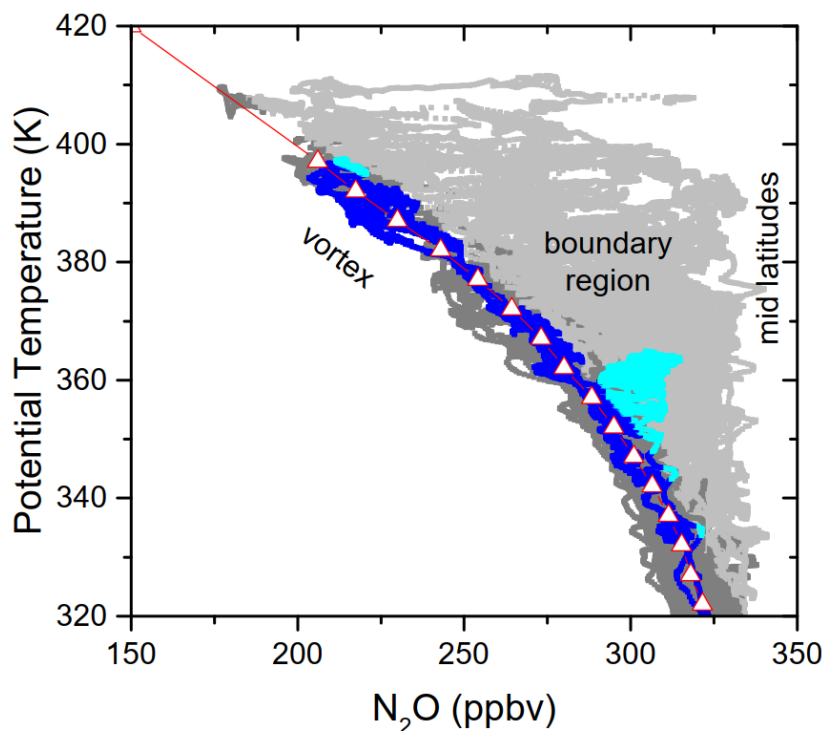
Figure 4.3.: Profiles of N_2O versus potential temperature for the whole POLSTRACC campaign (grey) and for the selected Flight 14, of 26 February 2016 (blue), above 320 K. The derived vortex reference profile is illustrated by the triangles, connected by straight red lines. Dark and light subsets of the grey and blue points indicate the assigned vortex air and extra-vortex air property, respectively.

Although the determined vortex reference correlation seems to be appropriate for the whole data set at first glance, one has to account for diabatic descent during the three month campaign phase. Satellite data of N_2O (Manney and Lawrence, 2016) and analysis of the in situ N_2O data (Krause et al., 2018) indicate that below $\theta = 450$ K, diabatic descent, i.e. descent of air masses versus isentropic surfaces, was strongest before the end of December 2015. Accordingly, the vortex reference correlation obtained from Flight 14 was lifted by 15 K only for the two December flights, while left unchanged for the rest of the flights.

The vortex reference correlation as shown in Fig. 4.3 coincides with the stratospheric profile from in Greenblatt et al. (2002) (Fig. 4.2 in the present work) very accurately, showing that this characteristic was maintained (within the range of uncertainty) over the decades. In contrast, below $\theta = 350$ K with more tropospheric influence, the 2016 values are enhanced over the year 2000 profile, in line with the increase in global tropospheric monthly mean N_2O burden of 13.7 ppbv within this period (NOAA-ESRL, 2020).
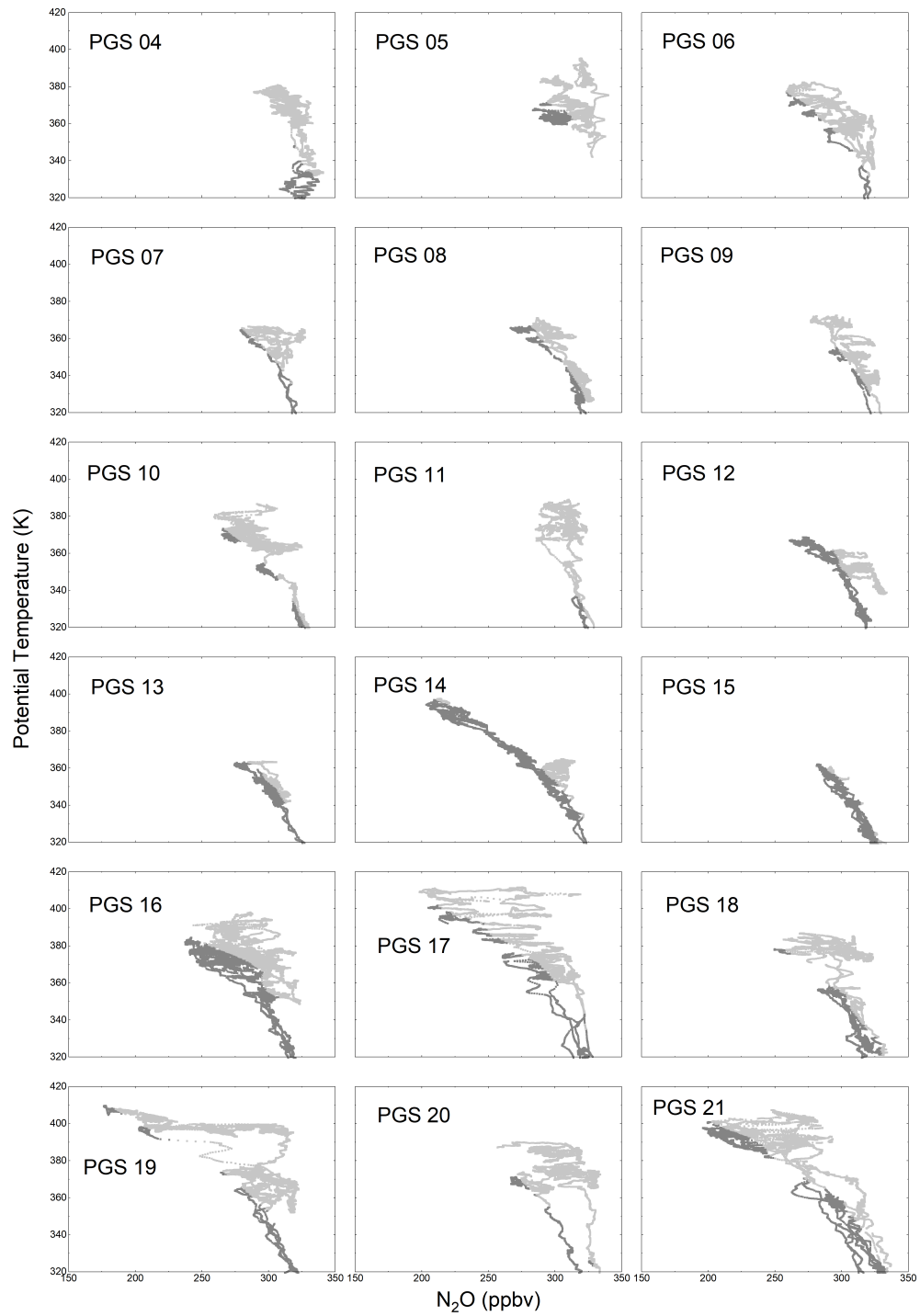
Figure 4.4.: Similar to Fig. 4.3, for all the single POLSTRACC (PGS) flights. The scales and color scheme are the same as in Fig. 4.3.

4.2.2. Identification of vortex air in the model

For CLaMS model data interpolated along the flight tracks, the measured N$_2$O:θ vortex criterion from Sec. 4.2.1 is applied in an equal manner, in order to achieve an optimal comparison to the measurement data. For vortex-wide averages, all model data with equivalent latitude Φ_e greater than 65° N are included. This choice results in a constant area (in square kilometres) and does not reflect the variability of the Nash criterion (Grooß and Müller, 2007), but – from experience – matches it quite well for a fully developed polar vortex, whereas the vortex area is overestimated during very early and late stages.

4.3. Chlorine partitioning throughout the Arctic winter 2015/2016

4.3.1. Overview of vortex air sampling

The flights of the POLSTRACC campaign were conducted from 17 December 2015 until 18 March 2016, covering several stages of evolution of the Arctic polar vortex. The map in Fig. 4.5 depicts vortex air sampling sections of the conducted flights in blue, as opposed to extra-vortex air sections in black. Two different patterns can be clearly distinguished: On the one hand, there are flights with long sections entirely inside the vortex, resulting in a good sampling statistics and providing insight to intra-vortex variability. On the other hand, many flights exhibit only a patchy sampling of vortex air whenever other objectives of the POLSTRACC campaign were pursued. As an example, the PV maps in Fig. 4.6 illustrate that a compact vortex signature is visible at 50 hPa (above 20 km altitude), whereas it becomes more spread-out and filamented below. On that particular day, vortex air measurements could be conducted over Greenland and northern Canada near the PV maximum on 150 hPa, which is the approximate flight altitude. Split-off parts of vortex air could also be found at latitudes down to 42.7° N towards the end of the campaign in early spring.

Vortex air sampling above a potential temperature of $\theta = 320$ K accumulated to a total of 2041 min or 34 h over the whole POLSTRACC campaign, enabling a generally good sampling statistics. Figure 4.7 gives an overview of the temporal sampling of vortex air above different potential temperatures. Therefore, the number of individual (HCl) measurements during each flight is summed up and depicted in columns. The colour code indicates the vortex air encounters divided in measurements above a certain potential temperature. Extensive vortex air sampling was performed primarily at the end of the first main phase and during the second main phase, in concert with the gradual descent of higher vortex air masses to flight altitude. Specifically, vortex air encounters represent between 3 % and 95 % of flight time
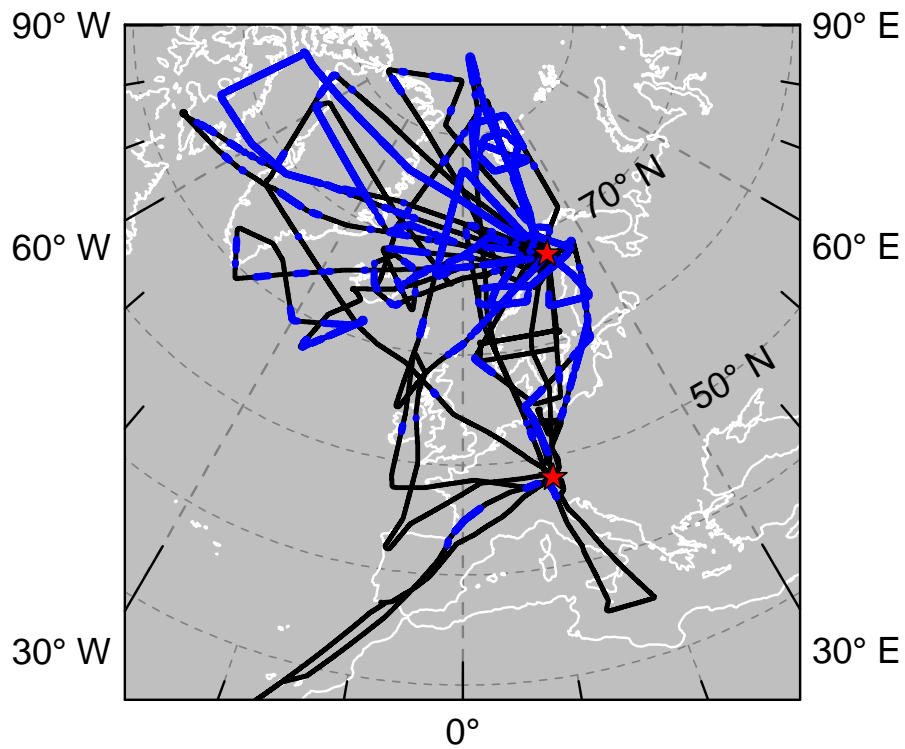
Figure 4.5.: Map of flight tracks of the POLSTRACC science flights. Red stars mark the two bases of operation Oberpfaffenhofen (EDMO) at 48° N, 11° E and Kiruna (ESNQ) at 68° N, 20° E. Flight sections where polar vortex air was encountered according to the criterion from Sec. 4.2.1 are indicated in blue.
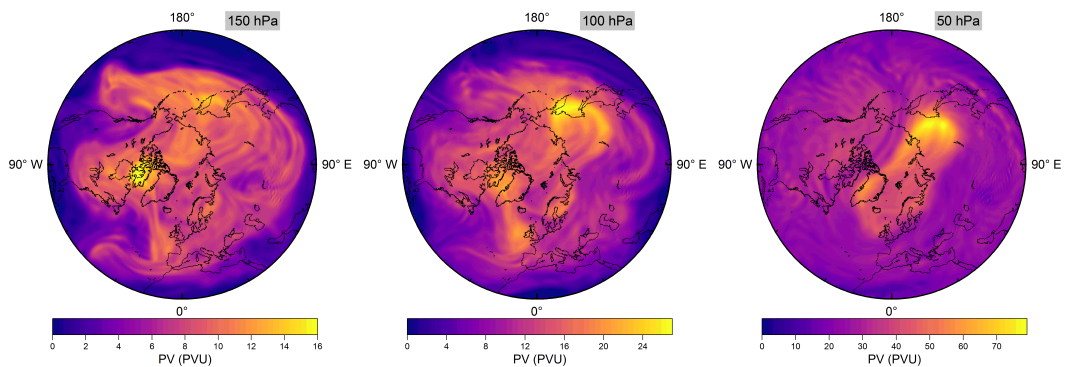

Figure 4.6.: Northern hemisphere potential vorticity (PV) maps from ECMWF reanalysis at 150, 100 and 50 hPa on 26 February 2016 at 12:00 UTC. Note the different colour scales in each panel.
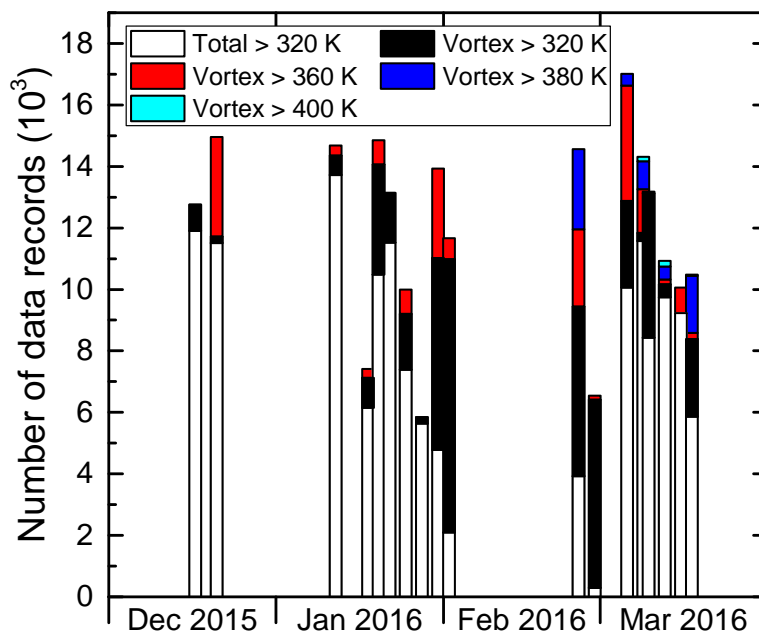
Figure 4.7.: Vortex air sampling statistics of the POLSTRACC campaign, counted by the number of individual HCl measurements. Each column represents a single science flight. Coloured bars indicate portions above selected isentropes.

of individual flights. In situ sampling was focused on $\theta > 340\,\text{K}$ for most flights, keeping significant distance to the tropopause. Vortex air above $\theta = 380\,\text{K}$ was only sampled as of 26 February 2016 when mainly adiabatic transport brought air masses with such high potential temperatures within reach of the HALO aircraft. The 400 K isentrope was only crossed during three occasions in March with a total time of about 10 min inside vortex air.

4.3.2. Measured evolution of inorganic chlorine during the winter

The evolution of inorganic chlorine partitioning in the lowermost Arctic polar vortex over a period of three months is assessed by means of daily statistics, which is performed by calculating averages, standard deviation and quantiles from all "vortex air" data points during individual research flights, in order to get a reasonable statistical sample size. This allows the study of changes in trace gas concentrations on a time scale of days. Beforehand, the data are binned into four layers of potential temperature, each spanning 20 K, to introduce a
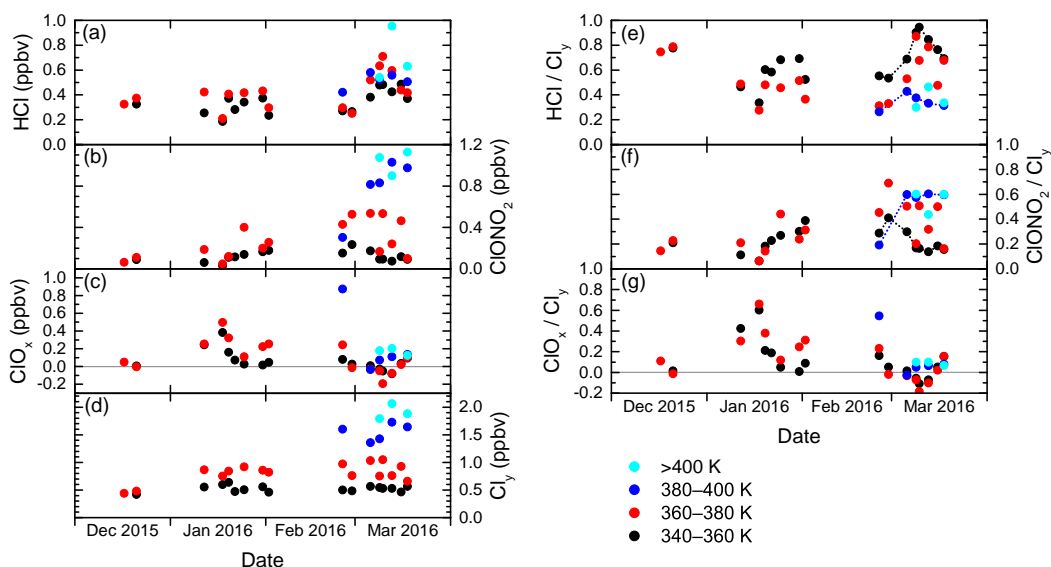
Figure 4.8.: Daily averages of measured mixing ratios of HCl, ClONO$_2$, ClO$_x$ and Cl$_y$ throughout the winter 2015/2016, from data that has been labeled "intra-vortex". Left (a–d): Absolute mixing ratios. Colours are the same as in Fig. 4.7. Right (e–g): Similar to the left panels, but for relative contributions of HCl, ClONO$_2$ and ClO$_x$ to Cl$_y$. Some of the black and blue points are connected by dashed lines to guide the eye along the different deactivation pathways.

coarse quasi-vertical coordinate. The panels a–d in Fig. 4.8 display the mean of the measured distributions for the individual HALO flights. Colours indicate the θ layers. The layer 320–340 K is omitted for clarity as it shows almost no difference to the 340–360 K layer. The panels e–g are similar to panels a–c, but display the relative abundance with respect to Cl$_y$ instead of absolute mixing ratios.

In December 2015, the measurements indicate that inorganic chlorine is partitioned almost entirely into the reservoir species HCl and ClONO$_2$ below the 380 K isentropic surface. This could already be observed in the instrument comparison in Fig. 3.11. With almost 80 % contribution to Cl$_y$, the photochemically stable HCl is predominant, whereas ClONO$_2$ ranges with less than 0.12 ppbv below or near the detection limit. This ratio is common in unperturbed conditions (e.g. Santee et al., 2008). At this early stage of the polar vortex, no ClO$_x$ has been detected.

The partitioning changes in January 2016, when the vortex is fully developed and temperatures are low enough to enable heterogeneous chemistry. The chlorine activation manifests itself in several ways in the observations: The absolute HCl mixing ratio does not show a

general trend through early February below 380 K, but in terms of relative partitioning, HCl makes up a smaller fraction of the total Cl_y with respect to December conditions. In addition, HCl exhibits intermediate minima at the length of days with a decrease by up to 0.21 ppbv, as well as a final minimum on 2 February, that may indicate episodes of enhanced chlorine activation. The lowest HCl mixing ratio measured above 360 K is 0.17 ppbv on 20 January. Correspondingly, at least two phases of enhanced active chlorine can be identified, in mid and late January/early February. On 18 January, measurements suggest that up to 75 % or 0.58 ppbv of Cl_y are activated below 380 K. These observations correspond with periods of high occurrence of ice and NAT PSCs (Voigt et al., 2018) which provide surfaces for heterogeneous chlorine activation. Enhanced mixing ratios of $ClONO_2$ up to 0.52 ppbv show how chlorine is repartitioned once sufficient amounts of ClO have been produced. The apparent rise in mean total Cl_y mixing ratio between December and January at 360–380 K from 0.44 to about 0.85 ppbv reflects the diabatic cooling that brings higher-level air masses to lower potential temperatures.

Large parts of the lower stratosphere could be sampled during the second main phase of the HALO deployment in late February and March, which covers the late stages of vortex evolution including the major final warming (MFW). The measurements show significant chlorine activation at the beginning of the second campaign phase when HALO could sample for the first time air masses above 380 K potential temperature, where a peak amount of 1.15 ppbv ClO_x at the flight altitude of 13 km was found. The MFW on 5 March (Manney and Lawrence, 2016) observably terminated heterogeneous chlorine activation reactions, with remaining ClO_x amounts no greater than 0.20 ppbv. The build-up of the reservoir species from deactivated compounds (sometimes referred to as "recovery") varies strongly across the specified isentropic layers (supported by dashed lines in 4.8e–f): below 360 K, a gradual increase in HCl up to 0.58 ppbv throughout March can be seen, whereas $ClONO_2$ soon returns to concentrations below the detection limit. The stratospheric warming made higher θ-levels accessible to HALO, and above 380 K, recovery pathways are different: depleted HCl starts to recover, but this positive trend is halted and eventually reversed by early to mid March. Meanwhile $ClONO_2$ increases strongly above the level of HCl mixing ratios. Between 360–380 K (red data), observations are not very clear about the overall evolution, especially of $ClONO_2$. Also, negative values for ClO_x are calculated. While these are still within the uncertainty limits, this isentropic layer seems to contain a strong vertical variability of chemical constituents involved in chlorine repartitioning, communicating the different behaviour below and above. The vertical sampling of HALO may introduce a bias, which is also obvious in the enhanced variability of mean Cl_y values in the layers above 360 K. This is investigated further by the model intercomparison below.

Figure 4.9 illustrates the concept of differential deactivation pathways in this late winter period in a different manner. There, the partitioning of Cl_y is shown in a ternary diagram of
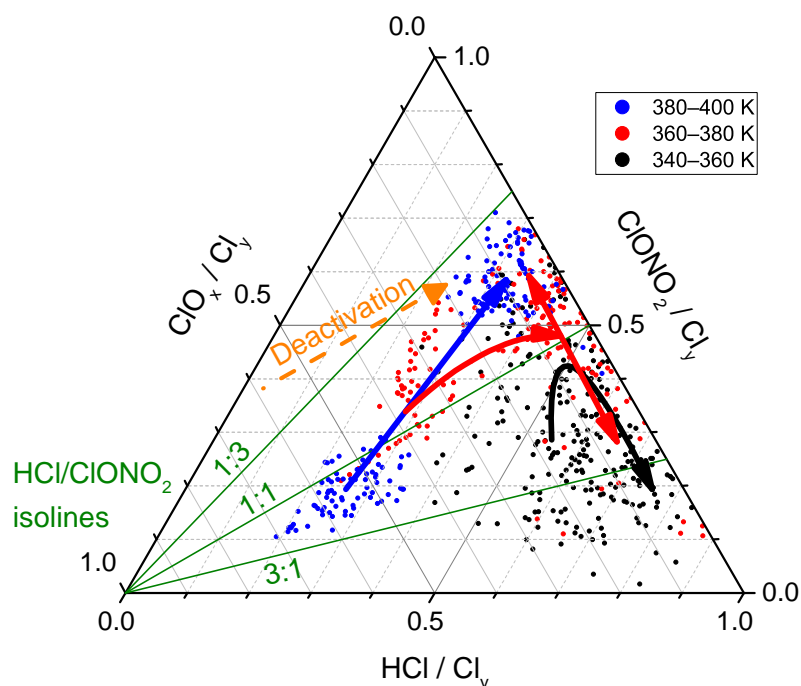
Figure 4.9.: Ternary diagram of the partitioning of Cl_y into HCl, $ClONO_2$ and ClO_x during the second main campaign phase, from 26 February to 18 March 2016. The HCl isolines run from bottom left to top right, the $ClONO_2$ isolines horizontally, and the ClO_x isolines from top left to bottom right. Dots mark individual measurements, where colours indicate the isentropic layers. Solid arrows illustrate the temporal evolution of the daily averages. As an aid to the reader, three green lines denote characteristic values of the HCl/$ClONO_2$ ratio, and the orange dashed arrow points towards decreasing values of the ClO_x fraction.

HCl, $ClONO_2$ and ClO_x fractions. The dots mark individual measurements, the same that the daily averages in Fig. 4.8e–g were based on. The solid arrows run along the temporal evolution of the daily averaged measurements and show the two pathways below 360 K (black) and above 380 K (blue), diverging towards HCl or $ClONO_2$, as well as the 360–380 K isentropic layer (red) sandwiched in between. Using the supporting green isolines of the HCl/$ClONO_2$ fraction, it is observed that below 360 K, the partitioning between the reservoir species is more HCl-heavy and after recovery, HCl is three times more abundant than $ClONO_2$. Above 380 K, in contrast, the reservoir species evolve from a nearly 1:1 partitioning to a state with twice as much $ClONO_2$ relative to HCl.

4.3.3. Comparison of measured and CLaMS-modelled data

Simulations by the Lagrangian chemical transport model CLaMS were provided by Jens-Uwe Grooß to put the observations into a broader context, and to investigate sampling biases potentially caused by the coverage of the aircraft observations. To assess the accuracy of the model, the model results were interpolated to the location and time of the observations employing the trajectory mapping described above. Figure 4.10 displays the model results (crosses) sampled alongside the original flight track with the same vortex criteria and averaging procedures. As for HCl, the model generally follows the trends of the measurement data. Before February, however, there is a clear high bias by 0.13–0.20 ppbv in almost all model HCl data which was not observed after the break in such a systematic manner. Having ruled out technical changes on the simulation and on the instrumental sides during this time, it seems as if a model bias can be observed that is known from satellite comparisons at higher altitudes in the dark polar vortices, a problem that is observed by other models as well (Grooß et al., 2018; Wohltmann et al., 2017). The intercomparison of model and in situ data supports the rationale that chemistry-climate models struggle in reproducing the observed chlorine partitioning in the dark winter months, where some unknown process for HCl removal is lacking. Grooß et al. (2018) investigated the response of modelled HCl to a number of hypothetical processes, particularly involving PSCs through (hypothetical) HCl uptake or, a more favoured explanation, through the release of NO_x. Galactic cosmic rays may catalyse PSC decomposition, but observational evidence for any of these processes is still lacking. Nevertheless, the present study extends the previous comparisons by Grooß et al. (ibid.) to lower altitudes. Consistently, the discrepancy is absent as soon as sufficient sunlight returns towards the end of the winter. An overestimation of HCl is partly reflected in an overestimation of Cl_y and underestimated $ClONO_2$ and ClO_x concentrations.

$ClONO_2$ is better represented in the model below $\theta = 360$ K, whereas there are indications of a slight underestimation at higher potential temperatures. This may be induced in part by the HCl high bias until midwinter, or by generally underestimated Cl_y mixing ratios recognizable above 380 K. The model is able to produce the observed change in recovery across the different isentropes. The modelled vertical shift from HCl to $ClONO_2$ as the dominant reservoir species during repartitioning in March between 360–400 K is obviously subject to a sampling bias just like the measurements, but at the same time does not always follow the observational data. This deviation is probably caused by a lack of vertical resolution in the meteorological data fields that prevents the model from estimating the high vertical gradients in the atmosphere in all detail.

Beyond this direct intercomparison, model data can help explore to what extent the observations along the aircraft's flight track are representative of the entire polar vortex. Therefore,
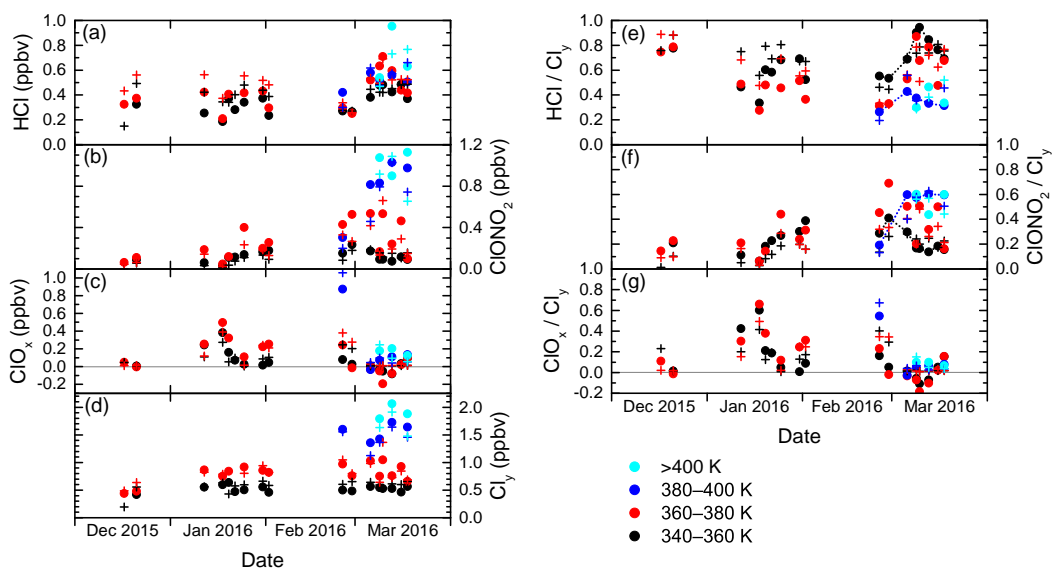
Figure 4.10.: Similar to Fig. 4.8. In addition to averages from the measurements depicted as points, crosses denote averages from CLaMS model data interpolated at the flight track.
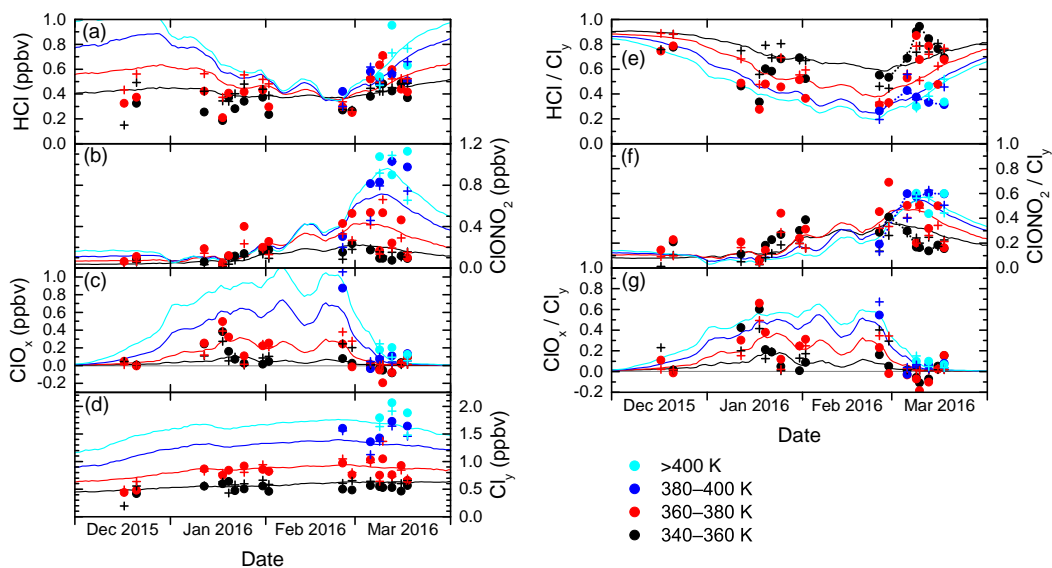
Figure 4.11.: Similar to Figs. 4.8 and 4.10. In addition, lines represent whole vortex model averages.

the lines in Fig. 4.11 display the modelled concentration of the chlorine species in a vortex-wide average at the different isentropic levels. In general the local aircraft observations reflect the mean chlorine partitioning in the vortex LMS quite well. The periods when activated chlorine can be found are consistent, whilst enhanced local variation of ClO_x in January is not projected into the vortex averages. Vortex-averaged HCl mixing ratios clearly suffer from the deviation during the dark episode. Apart from that, no systematic biases between vortex-averaged and local model data as well as in situ data are observed. Toward the end of the winter, the vortex averages include air masses from lower latitudes at increased frequency. This is accompanied, for example, by a sudden drop in modelled mean ozone (not shown), which would explain the lower values of all chlorine species, compared to the measurements in the local remainders of vortex air.

4.3.4. Variability of chlorine partitioning

To assess the validity of using daily averaged mixing ratios as in the previous sections, Fig. 4.12 displays in addition to mean values the extrema and quartiles from the statistics studied hitherto. The 360–380 K layer is taken as an example that stretches over all measurement phases. The same visualisation for the other potential temperature layers can be found in Figs. 4.13 to 4.15. Intermediate data spread, as seen in most January flights, reflects the small and steady variation through the depth of the layer, while trends between consecutive flights are clearly visible. There, the statistics are based on a solid sample size, and these are the periods where measurements and model data match best. A very low variability, such as for the first December flight or for two flights on 10 and 13 March stems from very few vortex sampling points in this layer, rendering these values less representative. Consistently, the model data interpolated along the flight track deviates strongest from the measurements on these dates, as visible in the HCl and $ClONO_2$ results. This is simply due to selection of data which is compared: Outside vortex data are consistent between the various measurements and in good agreement with the model. Very high variability, as seen on 26 February and 6 March hints at enhanced differential processing or transport within the sampled air masses.

The standard deviation of the vortex-averaged statistics (grey shading in Figs. 4.12 to 4.15) reflects the intra-vortex atmospheric variability. Without accounting for potential systematic biases, two thirds or 67 % of the observational data are found within this spread, which demonstrates the joint performance of the measurements and the model at reproducing vortex air characteristics on single aircraft flight tracks.
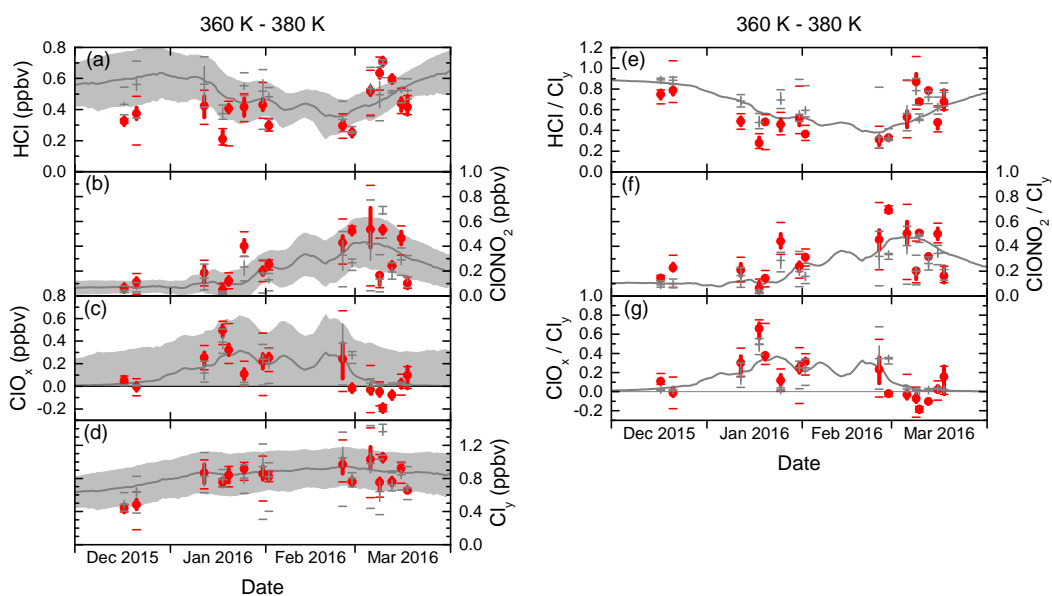
Figure 4.12.: Similar to Fig. 4.11, with more detailed statistics of only the 360–380 K layer. Measurements are red, model data are grey. Beyond the mean values (points and crosses), vertical bars span the second and third quartiles, while horizontal bars indicate minimum and maximum values. The grey area encompasses the standard deviation from the vortex averaging (only for panels a–d).
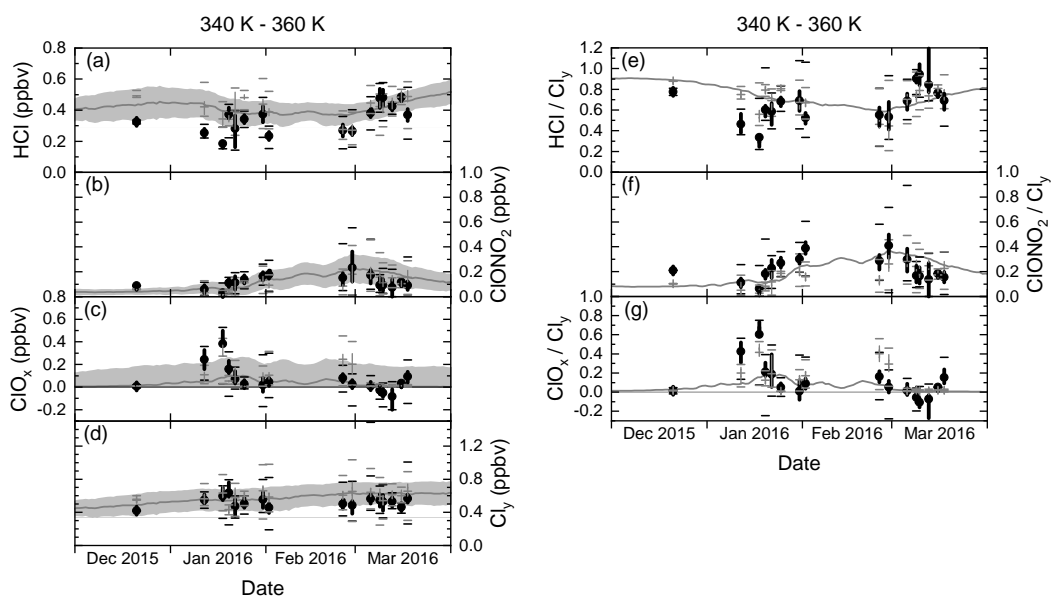
Figure 4.13.: Similar to Fig. 4.12 for the 340–360 K layer.
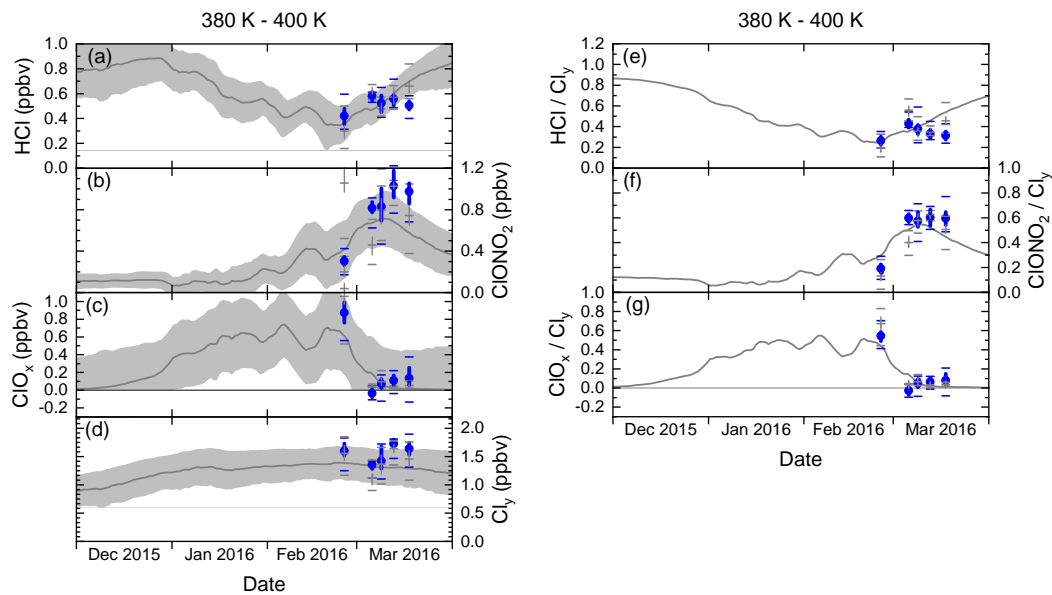
Figure 4.14.: Similar to Fig. 4.12 for the 380–400 K layer.
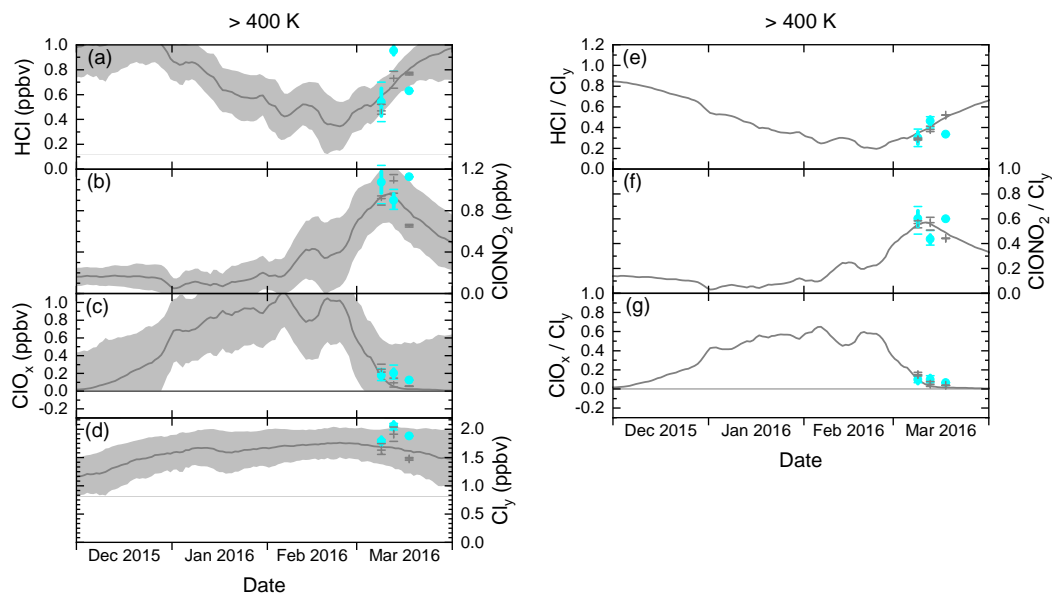
Figure 4.15.: Similar to Fig. 4.12 for the layer above 400 K.

4.4. Case study: peak active chlorine

This section presents a case study of one particular POLSTRACC flight, where the highest concentration of active chlorine was encountered. As will be discussed later, temperatures at the location of the in situ measurements were too high to enable PSC-catalysed activation, which must have occurred beforehand. The case study explores the observations and according modelled chlorine chemistry and probable trajectories that connect the origin and fate of the highly chlorine-activated air masses.

4.4.1. Synoptic situation and flight strategy

The measurements of Flight 14 which took place on 26 February 2016 are examined. This was the first opportunity for a scientific flight within the second major campaign phase, after a break of three weeks in February. The aims of this flight were essentially twofold: First, the stratospheric cold pool should be probed from its lower edge, including the observation of PSCs above flight altitude with the zenith-pointing lidar WALES (Groß et al., 2014; Voigt et al., 2018; Wirth et al., 2009). Second, an area of strongly subsided air masses west of Greenland should be sampled by the in situ instrumentation, where chemistry forecasts by the CLaMS model predicted – inter alia – high amounts of activated halogens (ClO and BrO). Figure 4.16 shows the actual flight track (light blue), which was flown in counter-clockwise direction. Starting out of ESNQ at around local noon, it comprised an extended section towards the north-west, with PSCs above the aircraft over the whole Atlantic overpass. After the Greenland crossing, the subsided air masses were encountered. The highest values in temperature, potential temperature (Fig. 4.17) and ozone (not shown) were found at the end of the southbound leg above Baffin Island, before heading east again. These observations are consistent with the temperature field at 150 hPa from ERA-Interim reanalysis by the European Centre for Medium-Range Weather Forecasts (ECMWF), which shows a temperature maximum over the Hudson Bay (Fig. 4.16).

The temperature map, however, does not give further evidence of the location and extent of the polar vortex. As stated in Sec. 4.2.1 and shown in Fig. 4.3 and Fig. 4.5, most sections of the flight were indexed as intra-vortex, with a major interruption only on the return leg between about 18:00 and 20:30 UTC. A clearer view on the vortex structure was given in Fig. 4.6, where PV from ERA-Interim reanalysis is displayed at three different pressure altitudes. The lowest altitude of 150 hPa approximates an average flight altitude. Usually, PV is analysed along isentropes. However, as θ varies strongly along the flight path, a pressure-based mapping seems more intuitive for a flight-focused consideration. A clear maximum in PV at 150 hPa is collocated with the temperature maximum in Fig. 4.16. Apart from that, a compact vortex structure cannot be found at flight altitude. Rather, the PV field exhibits larger patches
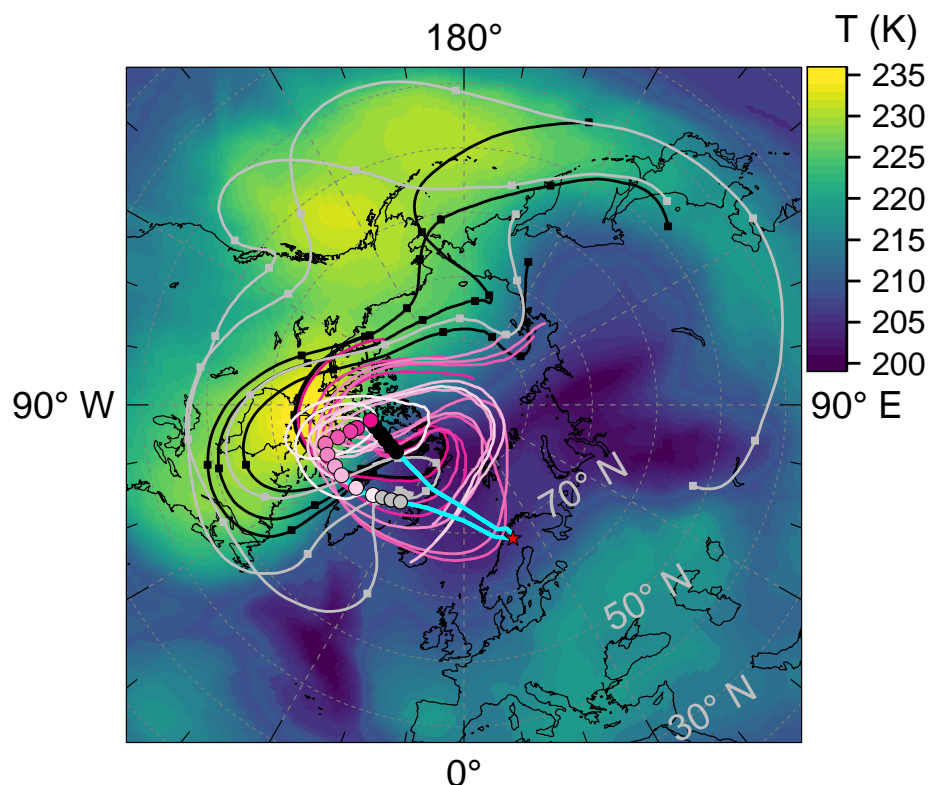
Figure 4.16.: North pole centred map containing several aspects of the case study in Sec. 4.4. The flight track of POLSTRACC Flight 14 on 26 February 2016 is shown in light blue. The red star marks the campaign base in Kiruna (ESNQ). Coloured dots along the flight track indicate the anchor points of calculated backward and forward trajectories. The horizontal tracks of the 10 day backward trajectories are shown in the same colours as their respective anchor points. Dots along the black and grey trajectories illustrate 24 h intervals. The shading indicates the ECMWF temperature field on 26 February 2016 at 12:00 UTC on the 150 hPa isobar, approximately the time and altitude of the flight.

as well as extended areas of filamentary structure. At 100 hPa, the PV distribution looks only slightly less frayed. A compact structure is clearly observed at 50 hPa. Thus the vortex is well constrained at 50 hPa, whereas the transport barrier is significantly weaker at lower altitudes, allowing for large scale advection and potentially mixing with air from the surf zone and mid latitudes. Still, patches and filaments with locally enhanced PV and θ-N_2O ensembles give indications of vortex outflow or air masses that inherit a local maximum contribution by the vortex compared with their surroundings. In particular, the T- and PV-maximum at 150 hPa

indicates an area of adiabatic descent of highly vortex-influenced air.

4.4.2. In situ measurements on 14 February 2016

Parts of Fig. 4.17, which displays the measured trace gas concentrations, have been published in Oelhaf et al. (2019), giving a short insight into observations of active chlorine during the campaign.

Figure 4.17a displays altitude and longitude for orientation. In Fig. 4.17b the evolution of temperature (T) and potential temperature (θ) during the flight is shown. After the initial climb, T stays very constant at 204 ± 1 K for 2.5 h. Only then, past 14:00 UTC, T rises almost monotonically, continuing also after the southward turn at 75° N, 80° W. Between 15:30 and 16:00 UTC there are fluctuations by up to 4 K. The temperature maximum of 233 K is reached just before the southern turning point at 16:18 UTC. Thereafter T declines again almost monotonically, until 203 K are indeed recaptured.
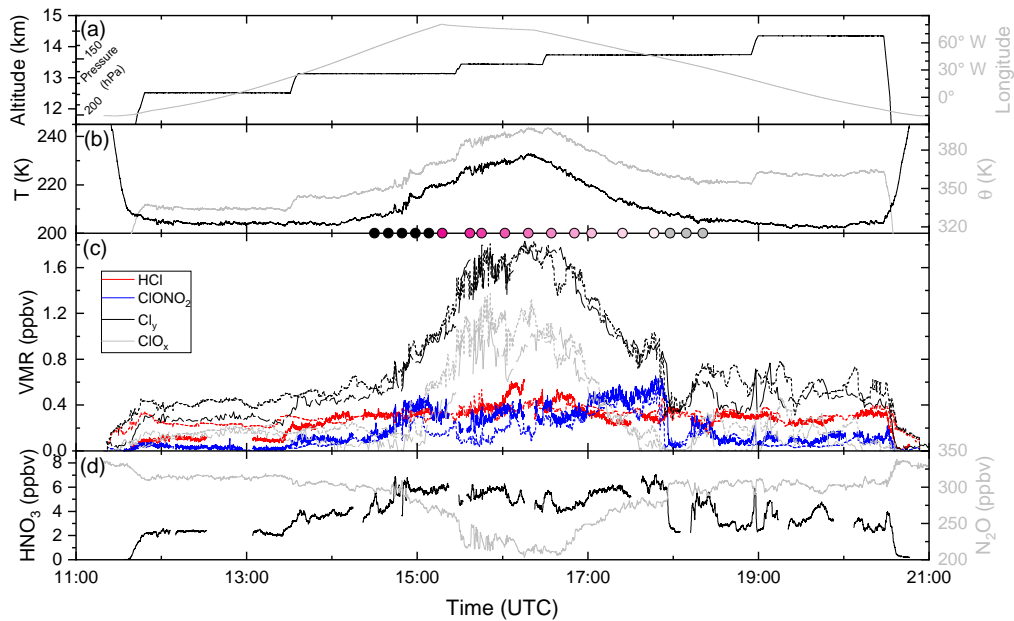
Figure 4.17.: Time series of measurements during Flight 14 on 26 February 2016. (a) Altitude, pressure and longitude for orientation, (b) temperature (T) and potential temperature (θ), (c) chlorine species, (d) nitric acid (HNO$_3$) and nitrous oxide (N$_2$O). Solid lines indicate measurements and dashed lines denote CLaMS simulations interpolated along the flight track. The inset shows the time period from 15:34 UTC to 16:06 UTC in more detail. The black, magenta and grey dots between panels (b) and (c) mark the points in time where trajectory calculations were started, cf. also Figs. 4.16 and 4.18.

4. Chlorine partitioning in the Arctic lowermost stratosphere

Accordingly, θ varies substantially along the flight track, ranging from 332 K to 397 K, while the pressure altitude changes only in small steps. The encountered high baroclinicity thus enabled a flight deep into the polar vortex outflow. The transitions between regions of low and high T (or θ) should probably be seen more as vertical sampling of the lowermost stratosphere (LMS) in terms of θ as a vertical coordinate, rather than horizontal sampling along (equivalent) latitudes or longitudes.

Figure 4.17c displays in solid lines the temporal evolution of the inorganic chlorine tracers from measurements of AIMS and GhOST. On the first and lowest flight leg with θ below 340 K, $ClONO_2$ is completely absent. At the same time, total inorganic chlorine Cl_y more than doubles the amount of HCl and thus active chlorine ClO_x contributes more than 50 % to the Cl_y budget. The nearly complete consumption of $ClONO_2$ indicates an ongoing or very recent chlorine activation event in the presence of PSCs or by photolysis of $ClONO_2$ at the return of sunlight. Indeed, the onboard lidar measurements indicated PSC occurrence at 1–7 km above flight level on that day. Unfortunately, lidar data from the Cloud-Aerosol Lidar and Infrared Pathfinder Satellite Observation (CALIPSO) satellite are not available for the February 2016 period.

ClO_x is almost completely absent in the air masses probed between 14:00 and 15:00 UTC. Meanwhile, an increase of Cl_y and θ along the flight track is observed, mainly composed of $ClONO_2$, while the HCl mixing ratio remains almost constant at about 0.32 ppbv. In the region sampled after 14:44 UTC, $ClONO_2$ provides the most abundant contribution to the Cl_y budget. An even stronger inversion of the HCl/$ClONO_2$ ratio is again observed between 17:00 UTC and 18:00 UTC. In both cases, at about $355\,\text{K} \leq \theta \leq 380\,\text{K}$, the enhanced values of $ClONO_2$ are indicative of a repartitioning of Cl from HCl through prior or ongoing activation and subsequent deactivation in the presence of HNO_3, enhanced by nitrification from PSC particles, which have been subject to sedimentation and sublimation (Manney and Lawrence, 2016; Voigt et al., 2018). This is corroborated by the occurrence of maximum HNO_3 mixing ratios up to 7 ppbv (Fig. 4.17d) in these particular flight sections. Note that HNO_3 is not directly involved in $ClONO_2$ formation. Rather it can be source of the required NO_2 through photolysis or a reaction with OH, an therefore serves as an indicator for NO_x abundance in the upper troposphere and stratosphere.

Between 15:30 UTC and 16:45 UTC, when T and θ reach their maximum values, Cl_y naturally approaches its highest levels as the aircraft performs the deepest intrusion into the stratosphere. N_2O assumes its minimum here. Meanwhile, HCl and $ClONO_2$ mixing ratios do not increase as much. HCl is the slightly more prevalent reservoir species for the most part. Altogether, these observations imply a high amount of ClO_x in terms of mixing ratio in this air mass at $\theta > 380\,\text{K}$. In fact, these are the maximum ClO_x concentrations found along all of the flight paths of the whole campaign, reaching up to 1.15 ppbv. Compara-

ble values have been reported from satellite observations at $\theta = 460\,K$ as an average in the 2005/2006 Artic vortex' core (Santee et al., 2008), whereas the ClO_x concentration was expected to drop by at least one third down to $\theta = 380\,K$. The values during the HALO flight are therefore unusually high. Until about 16:00 UTC, also a high fluctuation of ClO_x values is observed that span down to 0.61 ppbv, equivalent to a decrease by 47 % from the maximum value. In the calculation of ClO_x, these fluctuations are apparently introduced by the respective Cl_y fluctuations. In the meantime, HCl remains relatively smooth, while the fluctuations can be confirmed in the $ClONO_2$ signal. Caution should be exercised when addressing the frequency of fluctuations: from the $ClONO_2$, a typical along-track period of 30 s to 3 min can be estimated, equivalent to a typical horizontal length scale of 6 km to 36 km. Therefore, Cl_y data points and ClO_x values, correspondingly, resolve the fluctuation pattern only very poorly. Overall, the observed fluctuations likely result from a high dynamical variability in the probed air masses with differentially descended patches on a horizontal scale of tens of kilometres. That the fluctuations are seen in the $ClONO_2$ signal, but not in HCl, points to a separation of time scales in the recovery of chlorine into the reservoir species. The recovery into $ClONO_2$ is fast enough to produce the observed pattern, whereas HCl recovery proceeds much slower, such that the time scale of effective diffusion due to mixing between adjacent patches equals or is greater than the typical time scale of HCl recovery, smoothing the HCl distribution.

After 17:50 UTC till the end of the flight the aircraft crossed the vortex edge several times. These transitions are clearly visible in the high gradients in chlorine species and HNO_3. The independent marker N_2O also rises significantly (while θ evolves smoother) when leaving the vortex. This feature was also visible in the θ-N_2O profiles in Sec. 4.2.

4.4.3. Parallel model and remote sensing observations

The measured chlorine concentrations are juxtaposed with values calculated from the CLaMS model, interpolated along the flight track. Model data is shown as dashed lines in Fig. 4.17c. For the features of the latest version of CLaMS, see Grooß et al. (2018) and references therein. Overall, the model reproduces the observed chlorine activation surprisingly well. In the subsided air masses, mean ClO_x is similar in observations and the model. Only until 16:00 UTC, there are two strong deviations, that may be attributed to the limited spatial resolution of the model in the filamentary parts of the vortex outflow. More systematic deviations are found in the first and last thirds of the flight, especially at $\theta < 350\,K$ in HCl and Cl_y (and therefore also in ClO_x).

In these sections at low potential temperatures, Cl_y is overestimated in the model, which is at least in part induced by overestimated HCl. While chemical processes are expected to be well captured, possible causes may be unresolved small scale exchange processes in the

UTLS and improper tropospheric boundary conditions that echo into the LMS. On the other hand, the Cl_y estimated from CFC-12 measurements also exhibits the largest uncertainty at the low potential temperatures.

The in situ observations during the POLSTRACC campaign have been accompanied by limb infrared absorption spectra obtained with the GLORIA instrument aboard HALO. Johansson et al. (2018) describe the validation and comparison of some measured chemical species with in situ and satellite observations. Among these, $ClONO_2$ is the sole chlorine compound. Using these observations, Johansson et al. (2019) study the spatial distribution and partitioning of inorganic chlorine, inter alia for the flight on 26 February, with a stronger focus on model validation. From the 2D curtains of mixing ratio below flight altitude, a band of enhanced $ClONO_2$ about 1–2 km below the aircraft inside the subsided air masses was observed. While GLORIA reports less than 0.4 ppbv at flight altitude, the mixing ratio reaches 0.6–0.7 ppbv in this band. Meanwhile in similar curtain plots, measurements of enhanced HNO_3 and CFC-12 readily indicate the region of overall downward transport. ClO measurements by GLORIA indicate that the $ClONO_2$ band represents the lower boundary to the occurrence of enhanced active chlorine from downward transport.

4.4.4. Trajectory calculations

The high ClO_x concentrations found for this flight bear the potential to catalytically destroy ozone in the LMS. In oder to get an idea of the reasons behind exceptionally high ClO_x, the history and fate of selected air masses sampled during flight 14 were analysed using trajectory calculations by the HYbrid Single-Particle Lagrangian Integrated Trajectory (HYSPLIT) dispersion model (Draxler and Hess, 1998), based on meteorological fields provided by ECMWF ERA-Interim reanalysis at $0.25° \times 0.25°$ horizontal resolution. The trajectories were initialised at selected points distributed along the flight track (in space and time), as shown in Fig. 4.16 (top down view) and Fig. 4.17 (time). The points cover the period of passage through the area of subsided air as well as the transition periods before and after the passage (termed "pre-entry" and "post-exit" in the following). From each point, a trajectory was calculated ten days backwards (into the past) and eight days forwards (into the future). These trajectories account for the motion of air parcels along a mean wind only, whereas mixing and dispersion are not resolved. In Figs. 4.16, 4.17 and 4.18, the anchor points and according trajectories are colour-coded consistently: pre-entry trajectories are black, post-exit trajectories are grey, and passage trajectories are shaded in decreasing saturations of pink. The distinction between the groups is made by virtue of a visual inspection of common features.

To begin with, the pre-entry and post-exit trajectories are examined. The backward-calculated paths (see map in Fig. 4.16) are comparable for both groups, as they likely belong to air
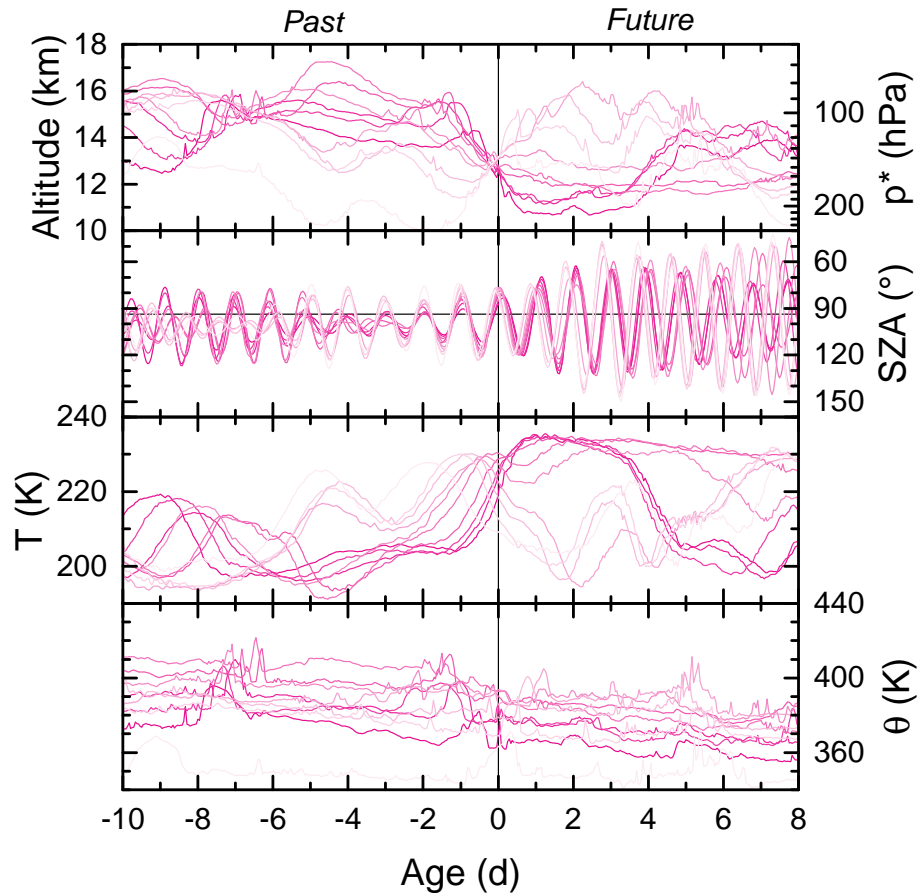
Figure 4.18.: Time series of altitude, solar zenith angle (SZA), temperature (T) and potential temperature (θ) of selected trajectories (see Sec. 4.4.4 and Figs. 4.16 and 4.17), calculated by the HYSPLIT model. As altitude and pressure representations are visually similar, p^* marks a proxy pressure axis. Backward and forward trajectories are seamlessly connected. Each individual trajectory starts at age "0" upon initialisation at the respective anchor point. The horizontal line at 93.66° in the SZA panel indicates the zenith angle of the horizon for an observer at 13 km altitude.

masses with similar history. The map shows – as a rough estimate – how the black and grey trajectories move halfway around the north pole within 10 days, equivalent to about 18°/d zonal velocity. In most cases, the black paths are found north of the grey paths, indicating a somewhat homogeneous motion. Only the "last" grey trajectory (anchor point as time reference) represents a certain outlier, as its adherence is different from the rest of the group. As of 3 days before the measurement, the black and grey trajectories take a more or less sharp left turn and travel in northbound direction, which is potentially induced by planetary

wave activity. The northbound motion halts 2 to 1 day(s) before encounter and eventually, the trajectories are slightly southbound again. Overall, this resembles a hard braking and may have led to a distortion of the vortex and narrowing of the vortex edge region.

In contrast, the coloured trajectories from the region of subsidence exhibit a very distinct shape. They show an almost coherent motion in a spiral-like manner, which is confined to the area north of 65° N. Within 10 days, the trajectories circle a (imaginary) centre approximately once. This centre seems to be located in northern Greenland for the very pink trajectories and near Baffin Island for the whitish ones. These trajectories neatly visualise the typical revolving motion of the polar vortex. This is also apparent from the time series of the solar zenith angle (SZA) in Fig. 4.18. There, the horizontal line indicates a simplistic separation of day and night sections. Coherent motion is seen in the equally coherent oscillations of the SZA, and the amplitudes are anticorrelated with latitude.

The altitude and approximate pressure of the pink trajectories is displayed in the upper panel of Fig. 4.18. There, a clear downwelling trend is observed within in the last 1–2 days, when the paths descend by 1–3 km. Beforehand, they remain within a range of about 2 km, with a mean altitude between 14 and 16 km. Thus, the descent prior to the flight represents a unique event in the younger history of the air masses. The downwelling event is not concurrent, but occurs with a shift of up to two days between the trajectories of the first (pink) and last (white) anchor point. A very similar picture is drawn by the evolution of temperature, where a rise by 20–25 K is apparent just before the flight time (within ≈ 2 days); in some cases, this "late" rise represents a continuation of a more prolonged effective positive temperature trend within the 10 days of backward trajectories. The T-variability resembles adiabatic up- and downwelling, because the potential temperature θ instead shows a much more steady and effectively negative trend between almost zero and 13 K over a period of 5 days, as evidence of diabatic descent.

A very important point in the backward trajectories is that the subsided air masses have likely experienced very low temperatures ($T < 200$ K) until 4 days before the measurement, at the latest. More precisely, all coloured backward trajectories reach at least down to $T = 196$ K, a value often given as the equilibrium temperature T_{NAT} for the existence of nitric acid-trihydrate (NAT) particles at typical stratospheric conditions (Hanson and Mauersberger, 1988). NAT particles in PSCs (Voigt et al., 2000a) can serve as the heterogeneous reaction partners for the formation of active chlorine. NAT particles have frequently been observed in the cold Arctic winter 2015/2016 (Voigt et al., 2018) when temperatures were continuously below T_{NAT} for 2 months (Dörnbrack et al., 2017). The observed high ClO_x values during the case study flight can therefore be explained by the presence of PSCs above 14 km altitude and 6 ± 2 days before the measurement, where $T \lesssim T_{\mathrm{NAT}}$. A similar conclusion was made by Johansson et al. (2019) based on backward trajectory calculations from the mentioned

$ClONO_2$ band below the flight path, involving CLaMS chemistry along the trajectories.

The high frequency fluctuations in θ at 8–6 and 2–0 days before encounter are similarly observed in the altitude graph, but not visible or much less pronounced in T. Examining the trajectory tracks, these fluctuations are assumend to be a model artefact in the presence of orography like Greenland or the islands of the Canadian Shield.

Forward trajectories provide a glimpse of the potential further behaviour of the probed air masses. While the "first" trajectories (in highly saturated pink) are the latest in the onset of downwelling, they descend even more beyond the encounter, resulting in a record increase of T by 30 K within 2 days. Similarly, the geometric descent is continued well down below 12 km. Thereafter, some days of stable conditions in altitude and T follow, before three of the pinkish trajectories experience a major upwelling and cooling again, effectively reversing the downward displacement during HALO flight 14. Other trajectories with later anchor points, however, either do not recover from the downwelling at all or they rise again very quickly within 1–2 days, whereupon the subsequent motion is governed by less coherent oscillatory modes. In summary, a range of three different future scenarios for the subsided air masses is identified: 1. several days of subsidence by up to 30 K or 4 km with complete recovery, 2. equal subsidence without observable recovery within a week, 3. quick recovery followed by a rather neutral trend. Further, the amplitude of the quasi-diurnal SZA oscillations tend to increase in all projections (Fig. 4.18), indicating a net southbound trend of the trajectories.

4.5. Discussion

In this section, the observed evolution of chlorine partitioning during the winter 2015/2016 is compared to previous studies using in situ and remote sensing data.

The Arctic polar vortex during winter 2015/2016 was studied by Manney and Lawrence (2016), using measurements from the Aura MLS instrument. As for chlorine species, they retrieved HCl and ClO at a vertical resolution of 2.5–6 km down to $\theta = 390$ K. Therefore, the satellite data only have a small overlap with this work's in situ observations in March. Nevertheless, the depletion and recovery of HCl and the occurrences of active chlorine as reported in Sec. 4.3.2 consistently extend the satellite observations to lower altitudes, showing that chlorine activation is not limited to the higher altitudes inside the Arctic polar vortex.

Based on measurements on the ER-2 aircraft within the SOLVE/THESEO mission, Wilmouth et al. (2006) drew a very comprehensive picture of inorganic chlorine partitioning in the Arctic polar vortex of 1999/2000, where low temperatures (Manney and Sabutis, 2000), high PSC occurrence and large chemical ozone loss (Rex et al., 2002) were observed. At isentropes around 440 K, ClO_x/Cl_y reached up to 90 % in January and HCl accounted for the

remaining 10 %, whereas ClONO$_2$ was not detectable. Thus, the higher degree of activation at higher potential temperatures, as compared to the POLSTRACC measurements, seems to come mainly at the expense of ClONO$_2$. From their late winter budget analysis, Wilmouth et al. (2006) suggest that HCl recovers at a rate similar to or higher than the ClONO$_2$ recovery rate. They state that the evolution of inorganic chlorine partitioning in the Arctic is rather variable. Whether the chlorine deactivation into ClONO$_2$ or HCl is favoured, depends critically on the mixing ratios of ozone and NO$_x$ (Grooß et al., 2005). The late winter aircraft measurements are in line with observations during a balloon sounding of the MIPAS-B (Michelson Interferometer for Passive Atmospheric Sounding) and TELIS (TErahertz and submillimeter LImb Sounder) in the late Arctic winter 2011 (Wetzel et al., 2015). There, HCl is the dominant reservoir species below 14 km altitude, while the ratio is shifted towards ClONO$_2$ between 14 and 24 km. In an overview of stratospheric polar winter chlorine partitioning by Santee et al. (2008), based on MLS and ACE-FTS satellite data, observations at $\theta = 500$ K in different years show different late winter patterns: In 2004/2005 in the Arctic, chlorine is mainly deactivated by ClONO$_2$ formation, which rises to about 60 % at the end of the winter, similar to the observations above 380 K in this work. Only later is chlorine slowly repartitioned into HCl through ClONO$_2$ photolysis towards the unperturbed conditions. The Arctic winter 2005/2006, instead, reveals a much faster build-up of HCl, similar to what Wilmouth et al. (2006) report and what is more reminiscent of the Antarctic stratosphere.

The general year-to-year variability in the northern hemispheric polar vortex is caused by high wave activity, which impacts the stability of the vortex and resultant cooling that occurs. On the process scale, the tradeoff between HCl or ClONO$_2$ recovery is controlled by the availability of reaction partners. NO$_2$ is needed for ClONO$_2$ formation, and may be introduced through mixing at the vortex edge (e.g. Krause et al., 2018), or through photolysis of gaseous HNO$_3$. HCl recovery is favoured if low ozone leaves enough Cl radicals to react with methane, which is typically the case in the lowermost stratosphere.

The same instruments used in the present study were previously used for measurements in the Antarctic polar vortex on 13 September 2012 at isentropes between 320 K and 385 K (Jurkat et al., 2017), where up to 40 % active chlorine was observed. Both the Arctic and Antarctic aircraft observations were made at (static) temperatures above 199 K, often even above 210 or 220 K. This is too warm for PSCs and for heterogeneous processes. Therefore, observable ClO$_x$ must have been activated beforehand, potentially with subsequent downward transport. The case study of strongly enhanced active chlorine at flight altitude, together with the presented trajectory calculations, reveals a similar mechanism and explores the spatial and temporal extent of such an event. This shows that, in both hemispheres, active chlorine can remain present in the vicinity of regions with temperatures below the PSC threshold.

5. Summary and Outlook

In the first section of this chapter the present work is summarised, highlighting the central findings of this work and checking the hypotheses from the introduction. The last section gives suggestions for future activities, especially on how the experimental methods presented in this thesis may be advanced.

5.1. Summary

This thesis uses novel in situ measurements of inorganic chlorine compounds sampled during the aircraft mission POLSTRACC in the Arctic polar winter 2015/2016. For the analysis of inorganic chlorine partitioning, in situ measurements of the reservoir gases HCl and $ClONO_2$ were performed, in combination with CFC-12 measurements for the derivation of total inorganic chlorine, Cl_y. This strategy contrasts many earlier airborne measurements that focused on the stratospheric polar chlorine activation, performing primarily measurements of ClO and ClOOCl. The study employs the AIMS mass spectrometer for the simultaneous measurement of HCl and $ClONO_2$. This assures correct collocation of the sampling of two important reservoir gases and to account for the overall instrumental performance and sensitivity. The accuracy of the measurement relies on the calibration and stability of the instrument and lies in the range of 10 % to 20 %. Permeation devices for HCl and HNO_3 in a custom made evaporator (permeation oven) were used, enabling regular and frequent calibration under varying environmental conditions during flights. The in flight calibration equipment was monitored carefully in the lab in long term measurements and instrumental and calibration drifts could be corrected. $ClONO_2$ sensitivities were derived from the HNO_3 calibration using the relative sensitivities of the kinetic constants reported in the literature. The measurements of the reservoir species showed an excellent agreement with Cl_y (derived from an independent measurement) in unperturbed conditions. As a consequence, the sum of the reactive (active) chlorine species (ClO_x) could be deduced wherever Cl_y exceeded the sum of the reservoir gases. As an additional improvement over the previous observations, ClO_x is not directly measurable (unless all included species are accurately sampled), but the current derived quantity is very robust to describe the ozone depleting potential of chlorine, as

it does not reflect the diurnal variability of its components. This also eases the comparability to model results, whereas comparisons to satellite observations are more challenging.

The polar vortex in winter 2015/2016 was characterised by unusual strength and extent, enabling low temperatures and rapid ozone depletion, comparable to the Antarctic counterpart. In spring, however, the Arctic vortex evolution came to an abrupt end through a major stratospheric warming. The dedicated aircraft mission targeted the Arctic lowermost stratosphere, including the outflow of the polar vortex, for an assessment of various characteristics of transport of air masses (including diabatic descent, isentropic transport across the vortex or tropopause boundaries and displacement through gravity waves) and in their composition (including photochemical processing and mixing). The dataset and analysis presented in this work, in the framework of the POLSTRACC campaign, aimed at observing the state of the lowermost Artic stratosphere over the course of an entire winter/early spring season, covering the major stages of the vortex evolution. The work contrasts previous airborne observations in the Arctic in 2000 (SOLVE/THESEO) and 2011 (RECONCILE) that focused on the understanding of processes involved in ozone depletion in the vortex using the higher flying WB-57 and Geophysica aircraft. Meanwhile it continued observations in a period that experienced significant changes in the load of pollutants and climate relevant trace gases in the atmosphere, accompanied by the coupled changes in the thermal structure, composition (including moisture), circulation and weather phenomena. Not only this required new observations on a new platform with updated equipment and strategy, but also the Arctic winter stratosphere itself challenges modelling and predictions as it is subject to higher interannual variability compared to the southern hemisphere.

The AIMS chlorine data obtained during the POLSTRACC campaign were evaluated within this thesis. In combination with other measurements and modelling results, the chlorine partitioning of the lowermost Arctic polar vortex was examined. The HALO aircraft's performance and the flight strategy provided a comprehensive sampling of air masses in and around the vortex. An established method for in situ identification of vortex air using N_2O was applied and refined to discriminate between intra and outside vortex air. Additionally the data were used for validation and comparison of the remote sensing infrared limb sounder GLORIA. The results of this study are summarised by reviewing and testing the hypotheses that were set up in the introductory chapter:

1. *Unlike the middle and upper stratosphere, tropopause-related gradients in trace gases impact the chlorine partitioning in the lowermost stratosphere throughout the polar winter.*
   In the free lower stratosphere, between about 400 and 520 K potential temperature, chlorine is fully activated in a strong polar vortex, in the Arctic and in the Antarctic (Manney and Lawrence, 2016; Santee et al., 2008). The new in situ measurements

show that this is not the case in the Arctic below 400 K, where gradients in the chlorine species initiate the transition to tropospheric conditions. This includes overall less inorganic chlorine, a reduced ratio of active chlorine and a shift in the partitioning of the reservoir species upon their recovery: HCl is quickly restored below 360 K, while $ClONO_2$ is predominant (within the observed early spring period) above 380 K, depending presumably on the availability of the reaction partners ozone or NO_2. Concluding, the chlorine partitioning in the lowermost vortex (or vortex outflow region) reflect the transition between conditions at the tropopause and in the stratospheric part of the vortex. As such, the composition is unique and had been only poorly sampled by previous campaigns or satellite platforms.

The present study is an important contribution to verifying model performance in this variable altitude range. The agreement of the measurements with the simulations of the CLaMS chemistry climate model is astonishing, showing that reanalysis meteorological fields, together with a chemistry model that sufficiently incorporates heterogeneous chemistry and transport processes in the stratosphere, reproduce the polar lower stratosphere generally well. Major uncertainties in the model persist in a systematic overestimation of HCl and in the tropospheric boundary conditions, which affect the composition of this stratospheric chemistry model in the lowermost stratospheric layers. As demonstrated in other literature work, the free running model EMAC shows less agreement with the measurements primarily due to the coarser resolution in the UTLS and misrepresented descent of the vortex (Johansson et al., 2019; Khosrawi et al., 2017). This thesis contributes to identify the subjects, location and extent of model uncertainties in order to improve their reliability and forecast/projection capabilities.

This work also demonstrates that the new local aircraft observations are able to reflect the larger scale patterns of active and repartitioned chlorine that characterise the overall vortex evolution. Active chlorine on the flight levels is found concurrent with activation maxima seen in satellite data at higher altitudes.

2. *The lowermost stratosphere can experience exceptionally high levels of active chlorine.*
   The ceiling altitude of HALO limits in situ observations to 15 km maximum altitude. While the presence of PSCs needed for large scale chlorine activation is restricted most of the time to altitudes above the flight level, active chlorine is observed at unexpectedly high levels up to 1.15 ppbv. This can be explained by strong (and mostly adiabatic) subsidence of air masses away from the activation region, which the CLaMS model also resolved in great detail. Beyond vague indications based on model data and sparse observations, the new evidence fosters the relevance of chlorine chemistry to the polar UTLS, where, in conjunction with enhanced mixing, previously activated

chlorine may increase the atmospheric oxidation capability, impacting the sensitive radiation budget not only through ozone removal, but also methane depletion. Future projections therefore need to incorporate the observable persistence of elevated levels of active chlorine (and other similar species).

Being able to answer both hypotheses at an unprecedented level of detail proves that this experimental approach, consisting of the instruments, campaign and flight strategy and data evaluation, is appropriate in addressing current and future questions concerning the characteristics, origin and impact of the trace gas composition in the UTLS region. It uniquely brings together the synoptic picture with the finer scale variations and gradients in chlorine processing in the outflow regions of the polar vortex. Yet the following section should lay out perspectives on how to improve and advance different aspects of the topic.

5.2. Outlook

After a short statement about stratospheric chlorine, the main and concluding parts of the outlook treat the future instrument design and propose new mission ideas.

5.2.1. Monitoring stratospheric chlorine

The Montreal Protocol has been in effect for more than 30 years, reducing the accumulation of long-lived and ozone depleting CFCs in the atmosphere. Along with the perceivable recovery of the Antarctic ozone hole (Strahan and Douglass, 2018), the treaty and its amendments are also attributed a mitigating effect on global warming, avoiding a 1.1 °C warming in the Arctic as of today and 1 °C global warming by mid century (Goyal et al., 2019), as CFCs and other controlled substitutes are themselves potent greenhouse gases. Top-down monitoring of the adherence to the protocol has to be continued, as new emissions would quickly counteract the tedious achievements of the past decades (Fang et al., 2018; Hegglin, 2018; Montzka et al., 2018).

The longevity of CFCs induces elevated chlorine levels in the stratosphere that shift the return of polar stratospheric ozone to 1980 (pre-emission) levels into the 2030ies (Arctic) to 2060 (Antarctic) (Dhomse et al., 2018). Future projections need to consider several important factors: Firstly, the evolution of polar ozone depletion varies each year due to interannual changes in the stratospheric circulation patterns. This leads to deviations from the climatological declining trend. Only very recently, the Antarctic experienced the rare event of a sudden stratospheric warming in 2019 (Safieddine et al., 2020), whereas Arctic ozone depletion reached a record high in 2020 (Dameris et al., 2020). It is a matter of current research to

estimate the frequency and strength of such deviating patterns in future scenarios. Secondly, the overall stratospheric cooling associated with tropospheric warming alters chemical reaction kinetics and may lead to enhanced nucleation of PSCs. Meanwhile, as CFCs gradually vanish, other sources for chlorine (i.e. VSLS), as well as other ODS such as brominated compounds or the stratospheric products of increased water vapour or N_2O gain in influence. Hence, the assessment of current state-of-the-art chemistry climate models with accurate observations is inevitable, especially in regions that are highly sensitive or that are only poorly resolved in the model scheme. Special emphasis deserve the crucial stages and processes of substances involved in ozone depletion, for example the transport of source or precursor compounds such as VSLS into the stratosphere, or the species directly involved in the catalytic cycles.

5.2.2. Future instrument development

Future activities with the AIMS instrument could encompass the direct calibration of $ClONO_2$. Although it is hardly possible to provide $ClONO_2$ at stratospheric concentration levels in the laboratory, a cross check measurement could be designed to verify the accuracy of the current indirect derivation method. The necessary infrastructure to supply $ClONO_2$ is available at DLR (Wagner and Birk, 2003) and was indeed used to derive spectroscopic properties of $ClONO_2$ for application in remote sensors like the MIPAS family or the GLORIA limb sounder. This provides an ideal experimental frame for a consistent calibration across the fields of in situ and remote sensing instruments.

While AIMS performs very well in a carefully executed deployment, it involves considerable efforts in preparation and operation of the mass spectrometer chamber, the inlet tubing and the calibration lines to achieve these high quality results, as the sensitivity and instrumental background depend on good vacuum conditions, clean and dry surfaces and equilibrated thermal conditioning. These factors are challenged by the aircraft operations, involving limited run up times, power outages and assignment and training of a dedicated operator in flight. Future deployments would therefore benefit from a number of modifications or redesigns of the instrument:

- Heating and thermal regulation has been gradually extended along the critical parts of the inlet line, enabling shorter conditioning and response times of several species, predominantly HNO_3. Temperature control should be extended to the flow tube segment, where the ionization of trace gas molecules exhibits temperature-dependent reaction kinetics. This would reduce the need of later drift correction of the sensitivity.

- The rods of the quadrupole could be redesigned to be heated as well. Other mass spectrometers apply this technique to actively remove remnants of ions which have

been trapped – by design – on the rod surface and which may accumulate to induce enhanced instrumental background and noise to the signal.

- Performing the measurements would benefit from a certain degree of automation, including for example triggering and controlling regular background measurements, or a spectral check and retuning, when required, or general status and error monitoring. This would significantly reduce the work load of the operating person, enabling a more flexible use of personnel on flight campaigns, which would certainly increase the attractiveness and demand for AIMS measurements in a – to some extent – competitive environment among airborne experiments.

- Some first tests were recently performed switching the sampling to a forward-facing inlet. This would in principle enable the study of condensed fractions of trace species, especially HNO_3 and HCl. A robust measurement, however, needs further development concerning the response to the different inlet flow and pressure, as well as dealing with effects of high condensed water content.

- Some additional species could be measured in addition by recording the respective product masses. A number of supplemental masses has been included in past deployments already, based on supposed product ions, but so far only for qualitative inspection. One example is formic acid ($HCOOH$), an important part of the (tropospheric) total acid budget, with implications on oxidation capability and precipitation (Millet et al., 2015). Another example is hydrogen cyanide (HCN) as a tracer for biomass burning (Li et al., 2009). A proper measurement requires the consideration of the (cross-) sensitivity of the respective mass and calibration, which could be easily realised with in-house equipment in the case of formic acid.

The AIMS trace gas measurements have been established as a vital contribution to a consolidated suite of experiments on board the HALO research aircraft for the worldwide observation of trace gas properties at altitudes around 10 to 15 km. While this suite was first fully operational within the POLSTRACC campaign treated in this thesis, it has yet been successfully redeployed for the WISE (Wave driven ISentropic Exchange, 2017) and South-TRAC (Southern hemisphere TRAnsport, dynamics and Composition, 2019) missions, both of which are still being evaluated at the time of writing.

The SouthTRAC campaign adapted some scientific targets from POLSTRACC. Measurements were conducted from September to November 2019 in the austral spring season. Based in Río Grande (Argentina) at the tip of the South American continent, it was possible to sample vortex-processed air masses characterised by high ozone depletion and dehydration. Also shifts in the chlorine reservoir species were observed. The chlorine analysis, with joint efforts of several working groups, will address the closure of the organic and inorganic chlorine

budget, its evolution through the late winter and spring season (similar to this thesis) and the different pathways of processing (activation/deactivation and connected redistribution) and mixing at the edge of the decaying Antarctic polar vortex. Many discoveries on stratospheric chlorine chemistry have been made in the southern hemispheric vortex due to its usually higher strength, associated by more intense chlorine activation and ozone depletion. The rare airborne in situ observations add valuable detail to satellite and model studies, inter alia treating the overestimated HCl in models, similar to this thesis. With similar payload employed on HALO during POLSTRACC and SouhtTRAC, the measurements are highly useful for an interhemispheric comparsion. In addition, the rare occurrence of a sudden stratospheric warming (SSW) terminating the 2019 Antarctic polar vortex was witnessed. It is now possible to examine its origin and impact on composition and climate.

AIMS has been, and will be, deployed in different contexts other than stratospheric chlorine chemistry. The past WISE (HALO, 2017) and BlueSky (DLR Falcon, 2020) campaigns, for example, take special advantage of the accurate nitric acid measurement, which is essential in respect of STE, nitrogen oxide budget and validation of the GLORIA remote sensor. In the planned Phileas campaign (HALO), nitric acid measurements will be performed in the outflow of the Asian monsoon anticyclone, targeting aerosol precursor studies and aerosol-cloud interactions. Also, sulfur dioxide (SO_2) observations have been valuable, and will be, in the context of aerosol formation, studying the stratospheric sulfate layer and volcanic emissions.

5.2.3. Future mission design

Thinking beyond the current and foreseeable activities, the question arises what other relevant topics emerge and how they may be addressed, based on the work in this thesis.

As the understanding of processes that control atmospheric composition is steadily deepened, models that describe the observed state and that project the future evolution of climate are ever improving at their performance. It is the subject of targeted airborne campaigns to thoroughly examine weak points and climate sensitive aspects of the current models.

A major challenging aspect in current climate modelling is the representation of heterogeneous processes, such as catalytic reactions or trapping of molecules inside condensates, due to their strongly increased number of degrees of freedom over pure gas or condensed phase processes. Some of these have been mentioned in this work. Such processes constitute important feedback systems or boundary conditions in climate models, and need to be well represented for precise weather and climate projections and estimations on mitigation potential.

5. Summary and Outlook

To experimentally resolve (heterogeneous) processes that run within minutes to hours, airborne missions could be designed that sample certain target air masses repeatedly. This could, for example, address the uptake or release of HCl and HNO_3 in cirrus particle that evolve depending on the degree of ice supersaturation. Such attempts have been made already, and especially in areas with strong advection or convection, their planning relies on an accurate and fast meteorological analysis. In that respect observations and tools have made significant progress in the recent years. The flight execution could involve returning patterns of one aircraft, crossing the same air mass several times, or multiple separated entities at defined evolution stages. The latter case, however, requires matching aircraft performance and comparable suites of instrumentation, which have been rarely achieved up to now. Mostly such a strategy involves the participation and funding of several partners and agencies.

Long term observations are incredibly valuable to observe trends in atmospheric composition and processing, as well as differential behaviour in repeated variations on the seasonal or (multi-) annual scale. This is proven not only by satellite or ground based observation time series, but also by the IAGOS (In-service Aircraft for a Global Observing System) project, which employs atmospheric sensors (e.g. for ozone or nitrogen oxides) on worldwide commercial air routes. Further development of instruments like AIMS could be headed towards a more compact and automatised design that allows a flexible deployment on such independent platforms.

Meanwhile, as this is a task for decades, it is worthwhile to perform dedicated aircraft campaigns repeatedly with similar targets. Combining the high resolution and precision of this data with the previous observations enables a very systematic advancement of knowledge.

Beyond, novel platforms could enhance the accessible space for observations. As an example, the performance of the unmanned Global Hawk enables extended measurements in the tropical tropopause region and in very remote areas. The former is also a promising target area for studying chlorine chemistry. Science should make further use of the new technology, by gaining access to such platforms and developing the instrumentation towards it.

Lastly, the conceptual understanding of atmospheric processes through modelling could advance if it were possible to flexibly adapt the spatiotemporal resolution and complexity of models to the sensitivity of certain areas. Several approaches have already been made in this direction, such as Lagrangian to nested grids. With respect of the sensitive UTLS region, especially a finer vertical resolution would allow for a more detailed representation of STE and heterogeneous processes.

The potential future instrument and campaign design presented in this chapter will help to improve our understanding of heterogeneous processes at the tropopause as well as transport processes and their impact on climate.

A. Appendix

Calibration of mass flow controllers The AIMS instrument includes four mass flow controllers (MFCs). The nitrogen (N_2) MFC delivers the carrier flow to the ion source. The synthetic air MFC is used for background measurements and as a clean (and dry) air supply on the ground. The bypass MFC ensures a constant bypass flow in flight (and hence a constant total mass flow). The SO_2 MFC is used for the isotopic SO_2 calibration.

Figure A.1 displays the calibration of the four MFCs. The MFCs were supplied by 2 bar of N_2 (synthetic air in case of the synthetic air MFC). The volume flow leaving the MFCs was measured by a Gilian Gilibrator 2 volume flow meter. Using ambient pressure and temperature, the standard flow was calculated, which is proportional to the mass flow. For synthetic air, the 10 slm MFC was only used a few days for a ground calibration sequence after the end of the POLSTRACC campaign. The data points were fitted (Fig. A.1 and Tab. A.1) and the fit functions are used to calculate the flow at arbitrary MFC settings during evaluation of the AIMS measurements.

Table A.1.: Parameters for the MFC fit functions visible in Fig. A.1. The linear functions of the standard flow f at the signal x read $f(x) = A + B \cdot x$. In case of the bypass MFC the function reads $f(x) = A(\exp(-C \cdot x) - 1) + B \cdot x$. Deviating units of the parameters are given in the table. Numbers in parentheses are the standard deviation in the last decimal digits.

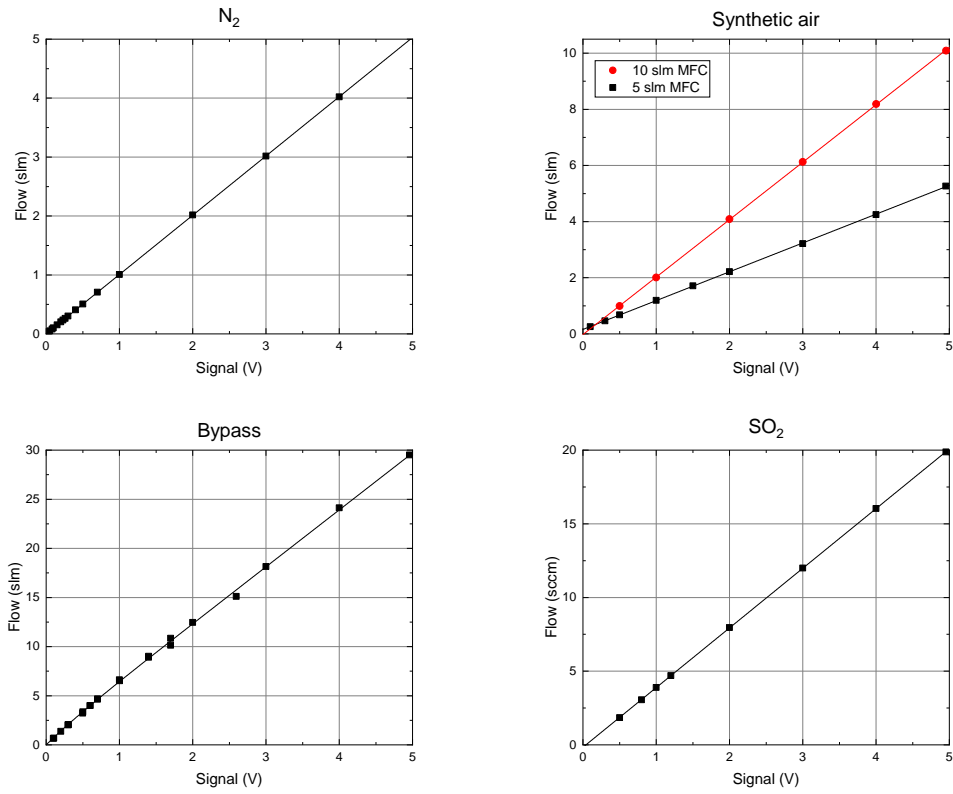| MFC	A (sccm)	B (sccm V^{-1})	C
N_2	2.09(49)	1005.31(34)	
Synthetic air 5 slm	159.3(82)	1026.6(33)	
Synthetic air 10 slm	-23(18)	2046.4(59)	
Bypass	-0.74(23) slm	5.794(72) slm V^{-1}	2.0(11) V^{-1}
SO_2	-0.164(11)	4.049(4)	

Figure A.1.: Calibration of the four MFCs of AIMS. The abscissa denotes the voltage signal in the range 0 to 5 V from the MFC. The ordinate displays the standard volume flow in standard litres per minute (slm) or standard cubic centimetres per minute (sccm). Two different MFCs were calibrated for synthetic air. The lines denote linear fits to the data (linear-exponential decay in the case of the bypass MFC). The functions and parameters are listed in Tab. A.1.

Acronyms, chemical species, symbols and units

Acronyms

AC	alternating current
ACE-FTS	Atmospheric Chemistry Experiment-Fourier Transform Spectrometer
ACIMS	active chemical ionization mass spectrometry
AENEAS	AtmosphEric Nitrogen oxides mEAsuring System (sometimes referred to as IPA-NO$_y$)
AIMS	AIrborne chemical ionization Mass Spectrometer
BDC	Brewer-Dobson circulation
CFC	chlorofluorocarbon (collective term)
CI	chemical ionization
CLaMS	Chemical Lagrangian Model of the Stratosphere
DC	direct current
DLR	Deutsches Zentrum für Luft- und Raumfahrt (German Aerospace Center)
ECMWF	European Centre for Medium-Range Weather Forecasts
ExTL	extratropical transition layer
GC	gas chromatograph
GhOST	Gas chromatograph for the Observation of Tracers – coupled with a Mass Spectrometer
GLORIA	Gimballed Limb Observer for Radiance Imaging of the Atmosphere
HALO	High Altitude and Long Range research aircraft
HYSPLIT	HYbrid Single-Particle Lagrangian Integrated Trajectory
IAGOS	In-service Aircraft for a Global Observing System
IPA	Institut für Physik der Atmosphäre (Institute of Atmospheric Physics)
LMS	lowermost stratosphere
MFC	mass flow controller
MFW	major final warming
MIPAS	Michelson Interferometer for Passive Atmospheric Sounding
MLS	Microwave Limb Sounder
MS	mass spectrometer
ODS	ozone depleting substance
PGI	product gas injection
PGS	POLSTRACC/GW-LCYCLE/SALSA (combined aircraft campaign)
POLSTRACC	POLar STRAtosphere in a Changing Climate
PSC	polar stratospheric cloud
SGI	source gas injection
SouthTRAC	Southern hemisphere TRAnsport, dynamics and Composition

SSW	sudden stratospheric warming
STE	stratosphere-troposphere exchange
SZA	solar zenith angle
TELIS	TErahertz and submillimeter LImb Sounder
TTL	tropical tropopause layer
UTC	coorinated universal time
UTLS	upper troposphere/lower stratosphere
UV	ultraviolet
VSLS	very short-lived substance
WISE	Wave-driven Isentropic Exchange

Chemical species

BrCl	bromine chloride
BrO	bromine oxide
CC	chlorocarbon
CCl_4	carbon tetrachloride
CF_3	trifluorocarbon
CFC-12	dichlorofluoromethane
CH_3Cl	methyl chloride
CH_4	methane
$CHCl_3$	chloroform
Cl	chlorine
Cl_2	molecular chlorine
Cl_2O_2	ClO dimer
Cl_y	total inorganic chlorine, $Cl_y = ClO_x + HCl + ClONO_2$
$ClNO_2$	nitryl chloride
$ClNO_3$	see $ClONO_2$
ClO	chlorine monoxide
ClO_x	active chlorine, $ClO_x = Cl + 2\,Cl_2 + ClO + 2\,ClOOCl + ClOO + HOCl$
$ClONO_2$	chlorine nitrate
ClOO	chlorine peroxide (sometimes referred to as OClO)
ClOOCl	see Cl_2O_2
CO_2	carbon dioxide
$COCl_2$	phosgene
F	fluorine
H_2O	water
H_2SO_4	sulfuric acid
HCFC	hydrochlorofluorocarbon
HCl	hydrogen chloride
HNO_3	nitric acid
HO_2	hydroperoxyl radical
HOCl	hypochlorous acid
HONO	nitrous acid
N	nitrogen
N_2	molecular nitrogen

N_2O	nitrous oxide
NAT	nitric acid trihydrate ($HNO_3 \cdot 3\,H_2O$), solid
NO	nitrogen oxide
NO_2	nitrogen dioxide
NO_3^-	nitrate ion
NO_x	reactive nitrogen oxides, $NO_x = NO + NO_2$
NO_y	sum of nitrogen oxides, $NO_y = NO_x + HNO_3 + N_2O_5 + PAN + HONO + \ldots$
O	oxygen
O_2	molecular oxygen
O_3	ozone
OH	hydroxyl radical
PFA	perfluoroalkoxy alkane
SCF_8	trifluoromethylsulfur pentafluoride
SF_5^-	sulfur pentafluoride ion
SF_6	sulfur hexafluoride
SO_2	sulfur dioxide

Symbols and units

β	dilution factor
c	speed of light in vacuum, $c = 299792458\ \mathrm{m\ s^{-1}}$
CF_i	calibration factor for trace gas ion X_iF^-
h	Planck constant, $h = 6.62607015 \cdot 10^{-34}\ \mathrm{J\ s}$
k_i	reaction rate constant for trace gas X_i
λ	wavelength of electromagnetic radiation
md_i	mass discrimination factor for trace gas ion X_iF^-
μ	transmission efficiency of the inlet line
N	number of measurements in running average window
N^2	Brunt-Väisälä (buoyancy) frequency squared
ν	frequency of electromagnetic radiation
ppbv	parts per billion by volume; unit of the molar mixing ratio times 10^9
ppmv	parts per million by volume; unit of the molar mixing ratio times 10^6
pptv	parts per trillion by volume; unit of the molar mixing ratio times 10^{12}
PV	potential vorticity
PVU	potential vorticity unit; $1\,\mathrm{PVU} = 10^{-6}\ \mathrm{K\ m^2\ kg^{-1}\ s^{-1}}$
r	count rate
s_i	sensitivity for trace gas ion X_iF^-
σ	standard deviation
slm	standard litres per minute; unit of the mass flow. Standard conditions: 1013.25 mbar and 0 °C
T	temperature
τ	reaction time
θ	potential temperature
u	atomic mass unit; $1\,\mathrm{u} = 1.66053906660(50) \cdot 10^{-27}\ \mathrm{kg}$
X_i	trace gas with index i
$[X_i]$	number concentration of trace gas X_i

Lists of figures and tables

List of Figures

List of Tables

Bibliography

Bekki, S., A. Rap, V. Poulain, S. Dhomse, M. Marchand, F. Lefevre, P. Forster, S. Szopa, and M. Chipperfield (2013). "Climate impact of stratospheric ozone recovery". In: *Geophys. Res. Lett.* 40.11, pp. 2796–2800. DOI: 10.1002/grl.50358.

Bonne, G. P., R. M. Stimpfle, R. C. Cohen, P. B. Voss, K. K. Perkins, J. G. Anderson, R. J. Salawitch, J. W. Elkins, G. S. Dutton, K. W. Jucks, and G. C. Toon (2000). "An examination of the inorganic chlorine budget in the lower stratosphere". In: *J. Geophy. Res. Atmos.* 105.D2, pp. 1957–1971. DOI: 10.1029/1999jd900996.

Borrmann, S., S. Solomon, J. E. Dye, and B. Luo (1996). "The potential of cirrus clouds for heterogeneous chlorine activation". In: *Geophys. Res. Lett.* 23.16, pp. 2133–2136. DOI: 10.1029/96gl01957.

Brauer, G. (1960). *Handbuch der Präparativen Anorganischen Chemie*. 2. umgearbeitete Auflage. Vol. 1. Stuttgart: Enke Verlag.

Braun, M., J.-U. Grooß, W. Woiwode, S. Johansson, M. Höpfner, F. Friedl-Vallon, H. Oelhaf, P. Preusse, J. Ungermann, B.-M. Sinnhuber, H. Ziereis, and P. Braesicke (2019). "Nitrification of the lowermost stratosphere during the exceptionally cold Arctic winter 2015–2016". In: *Atmos. Chem. Phys.* 19.21, pp. 13681–13699. DOI: 10.5194/acp-19-13681-2019.

Burrows, J., A. Richter, A. Dehn, B. Deters, S. Himmelmann, S. Voigt, and J. Orphal (1999). "Atmospheric remote-sensing reference data from GOME-2. Temperature-dependent absorption cross sections of O_3 in the 231–794 nm range". In: *J. Quant. Spectrosc. Radiat. Transfer* 61.4, pp. 509–517. DOI: 10.1016/s0022-4073(98)00037-5.

Carslaw, K. S., B. P. Luo, S. L. Clegg, T. Peter, P. Brimblecombe, and P. J. Crutzen (1994). "Stratospheric aerosol growth and HNO_3 gas phase depletion from coupled HNO_3 and water uptake by liquid particles". In: *Geophys. Res. Lett.* 21.23, pp. 2479–2482. DOI: 10.1029/94gl02799.

Clarmann, T. von and S. Johansson (2018). "Chlorine nitrate in the atmosphere". In: *Atmos. Chem. Phys.* 18.20, pp. 15363–15386. DOI: 10.5194/acp-18-15363-2018.

Crutzen, P. J. (1970). "The influence of nitrogen oxides on the atmospheric ozone content". In: *Q. J. R. Meteorol. Soc.* 96.408, pp. 320–325. DOI: 10.1002/qj.49709640815.

Crutzen, P. J. and F. Arnold (1986). "Nitric acid cloud formation in the cold Antarctic stratosphere: a major cause for the springtime 'ozone hole'". In: *Nature* 324.6098, pp. 651–655. DOI: 10.1038/324651a0.

Bibliography

Dameris, M., M. Rex, and C. Voigt (2011). "FCKW und die Ozonschicht – Eine folgenreiche Erkenntnis". In: *Chemie über den Wolken ... und darunter*. Ed. by Zellner, R. and GDCH. Wiley-VCH, pp. 194–204.

Dameris, M., D. G. Loyola, M. Nützel, M. Coldewey-Egbers, C. Lerot, F. Romahn, and M. van Roozendael (2020). "First description and classification of the ozone hole over the Arctic in boreal spring 2020". In: *Atmos. Chem. Phys.* DOI: 10.5194/acp-2020-746.

Daniel, J. S., S. Solomon, R. W. Portmann, and R. R. Garcia (1999). "Stratospheric ozone destruction: The importance of bromine relative to chlorine". In: *J. Geophys. Res. Atmos.* 104.D19, pp. 23871–23880. DOI: 10.1029/1999jd900381.

Dee, D. P., S. M. Uppala, A. J. Simmons, P. Berrisford, P. Poli, S. Kobayashi, U. Andrae, M. A. Balmaseda, G. Balsamo, P. Bauer, P. Bechtold, A. C. M. Beljaars, L. van de Berg, J. Bidlot, N. Bormann, C. Delsol, R. Dragani, M. Fuentes, A. J. Geer, L. Haimberger, S. B. Healy, H. Hersbach, E. V. Hólm, L. Isaksen, P. Kållberg, M. Köhler, M. Matricardi, A. P. McNally, B. M. Monge-Sanz, J.-J. Morcrette, B.-K. Park, C. Peubey, P. de Rosnay, C. Tavolato, J.-N. Thépaut, and F. Vitart (2011). "The ERA-Interim reanalysis: configuration and performance of the data assimilation system". In: *Q. J. R. Meteorol. Soc.* 137.656, pp. 553–597. DOI: 10.1002/qj.828.

Dhomse, S. S., D. Kinnison, M. P. Chipperfield, R. J. Salawitch, I. Cionni, M. I. Hegglin, N. L. Abraham, H. Akiyoshi, A. T. Archibald, E. M. Bednarz, S. Bekki, P. Braesicke, N. Butchart, M. Dameris, M. Deushi, S. Frith, S. C. Hardiman, B. Hassler, L. W. Horowitz, R.-M. Hu, P. Jöckel, B. Josse, O. Kirner, S. Kremser, U. Langematz, J. Lewis, M. Marchand, M. Lin, E. Mancini, V. Marécal, M. Michou, O. Morgenstern, F. M. O'Connor, L. Oman, G. Pitari, D. A. Plummer, J. A. Pyle, L. E. Revell, E. Rozanov, R. Schofield, et al. (2018). "Estimates of ozone return dates from Chemistry-Climate Model Initiative simulations". In: *Atmos. Chem. Phys.* 18.11, pp. 8409–8438. DOI: 10.5194/acp-18-8409-2018.

Dörnbrack, A., S. Gisinger, M. C. Pitts, L. R. Poole, and M. Maturilli (2017). "Multilevel Cloud Structures over Svalbard". In: *Mon. Weather Rev.* 145.4, pp. 1149–1159. DOI: 10.1175/mwr-d-16-0214.1.

Draxler, R. R. and G. D. Hess (1998). "An overview of the HYSPLIT_4 modelling system for trajectories, dispersion, and deposition". In: *Aust. Meteorol. Mag.* 47.4, pp. 295–308.

Drdla, K. and R. Müller (2012). "Temperature thresholds for chlorine activation and ozone loss in the polar stratosphere". In: *Ann. Geophys.* 30.7, pp. 1055–1073. DOI: 10.5194/angeo-30-1055-2012.

Fahey, D. W., R. S. Gao, K. S. Carslaw, J. Kettleborough, P. J. Popp, M. J. Northway, J. C. Holecek, S. C. Ciciora, R. J. McLaughlin, T. L. Thompson, R. H. Winkler, D. G. Baumgardner, B. Gandrud, P. O. Wennberg, S. Dhaniyala, K. McKinney, T. Peter, R. J. Salawitch, T. P. Bui, J. W. Elkins, C. R. Webster, E. L. Atlas, H. Jost, J. C. Wilson, R. L. Herman, A. Kleinböhl, and M. von König (2001). "The Detection of Large HNO$_3$-Containing

Particles in the Winter Arctic Stratosphere". In: *Science* 291.5506, pp. 1026–1031. DOI: 10.1126/science.1057265.

Fang, X., S. Park, T. Saito, R. Tunnicliffe, A. L. Ganesan, M. Rigby, S. Li, Y. Yokouchi, P. J. Fraser, C. M. Harth, P. B. Krummel, J. Mühle, S. O'Doherty, P. K. Salameh, P. G. Simmonds, R. F. Weiss, D. Young, M. F. Lunt, A. J. Manning, A. Gressent, and R. G. Prinn (2018). "Rapid increase in ozone-depleting chloroform emissions from China". In: *Nat. Geosci.* 12.2, pp. 89–93. DOI: 10.1038/s41561-018-0278-2.

Forster, P. M. d. and K. P. Shine (2002). "Assessing the climate impact of trends in stratospheric water vapor". In: *Geophys. Res. Lett.* 29.6, pp. 10–1–10–4. DOI: 10.1029/2001gl013909.

Gettelman, A., P. Hoor, L. L. Pan, W. J. Randel, M. I. Hegglin, and T. Birner (2011). "The extratropical upper troposphere and lower stratosphere". In: *Rev. Geophys.* 49.3. DOI: 10.1029/2011rg000355.

Goldfarb, L., A.-M. Schmoltner, M. K. Gilles, J. B. Burkholder, and A. R. Ravishankara (1997). "Photodissociation of ClONO2: 1. Atomic Resonance Fluorescence Measurements of Product Quantum Yields". In: *J. Phys. Chem. A* 101.36, pp. 6658–6666. DOI: 10.1021/jp970818f.

Goyal, R., M. H. England, A. S. Gupta, and M. Jucker (2019). "Reduction in surface climate change achieved by the 1987 Montreal Protocol". In: *Environ. Res. Lett.* 14.12, p. 124041. DOI: 10.1088/1748-9326/ab4874.

Graedel, T. E. and P. J. Crutzen (1992). *Atmospheric Change: An Earth System Perspective.* W H Freeman & Co, New York. ISBN: 0716723344.

Graedel, T. E. and W. C. Keene (1995). "Tropospheric budget of reactive chlorine". In: *Global Biogeochem. Cycles* 9.1, pp. 47–77. DOI: 10.1029/94gb03103.

– (1996). "The Budget and Cycle of Earth's Natural Chlorine". In: *Pure Appl. Chem.* 68.9, pp. 1689–1697. DOI: 10.1351/pac199668091689.

Greenblatt, J. B., H.-J. Jost, M. Loewenstein, J. R. Podolske, T. P. Bui, D. F. Hurst, J. W. Elkins, R. L. Herman, C. R. Webster, S. M. Schauffler, E. L. Atlas, P. A. Newman, L. R. Lait, M. Müller, A. Engel, and U. Schmidt (2002). "Defining the polar vortex edge from an N_2O:potential temperature correlation". In: *J. Geophys. Res. Atmos.* 107.D20. 8268, SOL 10-1–SOL 10-9. ISSN: 2156-2202. DOI: 10.1029/2001JD000575.

Grimvall, A. and E. W. B. de Leer, eds. (1995). *Naturally-Produced Organohalogens.* Springer Netherlands. DOI: 10.1007/978-94-011-0061-8.

Grooß, J.-U. and J. M. Russell (2005). "Technical note: A stratospheric climatology for O_3, H_2O, CH_4, NO_x, HCl and HF derived from HALOE measurements". In: *Atmos. Chem. Phys.* 5.10, pp. 2797–2807. DOI: 10.5194/acp-5-2797-2005.

Grooß, J.-U. and R. Müller (2007). "Simulation of ozone loss in Arctic winter 2004/2005". In: *Geophys. Res. Lett.* 34.5. DOI: 10.1029/2006gl028901.

Grooß, J.-U., I. Engel, S. Borrmann, W. Frey, G. Günther, C. R. Hoyle, R. Kivi, B. P. Luo, S. Molleker, T. Peter, M. C. Pitts, H. Schlager, G. Stiller, H. Vömel, K. A. Walker, and

R. Müller (2014). "Nitric acid trihydrate nucleation and denitrification in the Arctic stratosphere". In: *Atmos. Chem. Phys.* 14.2, pp. 1055–1073. DOI: 10.5194/acp-14-1055-2014.

Grooß, J.-U., P. Konopka, and R. Müller (2005). "Ozone Chemistry during the 2002 Antarctic Vortex Split". In: *J. Atmos. Sci.* 62.3, pp. 860–870. DOI: 10.1175/jas-3330.1.

Grooß, J.-U., R. Müller, R. Spang, I. Tritscher, T. Wegner, M. P. Chipperfield, W. Feng, D. E. Kinnison, and S. Madronich (2018). "On the discrepancy of HCl processing in the core of the wintertime polar vortices". In: *Atmos. Chem. Phys.* 18.12, pp. 8647–8666. DOI: 10.5194/acp-18-8647-2018.

Groß, S., M. Wirth, A. Schäfler, A. Fix, S. Kaufmann, and C. Voigt (2014). "Potential of airborne lidar measurements for cirrus cloud studies". In: *Atmos. Meas. Tech.* 7.8, pp. 2745–2755. DOI: 10.5194/amt-7-2745-2014.

Hanson, D. and K. Mauersberger (1988). "Laboratory studies of the nitric acid trihydrate: Implications for the south polar stratosphere". In: *Geophys. Res. Lett.* 15.8, pp. 855–858. DOI: 10.1029/gl015i008p00855.

Harrison, J. J., M. P. Chipperfield, R. Hossaini, C. D. Boone, S. Dhomse, W. Feng, and P. F. Bernath (2019). "Phosgene in the Upper Troposphere and Lower Stratosphere: A Marker for Product Gas Injection Due to Chlorine-Containing Very Short Lived Substances". In: *Geophys. Res. Lett.* 46.2, pp. 1032–1039. DOI: 10.1029/2018gl079784.

Hegglin, M. I. (2018). "Evidence of illegal emissions of ozone-depleting chemicals". In: *Nature* 557.7705, pp. 317–318. DOI: 10.1038/d41586-018-05110-3.

Hobe, M. von, J.-U. Grooß, R. Müller, S. Hrechanyy, U. Winkler, and F. Stroh (2005). "A re-evaluation of the ClO/Cl$_2$O$_2$ equilibrium constant based on stratospheric in-situ observations". In: *Atmos. Chem. Phys.* 5.3, pp. 693–702. DOI: 10.5194/acp-5-693-2005.

Hobe, M. von, J.-U. Grooß, G. Günther, P. Konopka, I. Gensch, M. Krämer, N. Spelten, A. Afchine, C. Schiller, A. Ulanovsky, N. Sitnikov, G. Shur, V. Yushkov, F. Ravegnani, F. Cairo, A. Roiger, C. Voigt, H. Schlager, R. Weigel, W. Frey, S. Borrmann, R. Müller, and F. Stroh (2011). "Evidence for heterogeneous chlorine activation in the tropical UTLS". In: *Atmos. Chem. Phys.* 11.1, pp. 241–256. DOI: 10.5194/acp-11-241-2011.

Hobe, M. von, S. Bekki, S. Borrmann, F. Cairo, F. D'Amato, G. D. Donfrancesco, A. Dörnbrack, A. Ebersoldt, M. Ebert, C. Emde, I. Engel, M. Ern, W. Frey, S. Genco, S. Griessbach, J.-U. Grooß, T. Gulde, G. Günther, E. Hösen, L. Hoffmann, V. Homonnai, C. R. Hoyle, I. S. A. Isaksen, D. R. Jackson, I. M. Jánosi, R. L. Jones, K. Kandler, C. Kalicinsky, A. Keil, S. M. Khaykin, F. Khosrawi, R. Kivi, J. Kuttippurath, J. C. Laube, F. Lefèvre, R. Lehmann, S. Ludmann, B. P. Luo, M. Marchand, J. Meyer, et al. (2013). "Reconciliation of essential process parameters for an enhanced predictability of Arctic stratospheric ozone loss and its climate interactions (RECONCILE): activities and results". In: *Atmos. Chem. Phys.* 13.18, pp. 9233–9268. DOI: 10.5194/acp-13-9233-2013.

Holton, J. R., P. H. Haynes, M. E. McIntyre, A. R. Douglass, R. B. Rood, and L. Pfister (1995). "Stratosphere-troposphere exchange". In: *Rev. Geophys.* 33.4, p. 403. DOI: 10.1029/95rg02097.

Hoor, P., H. Fischer, L. Lange, J. Lelieveld, and D. Brunner (2002). "Seasonal variations of a mixing layer in the lowermost stratosphere as identified by the CO-O_3 correlation from in situ measurements". In: *J. Geophys. Res. Atmos.* 107.D5, ACL 1–1–ACL 1–11. DOI: 10.1029/2000jd000289.

Hoor, P., C. Gurk, D. Brunner, M. I. Hegglin, H. Wernli, and H. Fischer (2004). "Seasonality and extent of extratropical TST derived from in-situ CO measurements during SPURT". In: *Atmos. Chem. Phys.* 4.5, pp. 1427–1442. DOI: 10.5194/acp-4-1427-2004.

Hoor, P., H. Wernli, M. I. Hegglin, and H. Bönisch (2010). "Transport timescales and tracer properties in the extratropical UTLS". In: *Atmos. Chem. Phys.* 10.16, pp. 7929–7944. DOI: 10.5194/acp-10-7929-2010.

Hossaini, R., M. P. Chipperfield, A. Saiz-Lopez, J. J. Harrison, R. Glasow, R. Sommariva, E. Atlas, M. Navarro, S. A. Montzka, W. Feng, S. Dhomse, C. Harth, J. Mühle, C. Lunder, S. O'Doherty, D. Young, S. Reimann, M. K. Vollmer, P. B. Krummel, and P. F. Bernath (2015). "Growth in stratospheric chlorine from short-lived chemicals not controlled by the Montreal Protocol". In: *Geophys. Res. Lett.* 42.11, pp. 4573–4580. DOI: 10.1002/2015gl063783.

Hossaini, R., E. Atlas, S. S. Dhomse, M. P. Chipperfield, P. F. Bernath, A. M. Fernando, J. Mühle, A. A. Leeson, S. A. Montzka, W. Feng, J. J. Harrison, P. Krummel, M. K. Vollmer, S. Reimann, S. O'Doherty, D. Young, M. Maione, J. Arduini, and C. R. Lunder (2019). "Recent Trends in Stratospheric Chlorine from Very Short-Lived Substances". In: *J. Geophys. Res. Atmos.* DOI: 10.1029/2018jd029400.

Huang, J., J. Huang, X. Liu, C. Li, L. Ding, and H. Yu (2018). "The global oxygen budget and its future projection". In: *Sci. Bull.* 63.18, pp. 1180–1186. DOI: 10.1016/j.scib.2018.07.023.

IPCC (2018). *Global Warming of 1.5°C. An IPCC Special Report on the impacts of global warming of 1.5°C above pre-industrial levels and related global greenhouse gas emission pathways, in the context of strengthening the global response to the threat of climate change, sustainable development, and efforts to eradicate poverty.* Ed. by Masson-Delmotte, V., Zhai, P., Pörtner, H.-O., Roberts, D., Skea, J., Shukla, P. R., Pirani, A., Moufouma-Okia, W., Péan, C., Pidcock, R., Connors, S., Matthews, J. B. R., Chen, Y., Zhou, X., Gomis, M. I., Lonnoy, E., Maycock, T., Tignor, M., and Waterfield, T. World Meteorological Organization, Geneva, Switzerland.

Jeßberger, P. (2013). "Messungen von salpetriger Säure und Eispartikeln im Nachlauf von Flugzeugen". PhD thesis. Universität Mainz.

Johansson, S., W. Woiwode, M. Höpfner, F. Friedl-Vallon, A. Kleinert, E. Kretschmer, T. Latzko, J. Orphal, P. Preusse, J. Ungermann, M. L. Santee, T. Jurkat-Witschas, A. Marsing,

C. Voigt, A. Giez, M. Krämer, C. Rolf, A. Zahn, A. Engel, B.-M. Sinnhuber, and H. Oelhaf (2018). "Airborne limb-imaging measurements of temperature, HNO_3, O_3, $ClONO_2$, H_2O and CFC-12 during the Arctic winter 2015/2016: characterization, in situ validation and comparison to Aura/MLS". In: *Atmos. Meas. Tech.* 11.8, pp. 4737–4756. DOI: 10.5194/amt-11-4737-2018.

Johansson, S., M. L. Santee, J.-U. Grooß, M. Höpfner, M. Braun, F. Friedl-Vallon, F. Khosrawi, O. Kirner, E. Kretschmer, H. Oelhaf, J. Orphal, B.-M. Sinnhuber, I. Tritscher, J. Ungermann, K. A. Walker, and W. Woiwode (2019). "Unusual chlorine partitioning in the 2015/16 Arctic winter lowermost stratosphere: observations and simulations". In: *Atmos. Chem. Phys.* 19.12, pp. 8311–8338. DOI: 10.5194/acp-19-8311-2019.

Jurkat, T. (2010). "Airborne ion trap CIMS using SF_5^- reagent ions: Atmospheric trace gas detection in the tropopause region and in aircraft exhaust plumes". PhD thesis. University of Heidelberg.

Jurkat, T., C. Voigt, F. Arnold, H. Schlager, H. Aufmhoff, J. Schmale, J. Schneider, M. Lichtenstern, and A. Dörnbrack (2010). "Airborne stratospheric ITCIMS measurements of SO_2, HCl, and HNO_3 in the aged plume of volcano Kasatochi". In: *J. Geophys. Res.* 115, p. D00L17. DOI: 10.1029/2010jd013890.

Jurkat, T., C. Voigt, S. Kaufmann, A. Zahn, M. Sprenger, P. Hoor, H. Bozem, S. Müller, A. Dörnbrack, H. Schlager, H. Bönisch, and A. Engel (2014). "A quantitative analysis of stratospheric HCl, HNO_3, and O_3 in the tropopause region near the subtropical jet". In: *Geophys. Res. Lett.* 41.9, pp. 3315–3321. DOI: 10.1002/2013gl059159.

Jurkat, T., S. Kaufmann, C. Voigt, D. Schäuble, P. Jeßberger, and H. Ziereis (2016). "The airborne mass spectrometer AIMS – Part 2: Measurements of trace gases with stratospheric or tropospheric origin in the UTLS". In: *Atmos. Meas. Tech.* 9.4, pp. 1907–1923. DOI: 10.5194/amt-9-1907-2016.

Jurkat, T., C. Voigt, S. Kaufmann, J.-U. Grooß, H. Ziereis, A. Dörnbrack, P. Hoor, H. Bozem, A. Engel, H. Bönisch, T. Keber, T. Hüneke, K. Pfeilsticker, A. Zahn, K. A. Walker, C. D. Boone, P. F. Bernath, and H. Schlager (2017). "Depletion of ozone and reservoir species of chlorine and nitrogen oxide in the lower Antarctic polar vortex measured from aircraft". In: *Geophys. Res. Lett.* 44.12, pp. 6440–6449. DOI: 10.1002/2017gl073270.

Kaufmann, S. (2013). "Massenspektrometrische Wasserdampfmessung in der oberen Troposphäre und unteren Stratosphäre". PhD thesis. Universität Mainz.

Kaufmann, S., C. Voigt, T. Jurkat, T. Thornberry, D. W. Fahey, R.-S. Gao, R. Schlage, D. Schäuble, and M. Zöger (2016). "The airborne mass spectrometer AIMS – Part 1: AIMS-H_2O for UTLS water vapor measurements". In: *Atmos. Meas. Tech.* 9.3, pp. 939–953. DOI: 10.5194/amt-9-939-2016.

Kaufmann, S., C. Voigt, R. Heller, T. Jurkat-Witschas, M. Krämer, C. Rolf, M. Zöger, A. Giez, B. Buchholz, V. Ebert, T. Thornberry, and U. Schumann (2018). "Intercomparison of midlatitude tropospheric and lower-stratospheric water vapor measurements and com-

parison to ECMWF humidity data". In: *Atmos. Chem. Phys.* 18.22, pp. 16729–16745. DOI: 10.5194/acp-18-16729-2018.

Keber, T., H. Bönisch, C. Hartick, M. Hauck, F. Lefrancois, F. Obersteiner, A. Ringsdorf, N. Schohl, T. Schuck, R. Hossaini, P. Graf, P. Jöckel, and A. Engel (2020). "Bromine from short-lived source gases in the extratropical northern hemispheric upper troposphere and lower stratosphere (UTLS)". In: *Atmos. Chem. Phys.* 20.7, pp. 4105–4132. DOI: 10.5194/acp-20-4105-2020.

Keene, W. C., M. A. K. Khalil, D. J. Erickson, A. McCulloch, T. E. Graedel, J. M. Lobert, M. L. Aucott, S. L. Gong, D. B. Harper, G. Kleiman, P. Midgley, R. M. Moore, C. Seuzaret, W. T. Sturges, C. M. Benkovitz, V. Koropalov, L. A. Barrie, and Y. F. Li (1999). "Composite global emissions of reactive chlorine from anthropogenic and natural sources: Reactive Chlorine Emissions Inventory". In: *J. Geophys. Res. Atmos.* 104.D7, pp. 8429–8440. DOI: 10.1029/1998jd100084.

Khosrawi, F., O. Kirner, B.-M. Sinnhuber, S. Johansson, M. Höpfner, M. L. Santee, L. Froidevaux, J. Ungermann, R. Ruhnke, W. Woiwode, H. Oelhaf, and P. Braesicke (2017). "Denitrification, dehydration and ozone loss during the 2015/2016 Arctic winter". In: *Atmos. Chem. Phys.* 17.21, pp. 12893–12910. DOI: 10.5194/acp-17-12893-2017.

Knudsen, B. M., N. Larsen, I. S. Mikkelsen, J.-J. Morcrette, G. O. Braathen, E. Kyrö, H. Fast, H. Gernandt, H. Kanzawa, H. Nakane, V. Dorokhov, V. Yushkov, G. Hansen, M. Gil, and R. J. Shearman (1998). "Ozone depletion in and below the Arctic Vortex for 1997". In: *Geophys. Res. Lett.* 25.5, pp. 627–630. DOI: 10.1029/98gl00300.

Knudsen, B. M. and J.-U. Grooß (2000). "Northern midlatitude stratospheric ozone dilution in spring modeled with simulated mixing". In: *J. Geophys. Res. Atmos.* 105.D5, pp. 6885–6890. DOI: 10.1029/1999jd901076.

Krause, J., P. Hoor, A. Engel, F. Plöger, J.-U. Grooß, H. Bönisch, T. Keber, B.-M. Sinnhuber, W. Woiwode, and H. Oelhaf (2018). "Mixing and ageing in the polar lower stratosphere in winter 2015–2016". In: *Atmos. Chem. Phys.* 18.8, pp. 6057–6073. DOI: 10.5194/acp-18-6057-2018.

Krisch, I., P. Preusse, J. Ungermann, A. Dörnbrack, S. D. Eckermann, M. Ern, F. Friedl-Vallon, M. Kaufmann, H. Oelhaf, M. Rapp, C. Strube, and M. Riese (2017). "First tomographic observations of gravity waves by the infrared limb imager GLORIA". In: *Atmos. Chem. Phys.* 17.24, pp. 14937–14953. DOI: 10.5194/acp-17-14937-2017.

Krisch, I., M. Ern, L. Hoffmann, P. Preusse, C. Strube, J. Ungermann, W. Woiwode, and M. Riese (2020). "Superposition of gravity waves with different propagation characteristics observed by airborne and space-borne infrared sounders". In: *Atmos. Chem. Phys.* 20.19, pp. 11469–11490. DOI: 10.5194/acp-20-11469-2020.

Li, Q., P. I. Palmer, H. C. Pumphrey, P. Bernath, and E. Mahieu (2009). "What drives the observed variability of HCN in the troposphere and lower stratosphere?" In: *Atmos. Chem. Phys.* 9.21, pp. 8531–8543. DOI: 10.5194/acp-9-8531-2009.

Bibliography

Livesey, N. J., W. G. Read, P. A. Wagner, L. Froidevaux, A. Lambert, G. L. Manney, L. F. M. Valle, H. C. Pumphrey, M. L. Santee, M. J. Schwartz, S. Wang, R. A. Fuller, R. F. Jarnot, B. W. Knosp, and E. Martinez (2017). *Earth Observing System (EOS): Aura Microwave Limb Sounder (MLS): Version 4.2x Level 2 data quality and description document.* Jet Propulsion Laboratory (JPL), California Institute of Technology. Pasadena, California.

Mahieu, E., P. Duchatelet, P. Demoulin, K. A. Walker, E. Dupuy, L. Froidevaux, C. Randall, V. Catoire, K. Strong, C. D. Boone, P. F. Bernath, J.-F. Blavier, T. Blumenstock, M. Coffey, M. D. Mazière, D. Griffith, J. Hannigan, F. Hase, N. Jones, K. W. Jucks, A. Kagawa, Y. Kasai, Y. Mebarki, S. Mikuteit, R. Nassar, J. Notholt, C. P. Rinsland, C. Robert, O. Schrems, C. Senten, D. Smale, J. Taylor, C. Tétard, G. C. Toon, T. Warneke, S. W. Wood, R. Zander, and C. Servais (2008). "Validation of ACE-FTS v2.2 measurements of HCl, HF, CCl_3F and CCl_2F_2 using space-, balloon- and ground-based instrument observations". In: *Atmos. Chem. Phys.* 8.20, pp. 6199–6221. DOI: 10.5194/acp-8-6199-2008.

Manney, G. L. and J. L. Sabutis (2000). "Development of the polar vortex in the 1999-2000 Arctic winter stratosphere". In: *Geophys. Res. Lett.* 27.17, pp. 2589–2592. DOI: 10.1029/2000gl011703.

Manney, G. L. and Z. D. Lawrence (2016). "The major stratospheric final warming in 2016: dispersal of vortex air and termination of Arctic chemical ozone loss". In: *Atmos. Chem. Phys.* 16.23, pp. 15371–15396. DOI: 10.5194/acp-16-15371-2016.

Marcy, T. P., D. W. Fahey, R. S. Gao, P. J. Popp, E. C. Richard, T. L. Thompson, K. H. Rosenlof, E. A. Ray, R. J. Salawitch, C. S. Atherton, D. J. Bergmann, B. A. Ridley, A. J. Weinheimer, M. Loewenstein, E. M. Weinstock, and M. J. Mahoney (2004). "Quantifying Stratospheric Ozone in the Upper Troposphere with in Situ Measurements of HCl". In: *Science* 304.5668, pp. 261–265. DOI: 10.1126/science.1093418.

Marcy, T. P., R. Gao, M. Northway, P. Popp, H. Stark, and D. Fahey (2005). "Using chemical ionization mass spectrometry for detection of HNO_3, HCl, and $ClONO_2$ in the atmosphere". In: *Int. J. Mass Spectrom.* 243.1, pp. 63–70. DOI: 10.1016/j.ijms.2004.11.012.

Marsing, A., T. Jurkat-Witschas, J.-U. Grooß, S. Kaufmann, R. Heller, A. Engel, P. Hoor, J. Krause, and C. Voigt (2019). "Chlorine partitioning in the lowermost Arctic vortex during the cold winter 2015/2016". In: *Atmos. Chem. Phys.* 19.16, pp. 10757–10772. DOI: 10.5194/acp-19-10757-2019.

Matthias, V., A. Dörnbrack, and G. Stober (2016). "The extraordinarily strong and cold polar vortex in the early northern winter 2015/2016". In: *Geophys. Res. Lett.* DOI: 10.1002/2016gl071676.

Mébarki, Y., V. Catoire, N. Huret, G. Berthet, C. Robert, and G. Poulet (2010). "More evidence for very short-lived substance contribution to stratospheric chlorine inferred from HCl balloon-borne in situ measurements in the tropics". In: *Atmos. Chem. Phys.* 10.2, pp. 397–409. DOI: 10.5194/acp-10-397-2010.

Millet, D. B., M. Baasandorj, D. K. Farmer, J. A. Thornton, K. Baumann, P. Brophy, S. Chaliyakunnel, J. A. de Gouw, M. Graus, L. Hu, A. Koss, B. H. Lee, F. D. Lopez-Hilfiker, J. A. Neuman, F. Paulot, J. Peischl, I. B. Pollack, T. B. Ryerson, C. Warneke, B. J. Williams, and J. Xu (2015). "A large and ubiquitous source of atmospheric formic acid". In: *Atmos. Chem. Phys.* 15.11, pp. 6283–6304. DOI: 10.5194/acp-15-6283-2015.

Molina, L. T. and M. J. Molina (1987). "Production of chlorine oxide (Cl2O2) from the self-reaction of the chlorine oxide (ClO) radical". In: *J. Phys. Chem.* 91.2, pp. 433–436. DOI: 10.1021/j100286a035.

Molina, M. J. and F. S. Rowland (1974). "Stratospheric sink for chlorofluoromethanes: chlorine atom-catalysed destruction of ozone". In: *Nature* 249.5460, pp. 810–812. DOI: 10.1038/249810a0.

Montzka, S. A., G. S. Dutton, P. Yu, E. Ray, R. W. Portmann, J. S. Daniel, L. Kuijpers, B. D. Hall, D. Mondeel, C. Siso, J. D. Nance, M. Rigby, A. J. Manning, L. Hu, F. Moore, B. R. Miller, and J. W. Elkins (2018). "An unexpected and persistent increase in global emissions of ozone-depleting CFC-11". In: *Nature* 557.7705, pp. 413–417. DOI: 10.1038/s41586-018-0106-2.

Müller, S., P. Hoor, H. Bozem, E. Gute, B. Vogel, A. Zahn, H. Bönisch, T. Keber, M. Krämer, C. Rolf, M. Riese, H. Schlager, and A. Engel (2016). "Impact of the Asian monsoon on the extratropical lower stratosphere: trace gas observations during TACTS over Europe 2012". In: *Atmos. Chem. Phys.* 16.16, pp. 10573–10589. DOI: 10.5194/acp-16-10573-2016.

Nash, E. R., P. A. Newman, J. E. Rosenfield, and M. R. Schoeberl (1996). "An objective determination of the polar vortex using Ertel's potential vorticity". In: *J. Geophys. Res. Atmos.* 101.D5, pp. 9471–9478. DOI: 10.1029/96jd00066.

Neuman, J. A., L. G. Huey, T. B. Ryerson, and D. W. Fahey (1999). "Study of Inlet Materials for Sampling Atmospheric Nitric Acid". In: *Environ. Sci. Technol.* 33.7, pp. 1133–1136. DOI: 10.1021/es980767f.

NOAA-ESRL (2020). *Nitrous Oxide (N_2O) – Combined Data Set*. https://www.esrl.noaa.gov/gmd/hats/combined/N2O.html [Last access: 30 July 2020]. URL: https://www.esrl.noaa.gov/gmd/hats/combined/N2O.html.

Oelhaf, H., B.-M. Sinnhuber, W. Woiwode, H. Bönisch, H. Bozem, A. Engel, A. Fix, F. Friedl-Vallon, J.-U. Grooß, P. Hoor, S. Johansson, T. Jurkat-Witschas, S. Kaufmann, M. Krämer, J. Krause, E. Kretschmer, D. Lörks, A. Marsing, J. Orphal, K. Pfeilsticker, M. Pitts, L. Poole, P. Preusse, M. Rapp, M. Riese, C. Rolf, J. Ungermann, C. Voigt, C. M. Volk, M. Wirth, A. Zahn, and H. Ziereis (2019). "POLSTRACC: Airborne Experiment for Studying the Polar Stratosphere in a Changing Climate with the High Altitude and Long Range Research Aircraft (HALO)". In: *Bull. Amer. Meteor. Soc.* 100.12, pp. 2634–2664. DOI: 10.1175/bams-d-18-0181.1.

Popp, P. J., T. P. Marcy, R. S. Gao, L. A. Watts, D. W. Fahey, E. C. Richard, S. J. Oltmans, M. L. Santee, N. J. Livesey, L. Froidevaux, B. Sen, G. C. Toon, K. A. Walker, C. D. Boone,

and P. F. Bernath (2009). "Stratospheric correlation between nitric acid and ozone". In: *J. Geophys. Res.* 114.D3. DOI: 10.1029/2008jd010875.

Rex, M., R. J. Salawitch, N. R. P. Harris, P. von der Gathen, G. O. Braathen, A. Schulz, H. Deckelmann, M. Chipperfield, B.-M. Sinnhuber, E. Reimer, R. Alfier, R. Bevilacqua, K. Hoppel, M. Fromm, J. Lumpe, H. Küllmann, A. Kleinböhl, H. Bremer, M. von König, K. Künzi, D. Toohey, H. Vömel, E. Richard, K. Aikin, H. Jost, J. B. Greenblatt, M. Loewenstein, J. R. Podolske, C. R. Webster, G. J. Flesch, D. C. Scott, R. L. Herman, J. W. Elkins, E. A. Ray, F. L. Moore, D. F. Hurst, P. Romashkin, G. C. Toon, B. Sen, J. J. Margitan, et al. (2002). "Chemical depletion of Arctic ozone in winter 1999/2000". In: *J. Geophys. Res.* 107.D20. DOI: 10.1029/2001jd000533.

Riese, M., F. Ploeger, A. Rap, B. Vogel, P. Konopka, M. Dameris, and P. Forster (2012). "Impact of uncertainties in atmospheric mixing on simulated UTLS composition and related radiative effects". In: *J. Geophy. Res. Atmos.* 117.D16. DOI: 10.1029/2012jd017751.

Rothman, L., I. Gordon, Y. Babikov, A. Barbe, D. C. Benner, P. Bernath, M. Birk, L. Bizzocchi, V. Boudon, L. Brown, A. Campargue, K. Chance, E. Cohen, L. Coudert, V. Devi, B. Drouin, A. Fayt, J.-M. Flaud, R. Gamache, J. Harrison, J.-M. Hartmann, C. Hill, J. Hodges, D. Jacquemart, A. Jolly, J. Lamouroux, R. L. Roy, G. Li, D. Long, O. Lyulin, C. Mackie, S. Massie, S. Mikhailenko, H. Müller, O. Naumenko, A. Nikitin, J. Orphal, V. Perevalov, A. Perrin, E. Polovtseva, et al. (2013). "The HITRAN2012 molecular spectroscopic database". In: *J. Quant. Spectrosc. Radiat. Transfer* 130, pp. 4–50. DOI: 10.1016/j.jqsrt.2013.07.002.

Safieddine, S., M. Bouillon, A.-C. Paracho, J. Jumelet, F. Tencé, A. Pazmino, F. Goutail, C. Wespes, S. Bekki, A. Boynard, J. Hadji-Lazaro, P.-F. Coheur, D. Hurtmans, and C. Clerbaux (2020). "Antarctic Ozone Enhancement During the 2019 Sudden Stratospheric Warming Event". In: *Geophys. Res. Lett.* 47.14. DOI: 10.1029/2020gl087810.

Sala, S., H. Bönisch, T. Keber, D. E. Oram, G. Mills, and A. Engel (2014). "Deriving an atmospheric budget of total organic bromine using airborne in situ measurements from the western Pacific area during SHIVA". In: *Atmos. Chem. Phys.* 14.13, pp. 6903–6923. DOI: 10.5194/acp-14-6903-2014.

Santee, M. L., I. A. MacKenzie, G. L. Manney, M. P. Chipperfield, P. F. Bernath, K. A. Walker, C. D. Boone, L. Froidevaux, N. J. Livesey, and J. W. Waters (2008). "A study of stratospheric chlorine partitioning based on new satellite measurements and modeling". In: *J. Geophys. Res.* 113.D12. DOI: 10.1029/2007jd009057.

Schäuble, D. (2010). "Aufbau eines flugzeuggetragenen Massenspektrometers zur Messung von HNO$_3$ und HONO und Quantifizierung der HNO$_3$-Aufnahme in Eispartikel in Kondensstreifen und Zirren". PhD thesis. Johannes-Gutenberg-Universität Mainz. URL: https://publications.ub.uni-mainz.de/theses/volltexte/2011/2647/pdf/2647.pdf.

Schmeltekopf, A., D. Albritton, P. Crutzen, P. Goldan, W. Harrop, W. Henderson, J. McAfee, M. McFarland, H. Schiff, T. Thompson, D. Hofmann, and N. Kjome (1977). "Stratospheric

Nitrous Oxide Altitude Profiles at Various Latitudes". In: *J. Atmos. Sci.* 34.5, pp. 729–736. DOI: 10.1175/1520-0469(1977)034<0729:snoapa>2.0.co;2.

Solomon, S., S. Borrmann, R. R. Garcia, R. Portmann, L. Thomason, L. R. Poole, D. Winker, and M. P. McCormick (1997). "Heterogeneous chlorine chemistry in the tropopause region". In: *J. Geophys. Res. Atmos.* 102.D17, pp. 21411–21429. DOI: 10.1029/97jd01525.

Solomon, S., J. Haskins, D. J. Ivy, and F. Min (2014). "Fundamental differences between Arctic and Antarctic ozone depletion". In: *P. Natl. Acad. Sci.* 111.17, pp. 6220–6225. DOI: 10.1073/pnas.1319307111.

Strahan, S. E. and A. R. Douglass (2018). "Decline in Antarctic Ozone Depletion and Lower Stratospheric Chlorine Determined From Aura Microwave Limb Sounder Observations". In: *Geophys. Res. Lett.* 45.1, pp. 382–390. DOI: 10.1002/2017gl074830.

Sumińska-Ebersoldt, O., R. Lehmann, T. Wegner, J.-U. Grooß, E. Hösen, R. Weigel, W. Frey, S. Griessbach, V. Mitev, C. Emde, C. M. Volk, S. Borrmann, M. Rex, F. Stroh, and M. von Hobe (2012). "ClOOCl photolysis at high solar zenith angles: analysis of the RECONCILE self-match flight". In: *Atmos. Chem. Phys.* 12.3, pp. 1353–1365. DOI: 10.5194/acp-12-1353-2012.

Symonds, R. B., W. I. Rose, and M. H. Reed (1988). "Contribution of C1- and F-bearing gases to the atmosphere by volcanoes". In: *Nature* 334.6181, pp. 415–418. DOI: 10.1038/334415a0.

Takahashi, K., T. Nakayama, Y. Matsumi, S. Solomon, T. Gejo, E. Shigemasa, and T. J. Wallington (2002). "Atmospheric lifetime of SF_5CF_3". In: *Geophys. Res. Lett.* 29.15, pp. 7–1–7–4. DOI: 10.1029/2002gl015356.

Talbot, R. W., R. C. Harriss, E. V. Browell, G. L. Gregory, D. I. Sebacher, and S. M. Beck (1986). "Distribution and geochemistry of aerosols in the tropical north Atlantic troposphere: Relationship to Saharan dust". In: *J. Geophys. Res.* 91.D4, p. 5173. DOI: 10.1029/jd091id04p05173.

Thornton, B. F., D. W. Toohey, A. F. Tuck, J. W. Elkins, K. K. Kelly, S. J. Hovde, E. C. Richard, K. H. Rosenlof, T. L. Thompson, M. J. Mahoney, and J. C. Wilson (2007). "Chlorine activation near the midlatitude tropopause". In: *J. Geophys. Res.* 112.D18. DOI: 10.1029/2006jd007640.

Toon, O. B., A. Tabazadeh, E. V. Browell, and J. Jordan (2000). "Analysis of lidar observations of Arctic polar stratospheric clouds during January 1989". In: *J. Geophy. Res. Atmos.* 105.D16, pp. 20589–20615. DOI: 10.1029/2000jd900144.

Ungermann, J., J. Blank, M. Dick, A. Ebersoldt, F. Friedl-Vallon, A. Giez, T. Guggenmoser, M. Höpfner, T. Jurkat, M. Kaufmann, S. Kaufmann, A. Kleinert, M. Krämer, T. Latzko, H. Oelhaf, F. Olchewski, P. Preusse, C. Rolf, J. Schillings, O. Suminska-Ebersoldt, V. Tan, N. Thomas, C. Voigt, A. Zahn, M. Zöger, and M. Riese (2015). "Level 2 processing for the imaging Fourier transform spectrometer GLORIA: derivation and validation of

temperature and trace gas volume mixing ratios from calibrated dynamics mode spectra". In: *Atmos. Meas. Tech.* 8.6, pp. 2473–2489. DOI: 10.5194/amt-8-2473-2015.

Vogel, B., J.-U. Grooß, R. Müller, T. Deshler, J. Karhu, D. S. McKenna, M. Müller, D. Toohey, G. C. Toon, and F. Stroh (2003). "Vertical profiles of activated ClO and ozone loss in the Arctic vortex in January and March 2000: In situ observations and model simulations". In: *J. Geophys. Res.* 108.D22. DOI: 10.1029/2002jd002564.

Voigt, C., J. Schreiner, A. Kohlmann, P. Zink, K. Mauersberger, N. Larsen, T. Deshler, C. Kröger, J. Rosen, A. Adriani, F. Cairo, G. D. Donfrancesco, M. Viterbini, J. Ovarlez, H. Ovarlez, C. David, and A. Dörnbrack (2000a). "Nitric Acid Trihydrate (NAT) in Polar Stratospheric Clouds". In: *Science* 290.5497, pp. 1756–1758. DOI: 10.1126/science.290.5497.1756.

Voigt, C., A. Tsias, A. Dörnbrack, S. Meilinger, B. Luo, J. Schreiner, N. Larsen, K. Mauersberger, and T. Peter (2000b). "Non-equilibrium compositions of liquid polar stratospheric clouds in gravity waves". In: *Geophys. Res. Lett.* 27.23, pp. 3873–3876. DOI: 10.1029/2000gl012168.

Voigt, C., H. Schlager, B. P. Luo, A. Dörnbrack, A. Roiger, P. Stock, J. Curtius, H. Vössing, S. Borrmann, S. Davies, P. Konopka, C. Schiller, G. Shur, and T. Peter (2005). "Nitric Acid Trihydrate (NAT) formation at low NAT supersaturation in Polar Stratospheric Clouds (PSCs)". In: *Atmos. Chem. Phys.* 5.5, pp. 1371–1380. DOI: 10.5194/acp-5-1371-2005.

Voigt, C., U. Schumann, T. Jurkat, D. Schäuble, H. Schlager, A. Petzold, J.-F. Gayet, M. Krämer, J. Schneider, S. Borrmann, J. Schmale, P. Jessberger, T. Hamburger, M. Lichtenstern, M. Scheibe, C. Gourbeyre, J. Meyer, M. Kübbeler, W. Frey, H. Kalesse, T. Butler, M. G. Lawrence, F. Holzäpfel, F. Arnold, M. Wendisch, A. Döpelheuer, K. Gottschaldt, R. Baumann, M. Zöger, I. Sölch, M. Rautenhaus, and A. Dörnbrack (2010). "In-situ observations of young contrails – overview and selected results from the CONCERT campaign". In: *Atmos. Chem. Phys.* 10.18, pp. 9039–9056. DOI: 10.5194/acp-10-9039-2010.

Voigt, C., P. Jessberger, T. Jurkat, S. Kaufmann, R. Baumann, H. Schlager, N. Bobrowski, G. Giuffrida, and G. Salerno (2014). "Evolution of CO_2, SO_2, HCl, and HNO_3 in the volcanic plumes from Etna". In: *Geophys. Res. Lett.* 41.6, pp. 2196–2203. DOI: 10.1002/2013gl058974.

Voigt, C., A. Dörnbrack, M. Wirth, S. M. Groß, M. C. Pitts, L. R. Poole, R. Baumann, B. Ehard, B.-M. Sinnhuber, W. Woiwode, and H. Oelhaf (2018). "Widespread polar stratospheric ice clouds in the 2015–2016 Arctic winter – implications for ice nucleation". In: *Atmos. Chem. Phys.* 18.21, pp. 15623–15641. DOI: 10.5194/acp-18-15623-2018.

Wagner, G. and M. Birk (2003). "New infrared spectroscopic database for chlorine nitrate". In: *J. Quant. Spectrosc. Radiat. Transfer* 82.1-4, pp. 443–460. DOI: 10.1016/s0022-4073(03)00169-9.

Wagner, J., A. Dörnbrack, M. Rapp, S. Gisinger, B. Ehard, M. Bramberger, B. Witschas, F. Chouza, S. Rahm, C. Mallaun, G. Baumgarten, and P. Hoor (2017). "Observed versus

simulated mountain waves over Scandinavia – improvement of vertical winds, energy and momentum fluxes by enhanced model resolution?" In: *Atmos. Chem. Phys.* 17.6, pp. 4031–4052. DOI: 10.5194/acp-17-4031-2017.

Wegner, T., J.-U. Grooß, M. von Hobe, F. Stroh, O. Sumińska-Ebersoldt, C. M. Volk, E. Hösen, V. Mitev, G. Shur, and R. Müller (2012). "Heterogeneous chlorine activation on stratospheric aerosols and clouds in the Arctic polar vortex". In: *Atmos. Chem. Phys.* 12.22, pp. 11095–11106. DOI: 10.5194/acp-12-11095-2012.

Wendisch, M., M. Brückner, J. Burrows, S. Crewell, K. Dethloff, K. Ebell, C. Lüpkes, A. Macke, J. Notholt, J. Quaas, A. Rinke, and I. Tegen (2017). "Understanding Causes and Effects of Rapid Warming in the Arctic". In: *Eos*. DOI: 10.1029/2017eo064803.

Werner, A., C. M. Volk, E. V. Ivanova, T. Wetter, C. Schiller, H. Schlager, and P. Konopka (2010). "Quantifying transport into the Arctic lowermost stratosphere". In: *Atmos. Chem. Phys.* 10.23, pp. 11623–11639. DOI: 10.5194/acp-10-11623-2010.

Wetzel, G., H. Oelhaf, O. Kirner, R. Ruhnke, F. Friedl-Vallon, A. Kleinert, G. Maucher, H. Fischer, M. Birk, G. Wagner, and A. Engel (2010). "First remote sensing measurements of ClOOCl along with ClO and ClONO$_2$ in activated and deactivated Arctic vortex conditions using new ClOOCl IR absorption cross sections". In: *Atmos. Chem. Phys.* 10.3, pp. 931–945. DOI: 10.5194/acp-10-931-2010.

Wetzel, G., H. Oelhaf, M. Birk, A. de Lange, A. Engel, F. Friedl-Vallon, O. Kirner, A. Kleinert, G. Maucher, H. Nordmeyer, J. Orphal, R. Ruhnke, B.-M. Sinnhuber, and P. Vogt (2015). "Partitioning and budget of inorganic and organic chlorine species observed by MIPAS-B and TELIS in the Arctic in March 2011". In: *Atmos. Chem. Phys.* 15.14, pp. 8065–8076. DOI: 10.5194/acp-15-8065-2015.

Wilmouth, D. M., R. M. Stimpfle, J. G. Anderson, J. W. Elkins, D. F. Hurst, R. J. Salawitch, and L. R. Lait (2006). "Evolution of inorganic chlorine partitioning in the Arctic polar vortex". In: *J. Geophys. Res.* 111.D16. DOI: 10.1029/2005jd006951.

Wirth, M., A. Fix, P. Mahnke, H. Schwarzer, F. Schrandt, and G. Ehret (2009). "The airborne multi-wavelength water vapor differential absorption lidar WALES: system design and performance". In: *Appl. Phys. B* 96.1, pp. 201–213. DOI: 10.1007/s00340-009-3365-7.

Wohltmann, I., T. Wegner, R. Müller, R. Lehmann, M. Rex, G. L. Manney, M. L. Santee, P. Bernath, O. Sumińska-Ebersoldt, F. Stroh, M. von Hobe, C. M. Volk, E. Hösen, F. Ravegnani, A. Ulanovsky, and V. Yushkov (2013). "Uncertainties in modelling heterogeneous chemistry and Arctic ozone depletion in the winter 2009/2010". In: *Atmos. Chem. Phys.* 13.8, pp. 3909–3929. DOI: 10.5194/acp-13-3909-2013.

Wohltmann, I., R. Lehmann, and M. Rex (2017). "A quantitative analysis of the reactions involved in stratospheric ozone depletion in the polar vortex core". In: *Atmos. Chem. Phys.* 17.17, pp. 10535–10563. DOI: 10.5194/acp-17-10535-2017.

Woiwode, W., A. Dörnbrack, M. Bramberger, F. Friedl-Vallon, F. Haenel, M. Höpfner, S. Johansson, E. Kretschmer, I. Krisch, T. Latzko, H. Oelhaf, J. Orphal, P. Preusse, B.-M.

Sinnhuber, and J. Ungermann (2018). "Mesoscale fine structure of a tropopause fold over mountains". In: *Atmos. Chem. Phys.* 18.21, pp. 15643–15667. DOI: 10.5194/acp-18-15643-2018.

Woiwode, W., A. Dörnbrack, I. Polichtchouk, S. Johansson, B. Harvey, M. Höpfner, J. Ungermann, and F. Friedl-Vallon (2020). "Technical note: Lowermost-stratosphere moist bias in ECMWF IFS model diagnosed from airborne GLORIA observations during winter–spring 2016". In: *Atmos. Chem. Phys.* 20.23, pp. 15379–15387. DOI: 10.5194/acp-20-15379-2020.

Wolff, M. A., T. Kerzenmacher, K. Strong, K. A. Walker, M. Toohey, E. Dupuy, P. F. Bernath, C. D. Boone, S. Brohede, V. Catoire, T. von Clarmann, M. Coffey, W. H. Daffer, M. D. Mazière, P. Duchatelet, N. Glatthor, D. W. T. Griffith, J. Hannigan, F. Hase, M. Höpfner, N. Huret, N. Jones, K. Jucks, A. Kagawa, Y. Kasai, I. Kramer, H. Küllmann, J. Kuttippurath, E. Mahieu, G. Manney, C. T. McElroy, C. McLinden, Y. Mébarki, S. Mikuteit, D. Murtagh, C. Piccolo, P. Raspollini, M. Ridolfi, R. Ruhnke, M. Santee, et al. (2008). "Validation of HNO_3, $ClONO_2$, and N_2O_5 from the Atmospheric Chemistry Experiment Fourier Transform Spectrometer (ACE-FTS)". In: *Atmos. Chem. Phys.* 8.13, pp. 3529–3562. DOI: 10.5194/acp-8-3529-2008.

World Meteorological Organization (2003). *Scientific Assessment of Ozone Depletion: 2002, Global Ozone Research and Monitoring Project - Report No. 47, 498 pp.* Geneva, Switzerland.

– (2011). *Scientific Assessment of Ozone Depletion: 2010, Global Ozone Research and Monitoring Project - Report No. 52, 516 pp.* Geneva, Switzerland.

– (2018). *Scientific Assessment of Ozone Depletion: 2018, Global Ozone Research and Monitoring Project – Report No. 58, 588 pp.* Geneva, Switzerland.

Xia, Y., Y. Huang, and Y. Hu (2017). "On the climate impacts of upper tropospheric and lower stratospheric ozone". In: *J. Geophys. Res. Atmos.* DOI: 10.1002/2017jd027398.

Ziereis, H., H. Schlager, P. Schulte, P. F. J. van Velthoven, and F. Slemr (2000). "Distributions of NO, NO_x, and NO_y in the upper troposphere and lower stratosphere between $28°$ and $61°$N during POLINAT 2". In: *J. Geophys. Res. Atmos.* 105.D3, pp. 3653–3664. DOI: 10.1029/1999jd900870.